Micromachined III-V cantilevers for AFM-guided scanning Hall probe microscopy

Brook, Alexander J.

Award date:
2003

Awarding institution:
University of Bath

Micromachined III-V Cantilevers for AFM-guided Scanning Hall Probe Microscopy

Submitted by Alexander J Brook

for the degree of

Doctor of Philosophy

of the University of Bath

2003

ProQuest LLC
789 East Eisenhower Parkway
P.O. Box 1346
Ann Arbor, MI 48106-1346

Abstract

This thesis describes the development of a new III-V cantilever-based atomic force sensor with piezoresistive detection and an integrated Hall probe for scanning Hall probe microscopy. This integration of the sensors allows simple operation in high-vacuum/variable-temperature environments and enables very high magnetic and topographic resolution to be achieved simultaneously

AFM detection is achieved by piezoresistive sensing, and two types of sensor are described. One is fabricated from a novel piezoresistive material based on the ternary alloy n-$Al_{0.4}Ga_{0.6}As$. The second is based on a two-dimensional electron gas, which reduced the complexity of the sensor fabrication. Both sensors were found to have sensitivities comparable to those achieved by commercial p-type silicon piezoresistive cantilevers.

The integrated Hall probe is fabricated from a high mobility two-dimensional electron gas heterostructure. Hall sensors with a width of 1μm were successfully fabricated on the cantilever surface. The integrated cantilever was mounted in a modified STM-guided Hall probe microscope and used to scan various samples. Scans of magnetic induction and topography of the samples are presented to illustrate the sensor performance at 300K and 77K.

Acknowledgements

I would like to thank my supervisor Prof. Simon Bending for all the time and effort he has put into making the project possible. His guidance has allowed me to complete this work and provided me with many solutions to the problems that have arisen during the project.

I would also like to thank Dr. Ahmet Oral and the rest of the Physics department at Bilkent University, Turkey. During my month long visit, their hospitality and hard work was very much appreciated and led to several of the results that are presented in this work. I would especially like to thank Munir Dede who was my personal translator, provided great assistance in the lab and also managed to show me many wonderful places in Ankara.

I would like to thank those who have collaborated with work for this project these include, Dr. Mohamed Henini at the University of Nottingham, Dr. D. Ritchie and Dr. H. Beere at the University of Cambridge and Dr. A. Springthorpe at Nortel Networks, Canada. Lastly, John Pinto, whose original work on GaAs/AlGaAs piezoresistive cantilevers was a basis for the work presented here.

Many others have also helped me during the course of this project, they include, the technical staff at the University of Bath, especially Ms. Wendy Lambson for her help in the clean room. Dr. Siva Sivaraya, for his many hours spent teaching me the art of semiconductor fabrication. Dr. Alexander Grigorenko, for his help and enlightening conversations. Other people I would like to thank are Dr.

David Lawton, Dr. James Gregory and Dejan Uzur and all those who played alongside me for Physics Department football team.

Finally I would like to thank my family and friends for all their help and support during the course of this project, especially my mother and father for their encouragement and backing over the years.

Contents

Chapter 1

1 Introduction

1.1 Background and motivation

The use of magnetic materials in modern technology has now become commonplace. From the hard disk in a modern PC to a magnetic resonance imaging system, the use of materials with precise magnetic characteristics has become deeply embedded in our everyday lives. Furthermore the need for improvement in these materials is readily apparent, in order to increase storage density for example or raising the critical temperature of high temperature superconductors (HTS). It is for this reason that techniques for the characterisation of these magnetic materials have also advanced in order to properly assess them. In this context, the investigation of the magnetic properties of new materials must involve their complete characterisation and allow the determination of their suitability for specific applications.

Much of the key information concerning the magnetic properties of these materials can be acquired through bulk or 'global' measurement techniques, such as temperature-dependent magnetization and transport measurements. However, microscopic information can only be obtained via local magnetic probes with spatial resolution comparable to the length scales of the relevant magnetic phenomena. As an example, two common magnetic imaging test features are individual bit tracks on a modern hard disk with a bit spacing of <50nm[1] and discrete flux vortices in

superconducting materials which have a characteristic diameter of the order of a micron.

Current local magnetic imaging techniques with the ability to resolve details <10μm are summarised in Figure 1.1. The chart shows the trade-off between spatial resolution and minimum detectable field (MDF). At one end of the spectrum is magnetic force microscopy (MFM) with high spatial resolution. At the other end is scanning SQUID microscopy with an excellent MDF. Scanning Hall probe microscopy (SHPM) offers an excellent compromise, with its spatial resolution and sensitivity lying somewhere between these two extremes. This makes SHPM an excellent complementary technique to be used in combination with others in the role of magnetic imaging.

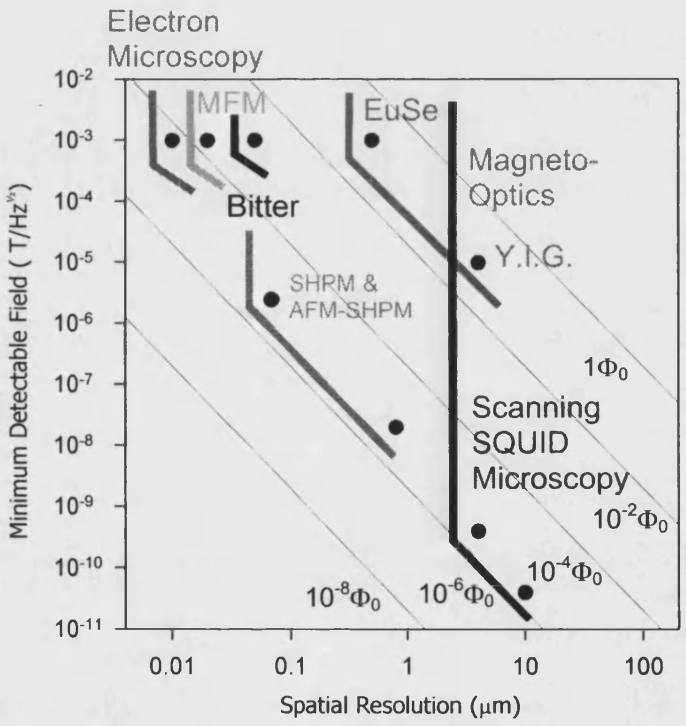

Figure 1.1 Chart comparing different magnetic imaging methods[2]

Scanning Hall probe microscopy (SHPM) is a quantitative technique that uses the Hall effect to measure the local surface magnetic induction with a micrometer-sized Hall sensor (often fabricated in a cross geometry). The technique of measuring magnetic materials using the Hall effect is not new, but recent advances in micro-fabrication have allowed spatial resolutions of up to ~100nm and minimum detectable fields of $\sim 10^{-6}$ T/√Hz (300K) to be achieved[3,4]. The Hall cross can be fabricated from many materials depending on the required operating environment. High spatial resolution can be achieved using materials such as bismuth[3], which can be milled with a focused ion beam to widths of ~100nm; however the minimum detectable field (MDF) is high for these sensors due to their characteristically low carrier motilities. For low noise and/or high field sensitivity applications two dimensional electron gas (2DEG) systems can be fabricated from GaAs/$Al_xGa_{1-x}As$ modulation doped heterostructures. This material limits the spatial resolution to >200nm due to edge wall depletion however at low temperatures (77K) an MDF of $\sim 10^{-8}$ T/√Hz can be achieved[4]. At room temperature the best performance can be achieved using InSb-based sensors with noise levels up to an order of magnitude smaller than those for GaAs/$Al_xGa_{1-x}As$ 2DEG sensors[5] at 300K.

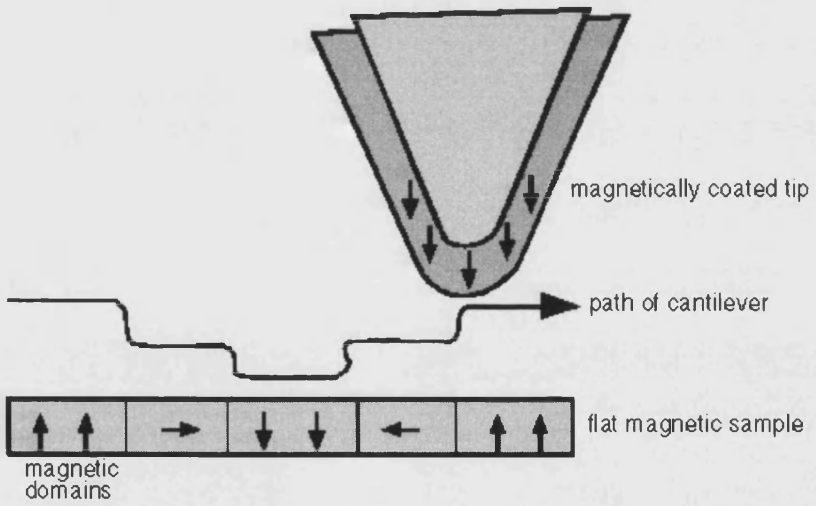

Figure 1.2 Magnetic force microscope tip scanning above a magnetic sample[6]

The SHPM can be seen as complementary to both MFM and SQUID imaging as it is capable of quantitative and non-invasive imaging of magnetic materials with sub-micron resolution at temperatures ranging from room temperature down to 4K.

The magnetic force microscope is capable of imaging at very high spatial resolutions (<100nm) but this is achieved by using a sharp atomic force microscope (AFM) tip coated with a ferromagnetic material such as cobalt as in Figure 1.2. The tip is scanned across the surface of a material and the resulting deflection (or shift in resonant amplitude/phase) is recorded giving a map of the magnetic interaction of the tip with the surface. The use of the magnetically coated tip means the method can be invasive and this is most likely why the method is mainly used in the investigation of "hard" ferromagnetic materials. In addition, the technique is challenging to adapt to low temperatures and the results obtained are hard to interpret quantitatively.

SQUID microscopy is able to quantitatively measure stray fields of magnetic materials with unparalleled sensitivity. It can achieve a MDF of $\sim 10^{-10}$ T/$\sqrt{\text{Hz}}$ which is at least 2 orders of magnitude better than other methods. The SQUID sensor though is usually fabricated from a low-T_c material such as niobium (T_c = 9.2K) requiring the experiment to be conducted either below this critical temperature or in a thermally isolated environment which is inevitably some distance from the sample. The resolution of the probe is also currently restricted by micro-fabrication limitations to $\geq 1\mu$m.

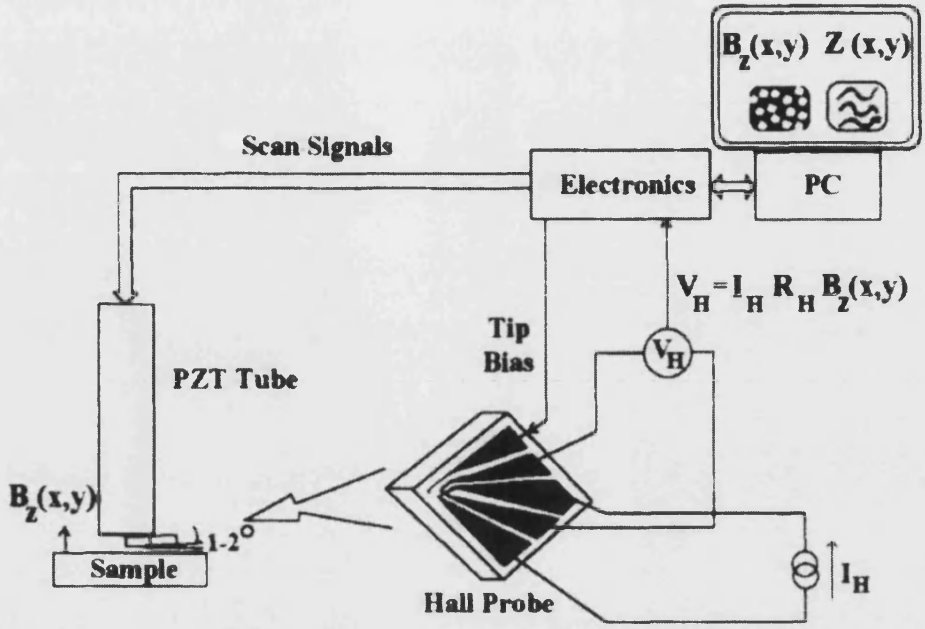

Figure 1.3 Schematic of STM-tracking SHPM[4]

Although SHPM has many advantages, it does also have its drawbacks. An outline of a typical SHPM measurement system is given in Figure 1.3. The sensor consists of a Hall probe and STM tip fabricated on a single semiconductor chip. The sensor is then attached to a piezoelectric scanner tube and scanned across the sample; the measured STM tip current keeps the sensor height constant via a feedback loop. This allows the local induction at the surface and the surface topography to be measured simultaneously creating both a magnetic and topographic map of the sample. The use of the STM tracking method does, however, require the sample to be conducting and topologically connected. If this is not the case it must be coated with a thin metallic layer (e.g. gold) which for some magnetic samples is neither desirable nor practical.

There is a need, therefore, for an SHPM system capable of imaging insulating materials without extensive sample preparation. There have recently been several attempts at a solution to this problem. One approach employed shear force detection using additional piezoelectric plates[7], whereby a non-planar 2DEG Hall cross was glued to the end of one of the plates and scanned across the sample. Another method

proposed by Weaver *et. al.*[8] is to fabricate a Hall sensor at the apex of an atomic force microscope (AFM) tip. The Hall sensor fabricated from bismuth was defined using e-beam lithography allowing resolutions of <500nm, the minimum detectable fields were, however, very low. The positioning of the Hall sensor on the end of the AFM tip could also lead to general degradation of its performance over time. In this case the sensor height was detected by an optical method commonly used in commercial AFMs. A slightly different approach was taken by Nakamura *et. al.*[9] Instead of using a Hall sensor they placed a magnetoresistive head at the apex of an AFM cantilever to measure the stray field, while also employing an optical technique to detect the sensor height deflection.

Whilst all these methods eliminate the need to coat the sample of interest beforehand, they do so by introducing considerable experimental complications. Ideally a solution similar to the single integrated chip approach of the STM-tracking SHPM is required, which allows simple operation in a variable temperature environment such as a cryostat. Consequently our solution to this problem was to integrate a 2DEG Hall probe with a piezoresistive AFM cantilever. The 2DEG Hall probe allows magnetic imaging at different temperatures and the piezoresistive cantilever allows deflection detection in a single-chip sensor with no additional 'external' components.

1.2 The Atomic force Microscope (AFM)

The basic objective of an AFM is to measure the forces (at the atomic level) between a sharp probing tip (which is attached to the end of a cantilever) and a sample surface. Images are taken by scanning the sample relative to the probing tip and measuring the deflection of the cantilever as a function of lateral position. The first AFM was introduced by Binnig *et. al.*[10] when they proposed that by using a cantilever with a spring constant smaller than the effective spring constant of an atom bonded at the surface of a solid, imaging on an atomic scale could be realised.

Their first attempt used an STM technique to measure the cantilever deflection, resulting in a vertical resolution of ~1Å. Since then techniques have been demonstrated using capacitive[11], piezoresistive[12] and optical detection methods[13], the most common of which is the optical deflection method.

1.2.1 Optical Deflection AFM

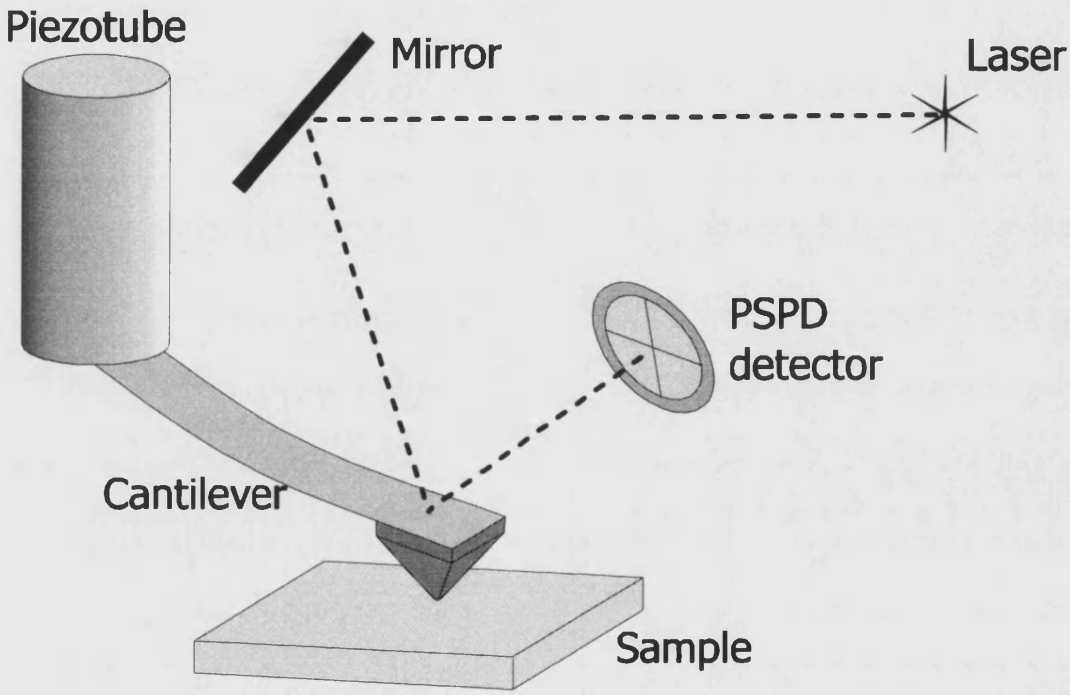

Figure 1.4 Optical method of measuring cantilever deflection[6]

In the most common scheme, shown in Figure 1.4, a beam from a laser diode bounces off the back of the cantilever onto a position-sensitive photodetector (PSPD). As the cantilever bends, the position of the beam on the detector shifts resulting in changes in their output voltages. The PSPD itself can measure displacements of light reflected from the back of the cantilever surface as small as 10Å across the detector. The ratio of the path length between the cantilever and the detector to the length of the cantilever itself produces a mechanical amplification. As a result, the system can detect sub-angstrom vertical movement of the cantilever tip (A "quad-cell" PSPD can be used to also measure the cantilever torsion, giving

further insight into properties of a material such as surface friction). The optical method is also the most sensitive AFM method allowing a minimum detectable deflection (MDD) limited only by the intrinsic thermo-mechanical noise (~0.01pm/√Hz).

The use of the optical method, although providing the most sensitive method for detecting cantilever deflection, does pose some problems when used in closed environments such UHV chambers and cryostats. The need to align the optical components *in situ* makes the experimental setup very complicated and time consuming. The use of the laser beam deflection method also limits the width of the cantilever to be larger than the laser spot size, which for commercial lasers is ~30μm.

1.2.2 Piezoresistive AFM

The phenomenon of piezoresistance in semiconductors has been utilised in strain gauges since its discovery some 40 years ago[14], and soon afterwards it was found that by doping the silicon with a p-type material further enhancement in the piezoresistive effect could be achieved[15]. This property of p-Si was exploited by Tortonese *et. al*[12] who demonstrated AFM imaging using a micro-machined cantilever with an integrated piezoresistor[16]. By integrating the highly doped p-type sensor onto the cantilever, atomic-resolution topographic imaging became possible without the need for critically aligned optical sensing elements, as in Figure 1.4.

A schematic of the cantilever design first suggested by Tortonese *et. al.* is shown in Figure 1.5. By implanting boron and micro-machining a central channel, a conducting path is created in the surface of the silicon at the base of a cantilever. A voltage is applied across the two legs, allowing current to flow through one leg of the probe, and back through the other. When the cantilever is deflected downwards, tensile stress in the top layer results in an increase in resistance, and the converse occurs when the beam is bent upwards.

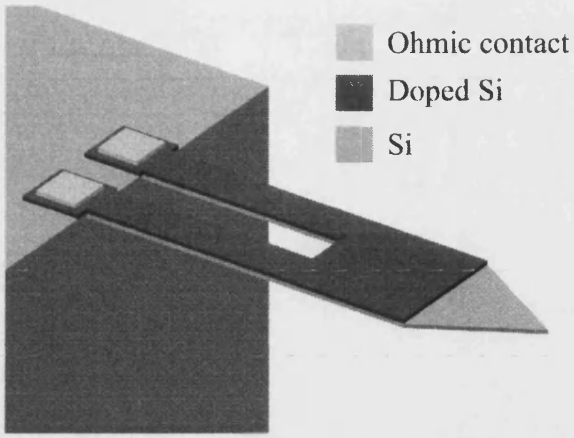

Figure 1.5 Schematic of the Tortonese *el al.*[16] piezoresistive cantilever

Piezoresistive cantilevers have been used in many applications where the use of optical methods would be impractical or impossible; these include multi-cantilever arrays[17], portable sensing equipment[18] and ultra small/thin cantilevers[19]. However, the use of piezoresistive detection is not that widespread, even with the advantages mentioned above, due to an order of magnitude loss in vertical resolution when compared to optical methods.

1.2.3 AFM imaging modes

The methods for scanning an AFM cantilever across a sample are numerous, the most common methods, contact, non-contact and intermittent contact are discussed in the following sections.

1.2.3.1 Contact mode

In contact-AFM mode, also known as repulsive mode, the AFM tip makes soft "physical contact" with the sample. To successfully scan using contact mode the cantilever spring constant must be small i.e. lower than the effective spring constant holding the atoms of the sample together. To create an image the tip is raster

scanned gently across the sample (or the sample under the tip), and the contact forces between the tip and the surface result in a deflection of the cantilever. These deflections are then measured using the methods such as those described previously in 1.2.1 and 1.2.2.

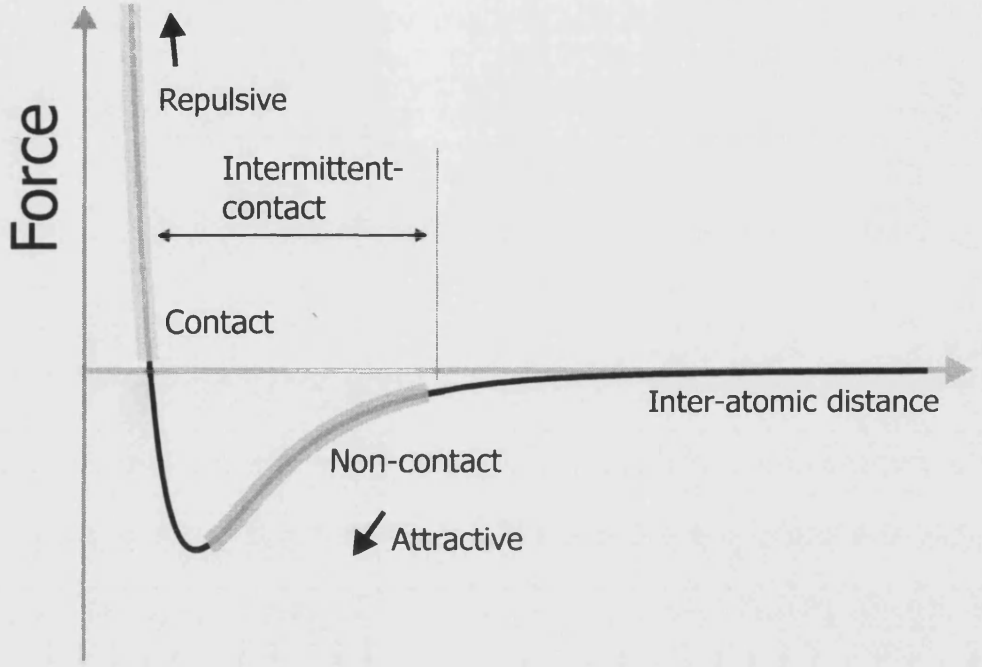

Figure 1.6 Lennard-Jones force curve describing the different AFM imaging modes.

The forces involved in the interaction of an AFM tip and surface are usually modelled using a Lennard – Jones force as shown in Figure 1.6. The Lennard - Jones potential between two atoms is given by

$$V(r) = 4V_0\left[\left(\frac{\sigma}{r}\right)^{12} - \left(\frac{\sigma}{r}\right)^{6}\right] \qquad (1.1)$$

This phenomenological expression combines the attractive van der Waals and repulsive atomic potentials as a function of inter-atomic distance r. The potential is at a minimum value of $V = -V_0$ at a distance $r = 1.12\sigma$ and is zero for $\sigma = r$ (σ is defined as the equilibrium distance for the two interacting molecules). The forces are obtained by differentiating eqn. 1.1, yielding

$$F(r) = -24V_0\left[\frac{\sigma^6}{r^7} - \frac{2\sigma^{12}}{r^{13}}\right] \quad (1.2)$$

This expression results in a curve as in Figure 1.6. As the inter-atomic spacing is gradually reduced a weak attraction is observed between the atoms due to van der Waals forces. This attraction increases until the atoms are so close together that their electron clouds start to repulse causing additional atomic repulsion. This repulsion progressively outweighs the attractive force as their inter-atomic separation continues to decrease. The force goes to zero when the distance between the atoms reaches a couple of angstroms. Once the force is repulsive the system is said to be in 'contact'. The very steep slope in the repulsive or contact regime means that when the cantilever pushes the tip against the sample whilst in contact, the cantilever bends rather than the tip atoms getting closer to the sample atoms.

In addition to the attractive van der Waals force described above, two other forces are generally present during contact - AFM operation: a capillary force exerted by the thin water layer often present in an ambient environment, and the force exerted by the cantilever itself. The net forces exerted in total for a typical contact AFM are in the operating range of 10^{-7} to 10^{-6}N [6].

To scan an image of the surface topography, two modes can be used: constant-height or constant-force mode. In constant-height mode, the spatial variation of the cantilever deflection is used directly to generate the topographic data, with the height of the scanner fixed as it scans. In constant-force mode, the deflection of the cantilever can be used as input to a feedback circuit that moves the scanner up and down in the z direction, responding to the topography by keeping the cantilever deflection constant. In this case, the image is generated from z-motion of the scanner. With the cantilever deflection held constant, the total force applied to the sample is also constant.

1.2.3.2 Non-contact AFM

Non-contact AFM (NC-AFM) or attractive mode imaging detects the surface topography by exploiting the attractive region of the Lennard-Jones force curve in Figure 1.6. The advantage of using NC-AFM is that it provides a means for measuring sample topography with little or no contact between the tip and the sample. The total force between the tip and the sample in the non-contact regime is very low, much lower than contact mode, and generally about 10^{-12}N. This low force is advantageous for studying soft or elastic samples. It is for this reason that AFM has become very popular in the imaging of soft biological samples.

The reduced force does mean that the deflection of the cantilever is much smaller and requires a more sensitive method for detecting the cantilever deflection. The common method employed is an AC detection method, whereby the cantilever is vibrated near its resonant frequency and changes in the resonance frequency or vibration amplitude are detected as the tip nears the sample surface. The change in resonance frequency is attributed to a change in the effective spring constant of the cantilever which in turn is due to a change in the local force gradient. The force gradient is the derivative of the force versus distance curve shown in Figure 1.6 and is a function of inter-atomic separation, which in turn allows imaging of the surface topography. This method does require the use of stiff cantilevers with spring constants greater than the local force gradient to prevent the cantilever from 'snapping down' onto the surface of the sample. It is for this reason that short thick cantilevers with large spring constants are used for NC-AFM.

1.2.3.3 Intermittent-contact mode

Intermittent-contact atomic force microscopy (IC-AFM) also known as 'Tapping Mode' is similar to NC-AFM, except that for IC-AFM the vibrating cantilever tip is brought closer to the sample so that at the bottom of its travel just barely hits, or "taps" the sample. The IC-AFM operating region is indicated on the force curve in

Figure 1.6. As for NC-AFM, in IC-AFM the cantilever's oscillation amplitude changes in response to tip-to-sample spacing, the difference being that the change in amplitude is much larger and therefore easier to detect. Again the image of the surface topography is obtained by monitoring these changes.

1.3 The Hall effect

In 1879 E. C. Hall discovered that when a metal plate, through which an electric current is being passed, was placed in a magnetic field perpendicular to the plate, a potential difference is observed between the two sides of the plate.

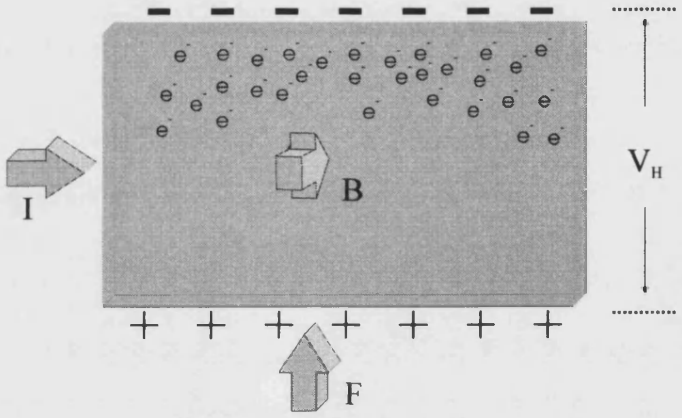

Figure 1.7 The Hall effect

Figure 1.7 illustrates Hall's experiment whereby electrons are forced to one side of the plate creating a potential difference, V_H, known as the Hall voltage. The motion of the electrons is due to the Lorentz force ($\vec{F} = -q\vec{v} \times \vec{B}$) acting on them. The potential difference between the plates is given by

$$V_H = -\frac{BI}{nqt} \tag{1.3}$$

where I is the current, B the electric field, t is the plate thickness and n is the charge carrier density. The Hall constant of the material R_H is then defined as

$$R_H = -\frac{1}{nq} \tag{1.4}$$

The Hall probe is therefore a very versatile device as it can also be used to measure both the carrier density and its charge or alternatively, if these are known, the magnetic field.

1.4 References

[1] Hitachi Deskstar 180GXP Specifications, www.hgst.com

[2] S. J. Bending, *Advances in Physics*, **48**, 449 (1999)

[3] A. Sandhu, H. Masuda, K. Kurosawa, A. Oral, and S. J. Bending, *Electronics Letters*, **37**, 1335 (2001)

[4] A. Oral, S. J. Bending, and M. Henini, *App. Phys. Lett.*, **69**, 1324 (1996)

[5] A. Oral, M. Kaval, M. Dede, H. Masuda, A. Okamoto, I. Shibasaki, and A. Sandhu, *IEEE TRANSACTIONS ON MAGNETICS*, **38,** 2438 (Part 1) (2002)

[6] from TM microscopes webpage. http://www.tmmicro.com/spmguide/

[7] T. Schweinbock, D. Weiss, M. Lipinski, and K. Eberl, *J. Appl. Phys.*, **87**, 6496 (2000)

[8] B. K. Chong, H. Zhou, G. Mills, L. Donaldson, and J. M. R. Weaver, *J. Vac. Sci. Technol.* A **19**, 1769 (2001)

[9] M. Nakamura, M. Kimura, K. Sueoka, and K. Mukasa, *App. Phys. Lett.*, **80**, 2713 (2002)

[10] G. Binnig, C. F. Quate, and Ch. Gerber, *Phys. Rev. Lett.*, **56**, 930 (1986)

[11] T. Goddenrich, H. Lemke, U. Hartmann, and C. Heiden, *J. Vac. Sci. Technol.*, **8**, 383 (1990)

[12] M. Tortonese, H. Yamada, R. C. Barrett, and C. F. Quate, *Proceedings of Transducers '91,* (IEEE, New York, 1991), 91 448

[13] E. Meyer, H. Heinzelmann, P. Grutter, Th. Jung, Th. Weisskopf, H. R. Hidber, R. Lapka, H. Rudin, H. J. Guntherodt, *J. Micros.*, **151**, 269 (1988)

[14] C. S. Smith, *Phys. Rev.*, **94**, 42, 1954.

[15] O. N Tufte and E. L. Stelzer, *J Appl. Phys.*, **34**, 313 (1963)

[16] M. Tortonese, R. C. Barrett, and C. F. Quate, *App. Phys. Lett.*, **62**, 834 (1992)

[17] E. M. Chow, G. G. Yaralioglu, C. F. Quate, and T. W. Kenny, *App. Phys. Lett.*, **80**, 664 (2002)

[18] T. L. Porter, M. P. Eastman, D. L. Pace, and M. Bradley, *Sensors and Actuators*, **88**, 47 (2001)

[19] J. A. Harley, *Advances in piezoresistive probes for Atomic Force Microscopy,* PhD. thesis, Stanford University, 2000

Chapter 2

2 Mechanical and Electrical properties of GaAs and $Al_xGa_{1-x}As$ ternary alloys

2.1 Introduction

This chapter will outline some important mechanical and electrical characteristics of GaAs and the ternary alloy $Al_xGa_{1-x}As$. The mechanical properties of GaAs and $Al_xGa_{1-x}As$ will determine the micro-cantilever's attributes, such as resonant frequency and spring constant. A thorough knowledge of the electrical properties must also exist if a Hall sensor is to be successfully integrated into the cantilever design.

Gallium arsenide (GaAs) is a III-V semiconductor and was first produced by Goldschmidt[1] in the 1920's. Since then it has played a relatively minor role in the field of microelectronics when compared with the far more common semiconductor, silicon (Si). This is especially true in the field of AFM cantilevers, where silicon is used in at least 99% of all cases. The use of GaAs as an AFM cantilever material has been reported[2] but the number of people using GaAs instead of Si is very small. The advantages of using Si are ease of growth, cost, simpler micro-fabrication techniques and readily grown oxide layers (SiO_2).

Recently, however, III-V growth techniques have developed and micromachining methods have matured so that microfabrication in GaAs is almost as simple as that in Si. The defect densities in bulk grown GaAs are still higher than those in Si, but

are now at an acceptable level from an electrical and mechanical point of view. An additional benefit of using GaAs is the ability to form the ternary alloy $Al_xGa_{1-x}As$ with the addition of aluminium (Al) to GaAs. By varying the Al mole fraction, x, the band gap of the material can be altered, in a process known as 'band gap engineering'. The use of molecular beam epitaxy to grow GaAs/$Al_xGa_{1-x}As$ epilayers, now allows high quality heterostructures to be grown with high reproducibility.

The advantages of being able to fabricate devices in GaAs/$Al_xGa_{1-x}As$ are numerous when compared to Si; GaAs has high mobility carriers and a direct band gap (which can be manipulated with the addition of Al) and these properties have led to the development of high frequency electronics and opto-electronic devices not previously obtainable with Si.

2.2 Mechanical properties

2.2.1 Crystal structure

The crystal structure for III-V compounds such as GaAs and AlAs is a zincblende arrangement as shown in Figure 2.1. The unit cell illustrated in Figure 2.1 contains 4 GaAs molecules in a volume a^3, each Ga connected to 4 As nearest neighbours and each As to 4 Ga neighbours.

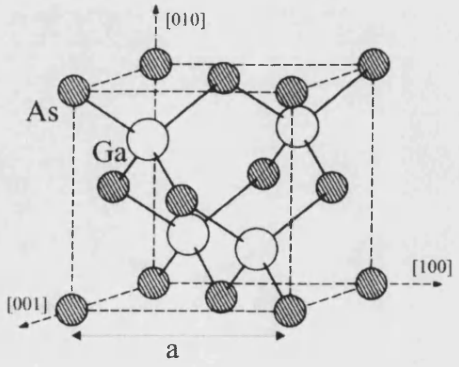

Figure 2.1 Zincblende crystal structure of GaAs

The length of each side is the lattice constant a, the total number density of atoms is $8/a^3$. The length of each bond is $a\sqrt{3}/4$.

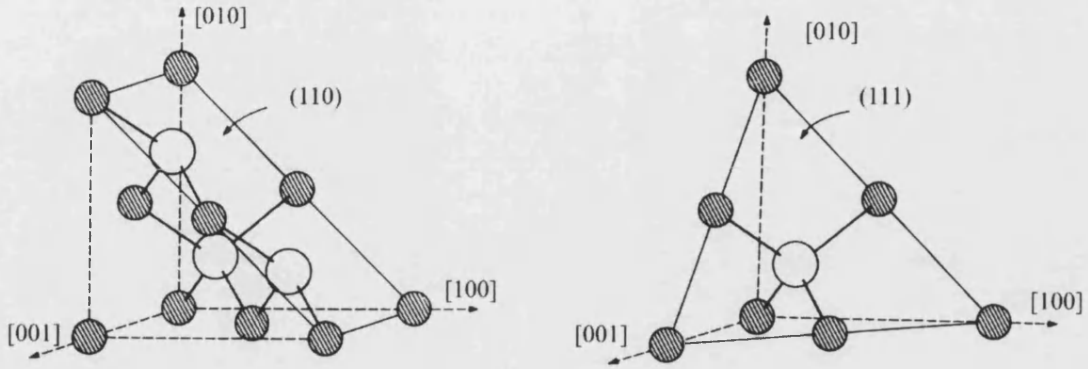

Figure 2.2 (110) and (111) planes in the Zincblende crystal structure[1]

The most important planes in the zincblende structure are the {100} planes which are normal to the principal axes as well as the {110} and {111} planes shown in Figure 2.2. The (100) plane, which is the predominant growth plane in GaAs, contains only one species of atom, alternating in successive planes of Ga and As, which are separated by $a/4$. The {110} planes are those along which GaAs most readily cleaves making it an important plane when considering device design in GaAs. Each plane contains both Ga and As atoms, so for any atom in a {110} plane it has two of its four nearest neighbours also in that plane. The third plane, the (111) plane, is also important as, like the (100) facets, it only contains one species of atom. This means the surface will be either Ga or As 'rich' resulting in different epitaxial growth and etch rates.

The crystal structure of elemental semiconductors, such as Si, exhibit inversion symmetry at all sites, due to the cubic symmetry and the absence of charge displacement within the unit cell. The compound III-V semiconductors, on the other hand, exhibit a certain deviation from inversion symmetry. This absence of inversion symmetry leads to a non-vanishing coefficient of piezoelectricity[3], making GaAs suitable for piezoelectric applications.

2.2.2 Growth

GaAs can be grown by various methods depending upon the type of material required. Bulk GaAs can grown via Liquid Encapsulated Czochralski (LEC) or Bridgman methods. These bulk methods are used to produce the substrates that, in turn, are used for epitaxial growth.

Epitaxial GaAs can be grown by various methods such as, liquid phase epitaxy, chemical vapour deposition, sputtering and metal-organic chemical vapour deposition (MO-CVD)[4], but since 1970 molecular beam epitaxy (MBE) has proved to be the pre-eminent method, with its precise control over the growth of thin GaAs and $Al_xGa_{1-x}As$ films. The strengths of MBE arise from its lower growth temperature, slow growth rate (when required), and use of shuttered, directed molecular beams. These give greater control over the growth of thin layers and variation in alloy composition as well as the ability to tailor doping profiles to a greater extent than in the other techniques[4]. The doping of GaAs and $Al_xGa_{1-x}As$ allows the modification of the material's electrical properties by precisely varying the number of carriers in the material. The addition of substitutional impurity atoms from groups II, IV or VI to the material during growth can introduce either donors or acceptors into the layer. In (100) GaAs and $Al_xGa_{1-x}As$, Si doping in the range 10^{14}-10^{18} cm^{-3} is often used to produce n-type doped layers.

2.2.3 Heterostructures

A heterostructure is a 'stack' of epilayers of differing composition grown on top of each other via an epitaxial method such as MBE or MO-CVD. The ability to grow materials with different band gaps and doping profiles on top of each other, with a sharp interface between them, has allowed the fabrication of many interesting structures leading to devices such as semiconductor lasers and high speed transistors. To be able to grow heterostructures of high quality requires the lattice

constant of the two materials to be closely matched. Figure 2.3 shows why GaAs and $Al_xGa_{1-x}As$ alloys are well suited to heterostructure growth as the lattice constants are almost identical.

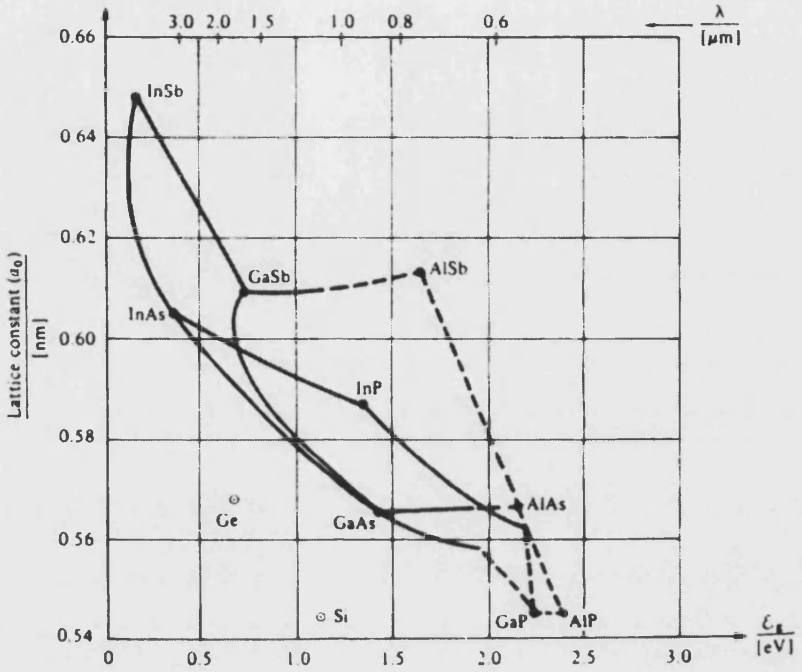

Figure 2.3 Plot of the lattice constant *a* against band gap energy for various semiconductors[7]

GaAs and AlAs have lattice constants of 0.56533nm and 0.5611nm and the alloy $Al_xGa_{1-x}As$ has a lattice constant which is can be estimated by a linear interpolation of the two:

$$a_{(AlxGa1-xAs)} = 0.56533 + 0.00078x \text{ nm} \qquad (2.1)$$

Good GaAs/$Al_xGa_{1-x}As$ heterostructures can be grown for $x<0.5$, but the surface roughness increases as the Al fraction, x, increases above this.

2.2.4 Young's Modulus

For crystals such as GaAs, the elasticity constants (Young's modulus, Poisson's ratio), depend upon the crystal orientation. The Young's modulus, *E,* in a given crystal direction can be calculated according to[5]

$$E^{-1} = S_{11} - 2\left(S_{11} - S_{12} - \frac{1}{2}S_{44}\right)\left(l_1^2 l_2^2 + l_2^2 l_3^2 + l_1^2 l_3^2\right) \qquad (2.2)$$

where S_{ij} are the elastic compliance coefficients of the material and l_k are the directional cosines (see Appendix A).

Crystal Direction	Young's Modulus E (GPa)
[100]	85.5
[110]	122
[111]	137

Table 2.1 Young's Modulus of GaAs for the main crystallographic directions calculated from eqn. 2.1 and Table 2.2

Using this expression it is possible to determine the Young's modulus for any crystal direction. The Young's modulus for the main crystal directions are given in Table 2.1. A polar plot of the variation of Young's modulus with crystal direction is shown in Figure 2.4

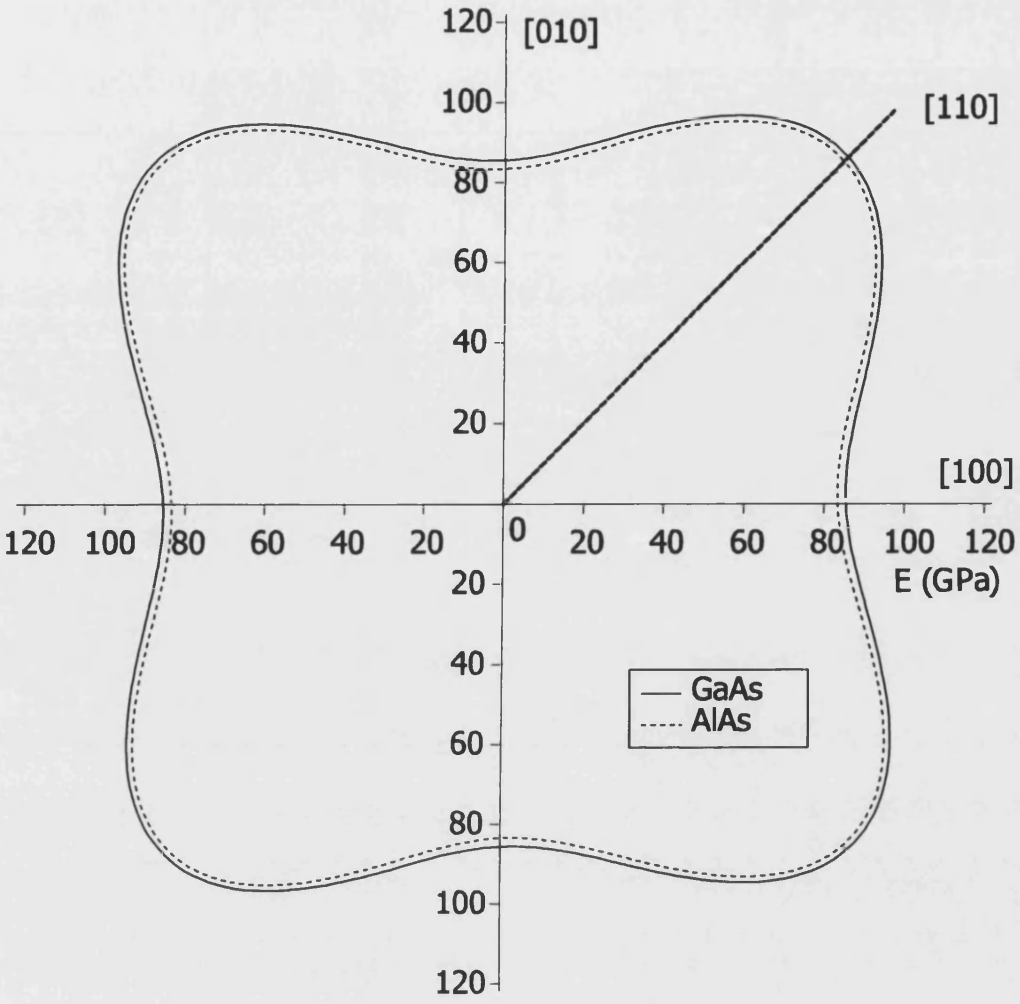

Figure 2.4 The (001) cross-section of the Young's modulus surface of GaAs and AlAs calculated from eqn 2.1 and Table 2.2

2.2.5 Bulk material parameters for GaAs, AlAs and $Al_xGa_{1-x}As$

The main mechanical constants used in the project are outlined in Table 2.2. Values are given for both GaAs and AlAs and the alloy $Al_xGa_{1-x}As$.

	GaAs	AlAs	$Al_xGa_{1-x}As$
Lattice Constant *a* (nm)	0.56533	0.56611	0.56533 + 0.00078x
Crystal Density (Kg/m^3)	5360	3760	5360 - 1600x
Elastic compliance constant S_{ij} ($x10^{-11} Pa^{-1}$)			
S_{11}	11.7	12	11.7 + 0.3x
S_{12}	-3.7	-3.9	-3.7 - 0.2x
S_{44}	16.8	17	16.8 + 0.2x
Young's Modulus *E* (GPa) <110>	122	120	122 - 2x
Poisson's ratio *P*	0.31	0.32	0.31 + 0.01x

Table 2.2 Structural and mechanical properties of GaAs, AlAs and $Al_xGa_{1-x}As$[6]

2.3 Electrical properties

2.3.1 Band Structure

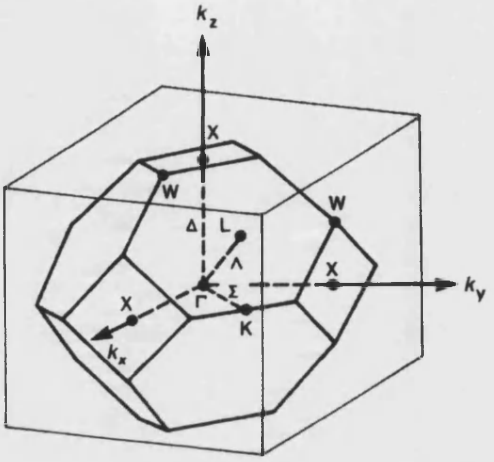

Figure 2.5 First Brillouin zone for the fcc, diamond and zincblende lattices[7]

The relationship between k, the crystal momentum represented by a point in the first Brillouin zone, and the energy E(k), is known as the energy band structure and is an important tool for describing the electrical (and optical) properties of semiconductors.

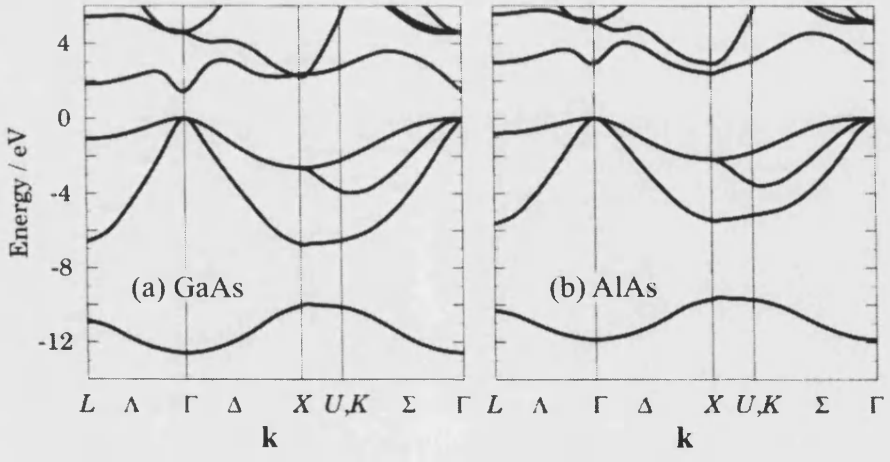

Figure 2.6 Band structure of (a) GaAs and (b) AlAs (not including spin-orbit coupling)[8]

The band structure of a material can be measured experimentally, but this usually only yields data for certain regions in the Brillouin zone. Theoretical methods have been developed to produce full band structures like those in Figure 2.6. The zero of energy is conventionally taken as the top of the valence band.

From Figure 2.6(a) it can be seen that the conduction band minimum in GaAs is at the Γ point. This is the same point in k-space as the top of the valence band and therefore GaAs has a direct band gap. Optically this is important as photons alone can excite electrons across the band gap. AlAs, however, has its conduction band minimum at the X point, making it an indirect band gap semiconductor (and unsuitable as an optical device material). By varying the aluminium fraction x in $Al_xGa_{1-x}As$ the properties of the material change continuously from that of GaAs to AlAs with some interesting effects for $0<x<0.5$. The effect on the band gap for increasing AlAs content can be seen in Figure 2.7, the band gap increases in energy until $x\sim0.45$ where the X minima fall bellow the Γ minimum, changing from a direct to an indirect band gap material.

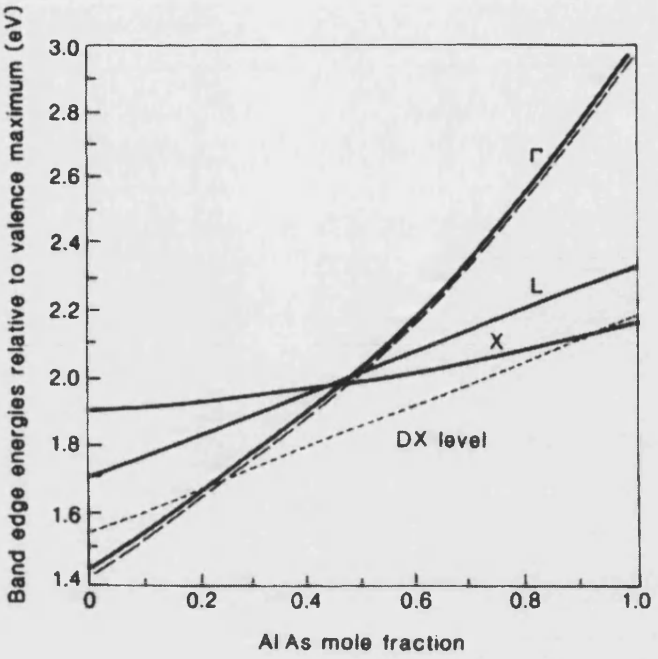

Figure 2.7 Optical data on band gaps at the Γ, X and L points in bulk GaAs and $Al_xGa_{1-x}As$ alloys; the broken line parallel to the Γ point curve indicates the energy of the shallow donor levels. The line marked DX refers to the energy levels of deep defects in $Al_xGa_{1-x}As$

2.3.2 DX Centres

DX centres arise in association with n-doping of $Al_xGa_{1-x}As$. While for $x < 0.2$ the doping with group-VI or group-IV elements produces normal shallow donors, for $x > 0.2$ deep donors appear in addition to the shallow ones, independent of the nature of the dopant and the epitaxial-growth method[9].

The DX centres trap electrons at these deep donor sites and the energy required to thermally ionize the dopant impurities (known as the thermal ionization energy) increases from the hydrogenic donor binding energy of ~5 meV by more than one order of magnitude to ~0.1 eV[10]. The centre exhibits a higher-energy metastable (or long-lived) conducting state which can be excited optically. As a result samples

containing these centres exhibit persistent photoconductivity (PPC) at low temperatures (<100K), i.e. their conductivity is greatly increased by light irradiation but, unlike ordinary photoconductivity, the sample remains in this conducting state for a very long time even after the light is turned off. The rate of decay of this state depends strongly on the type of the donor atom to which the DX centre is related. In the case of the silicon-related DX centres the PPC decays very slowly, of the order of days.

2.3.3 Conductivity, Effective Mass and Mobility

The Drude model of conductivity is a simple way of describing the conduction process for free electrons in a solid. The current density, j, is given by

$$j = \sigma E \tag{2.3}$$

where E is the electric field and the conductivity, σ, is described by

$$\sigma = \frac{ne^2\tau}{m} \tag{2.4}$$

This equation relates the conductivity to the carrier density n, the electron mass m and the momentum scattering time τ. The mobility is given by

$$\mu = \frac{e\tau}{m} \tag{2.5}$$

However when an electron is in a solid it is not strictly 'free' and its mass m_0, is replaced by the effective mass m^* which, in the conduction band in GaAs near the Γ point, can be assumed to be constant and given by the parabolic E-k relationship

$$E = \frac{\hbar^2 k^2}{2m^*} \tag{2.6}$$

which results in an effective mass of $0.067m_0$ [6]. From eqn 2.5 a smaller effective mass leads to a higher mobility. The mobility is also dependent upon the momentum scattering time τ, which is determined from many different scattering mechanisms in a solid. The reduction of some of these mechanisms can be achieved by *modulation doping* as described in the next section.

2.3.4 Modulation doping

The doping of semiconductors is used to introduce carriers in addition to the intrinsic carriers already present. Unfortunately the charged donor or acceptor which is left behind when electrons or holes are released now becomes an obstacle to the carriers via ionized impurity scattering. This scattering severely reduces the mobility of the carriers.

To overcome this problem *modulation doping* can be used to separate the carriers from the ionized impurities. This is illustrated for a heterojunction between n-AlGaAs, AlGaAs and undoped GaAs in Fig. 2.8. A thin capping layer is grown to prevent oxidation of the AlGaAs layer. The electrons are liberated from the donors and are free to diffuse and will eventually cross the heterojunction into the GaAs layer. There they lose energy and become trapped because they cannot climb the barrier presented by ΔE. This motion separates the negatively charged electrons from their positively charged donors and sets up an electrostatic potential that pulls the electrons back towards the ionized donors in the n-AlGaAs.

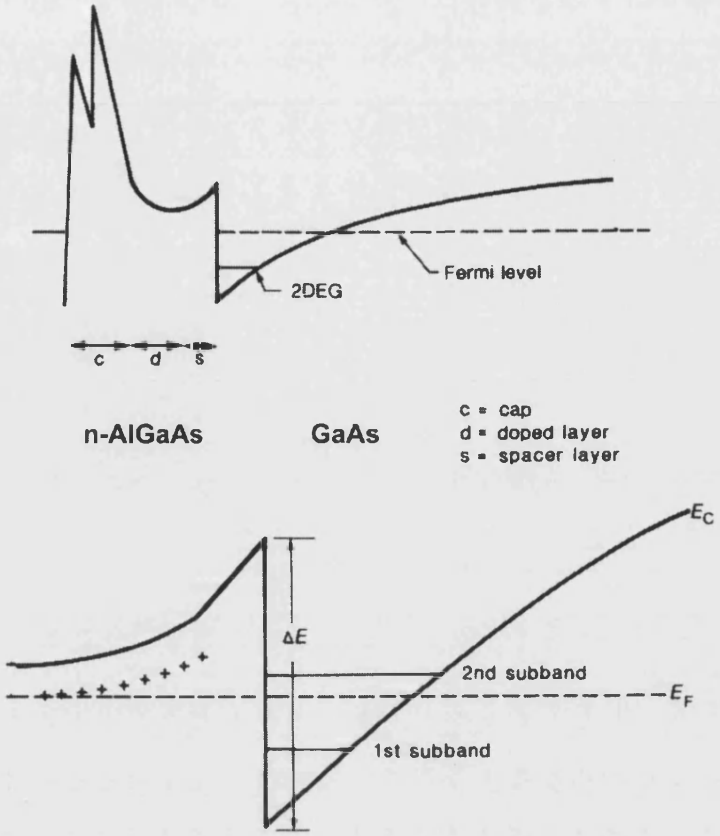

Figure 2.8 Formation of the two-dimensional electron gas (2DEG) using modulation doping. The profile is in a direction perpendicular to the wafer surface

The discontinuity has an important effect because it prevents the induced electric field from returning the electrons to their donors; this field can only squeeze the electrons against the interface, where they are trapped in a roughly triangular potential well. This well is typically about 10nm wide. The energy levels for motion along the z direction are quantized in a similar way to those in a square well and often only the lowest level is occupied. All electrons then occupy the same bound state in the z-direction but remain free in the x and y directions. This heterostructure is known as a two-dimensional electron gas or 2DEG.

Thus modulation doping has achieved two benefits: it has separated electrons from their donors to reduce scattering by ionized impurities, and confined the electrons to

two dimensions. Further refinements can be made by introducing a spacer layer of undoped AlGaAs between the n-AlGaAs and GaAs which increases the separation between electrons and the ionized donors. The effect this has on the mobility of the electrons is very dramatic and at low temperatures mobilities of $>10^6$ $cm^2V^{-1}s^{-1}$ are achievable.

2.3.5 Piezoresistivity

Piezoresistivity is defined as a change in the electrical resistance of a material when it is subject to an applied stress. The magnitude of the change in resistance is a product of the stress in the material and the piezoresistive coefficient of the material.

The fractional change in resistivity $\Delta\rho/\rho$ can be written in terms of transverse and longitudinal stresses.

$$\frac{\Delta\rho}{\rho} = \pi_T\sigma_T + \pi_L\sigma_L \qquad (2.7)$$

The longitudinal coefficient, π_L, refers to the case where the applied stress is in the same direction as the electric field, whereas the transverse coefficient, π_T, refers to the case where the applied stress is perpendicular to the electric field.

The physical mechanisms that cause piezoresistivity in a material are not always the same for each type of material. The piezoresistive effect in semiconductors was first reported in silicon and germanium in 1954 for single crystals[11]. In Si the piezoresistive effect is due to a modulation in the average mobility in response to a uniaxially applied stress. It is therefore crystal direction-dependent and has a maximum in the [111] direction. It was found that by diffusing p-type impurities into Si[12] even larger piezoresistive sensitivities could be achieved. It is for this reason that most piezoresistive based AFM cantilevers use p-type Si as a sensing element.

Piezoresistivity in GaAs and the $Al_xGa_{1-x}As$ alloys differs from that in Si as it has piezoresistive response for hydrostatic pressure. This means that piezoresistance should be observable for strain in all crystal orientations. The use of Bulk GaAs as a piezoresistive material has not been common due to its characteristically low piezoresistive coefficient[13], but the ternary alloy $Al_xGa_{1-x}As$ can be tailored to give large piezoresistive coefficients by varying the Al content. In $Al_xGa_{1-x}As$ there are four different mechanisms which lead to piezoresistivity and the first three described below are independent of the crystal direction[3].

One mechanism is due to the change of the electron effective mass m^* with applied pressure. From eqn 2.5 an increase in effective mass leads to a reduction in conductivity. A typical piezoresistive response[3] arising from this is ~$1x10^{-10}$ Pa^{-1}.

A second mechanism is a pressure induced transfer of electrons from the high mobility band gap minimum $\Gamma\left(m_\Gamma^* = 0.067m_0\right)$ to the low mobility X $\left(m_X^* = 0.32m_0\right)$ band due to a relative change in the energy of the conduction band minima. In $Al_xGa_{1-x}As$ the effect gets more pronounced as the Al fraction nears the direct-indirect crossover point at x~0.45 shown in Fig, 2.7. A typical response[3] for this effect is ~$10x10^{-10}$ Pa^{-1}.

A third mechanism arises in $Al_xGa_{1-x}As$ due to deep donor states, known as DX centres. At aluminium fractions >0.2 these donor states rise in energy above the Γ minimum as shown in Fig 2.7. These DX centres can trap additional electrons with the application of stress and alter the resistivity of the $Al_xGa_{1-x}As$. The optimum Al fraction has been found to x ~ 0.33[3]. Piezoresistivity responses of ~$40x10^{-10}$ Pa^{-1} have been measured.

The fourth response mechanism is slightly different from the others, being direction dependent and the response being a function of the *stress gradient* rather than the stress. Stress gradient induced piezoelectric bound charges are used to change the

resistivity in a diffused resistor. By the use of stress amplifying stripes patterned into the resistor, responses of ~$10x10^{-10}$ Pa^{-1} have been measured[3].

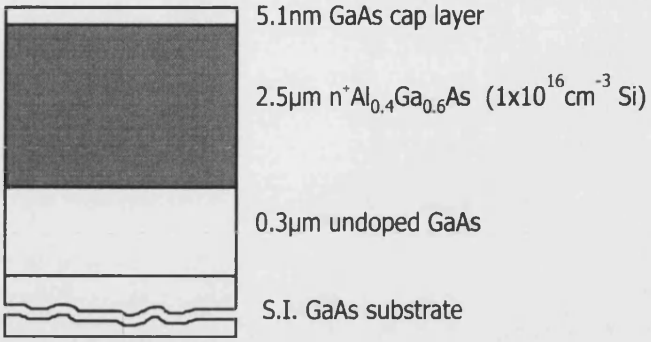

Figure 2.9 Test epilayer structure used for measurement of piezoresistive coefficient

Piezoresistivity measurements on a test epilayer structure shown in Fig 2.9 were carried out to determine the piezoresistive coefficient of $Al_{0.4}Ga_{0.6}As$. The results are shown in Fig 2.10. The graph shows the fractional resistance change as a function of applied stress along the [011] direction, which in this case was applied by loading the material with known weights. At room temperature a value of $134x10^{-11}$ Pa^{-1} for the piezoresistive coefficient is obtained, which compares favourably with the value for p-type silicon in the [110] direction of ~$72x10^{-11}$ Pa^{-1} (300K)[14]. The measurements also show an increase in response at low temperatures.

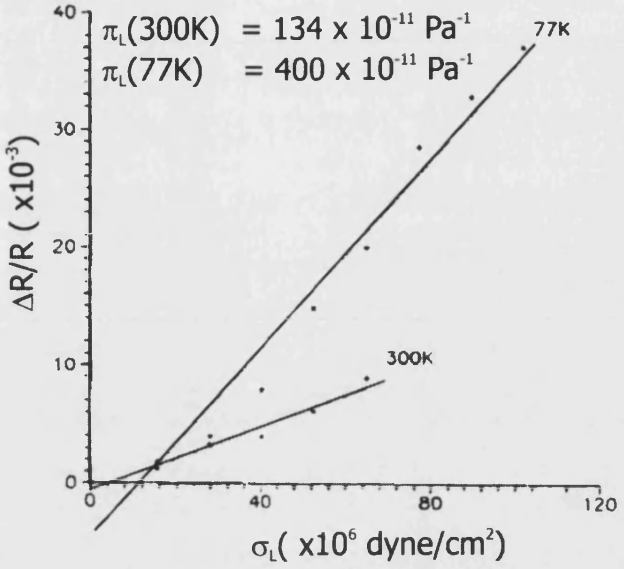

Figure 2.10. Longitudinal piezoresistive coefficient via stress measurements on 2.5μm $Al_{0.4}Ga_{0.6}As$ epilayer[15]

2.3.6 Electrical parameters for GaAs, AlAs and $Al_xGa_{1-x}As$

The main electrical constants used in the project are outlined in Table 2.3. Values are given for both GaAs and AlAs and the alloy $Al_xGa_{1-x}As$.

	GaAs	AlAs	$Al_xGa_{1-x}As$
Band Gap energy (eV)	1.424*	2.168*	1.424 + 1.247x (x <0.45) *
			1.900 + 0.125x (x >0.45) *
Effective mass			
Γ valley m_Γ^*	$0.067m_0$*	$0.150m_0$*	...
X valley m_X^*	$0.32m_0$*	$0.26m_0$*	...
L valley m_L^*	$0.11m_0$*	$0.14m_0$*	...
Piezoresistive coefficient			
p-GaAs π_L (10^{-11} Pa^{-1})	16.7†	...	...
n-$Al_{0.4}Ga_{0.6}As$ π_L (10^{-11} Pa^{-1})	...	...	134 (300K)‡
			400 (77K)‡

Table 2.3 Electrical properties of GaAs, AlAs and $Al_xGa_{1-x}As$

* From 6

† From 13

‡ From 15

2.4 References

[1] J. S. Blakemore, *J. Appl. Phys* **53,** R123-R181 (1982)

[2] S. Heisig, H. U. Danzebrink, A. Leyk, W. Mertin, S. Munster, E. Oesterschulze, *ULTRAMICROSCOPY*, **71**, 99 (1998)

[3] K. Hjort, J. Soderkvist and J. Schweitz, J. Micromech. Microeng. **4**, 1 (1994)

[4] E. H. C. Parker, *The Technology and Physics of MBE*, Plenum Press, (1985)

[5] R. I. Cottam and G. A. Saunders, *J. Phys C* **6,** 2105-2118 (1973)

[6] S. Adachi, *J. App. Phys.* **58**, R1-R29 (1985)

[7] M. J. Kelly, *Low dimensional semiconductors*, OUP, (1995)

[8] J. H. Davies, *The Physics of low-dimensional semicond*uctors, Cambridge University Press, (1998)

[9] K. Zdansky, I. D. Hawkins, *Czech. J. Phys.*, **49**, 813 (1999)

[10] P. Y. Yu, M. Cardona, *Appendix 4.1 A Prototypical Deep Center in n-type Zincblende-Type Semiconductors: The DX Center, Fundamentals of Semiconductors,* Springer Verlag (2003)

[11] C.S. Smith, *Phys. Rev.*, **94** (1), pp. 42-49 (1954)

[12] O. N Tufte and E. L. Stelzer, *J Appl. Phys.*, **34**, 313 (1963)

[13] A. Dehe, K. Fricke, K. Mutamba and H. Hartnagel, *J. Micromech. Microeng.* ***5***, 139 (1995)

[14] J. A. Harley, *Advances in piezoresistive probes for Atmoic Force Microscopy,* PhD. thesis, Stanford University, 2000

[15] Data supplied by Dr. A. Oral, University of Bath

Chapter 3

3 Integrated Sensor Design

3.1 Introduction

This chapter will discuss the design process for the fabrication of an integrated AFM cantilever and Hall sensor. This follows three steps, firstly the cantilever design i.e. its shape, length, width and thickness. Secondly the Hall probe design, which is influenced by the cantilever design, and thirdly the heterostructure design, a vital step when integrating the two sensors onto one cantilever.

3.2 Cantilever Design

The design of our cantilever has to satisfy three main criteria

- Sensitivity to deflection (or force depending upon the type of measurement required).
- To be within GaAs fabrication limitations (e.g. optical lithography resolution and materials parameters).
- Allows the integration of two sensors.

Cantilever sensitivity is dependent upon the cantilever geometry and the piezoresistive coefficient of the cantilever material. The first piezoresistive cantilever was reported by Tortonese *et. al.*[1] and their design has been the template

for most piezoresistive cantilever designs since. They cite the two main parameters influencing piezoresistive cantilever performance as the spring constant and minimum detectable deflection (MDD)[2], both of which will discussed later in this section.

The limitations imposed by the cantilever fabrication process will be further discussed in Chapter 4 but, as a guide, an approximate minimum feature size of ~1μm is imposed by the use of optical lithography techniques.

The integration of the two sensors is a more open-ended criterion than the other two criteria, both of which will determine how the two sensors need to be integrated. However, the integration of the sensor needs to be the ultimate goal of the project and, as such, needs to be carefully considered at each stage of the design.

3.2.1 Sensitivity

For a piezoresistive cantilever the sensitivity is a measure of the fractional change in resistance to a given displacement/force. This fractional resistance change is usually detected using a Wheatstone bridge arrangement as in Figure 3.1.

The Wheatstone bridge is an arrangement of three almost identical resistors with values equal to that of the unstressed piezoresistor. The bridge is biased with a voltage, V, and any change in the piezoresistor resistance, ΔR, is seen as a voltage difference $V_2 - V_1$.

$$V_2 - V_1 = \Delta V = V\frac{\Delta R}{4R} \tag{3.1}$$

The sensitivity, S, to a deflection, Δz, is usually written

$$S = \frac{\Delta V}{\Delta z} = \frac{V}{4}\frac{\Delta R}{R\Delta z} \tag{3.2}$$

In AFM literature, sensitivity is more often quoted as $\Delta R/(R\Delta z)$ as this is independent of bridge voltage. The sensitivity, whilst important, does not define the resolution of the cantilever as the resolution is dependent on noise in the measurement system which results in the minimum detectable deflection (MDD) which will be discussed in Chapter 5.

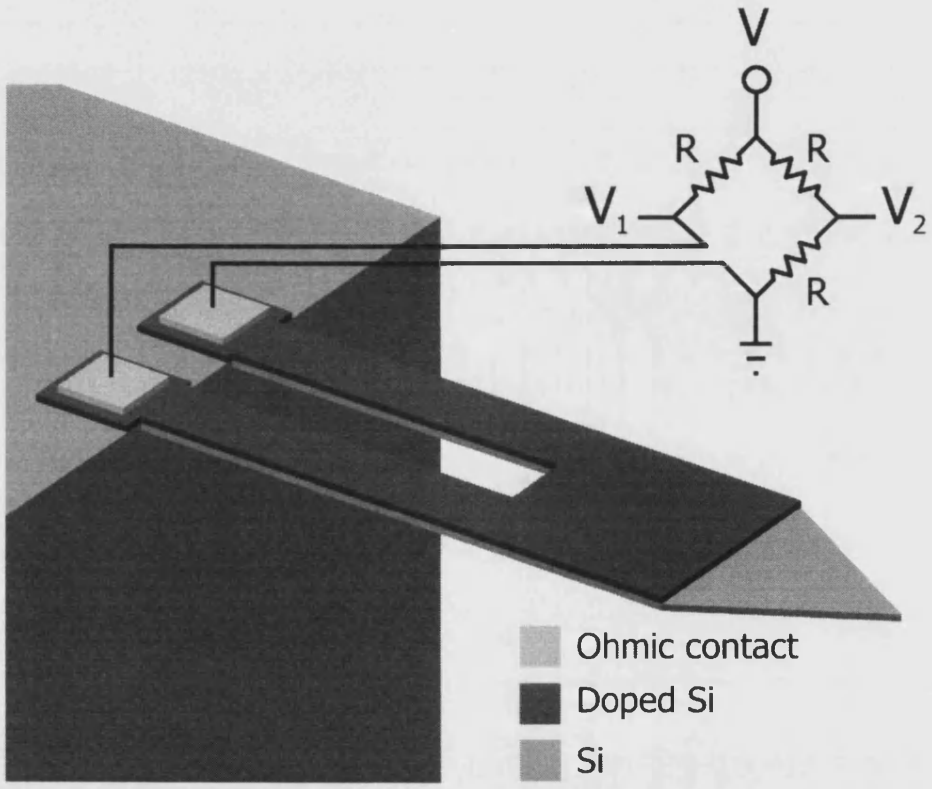

Figure 3.1 Piezoresistive detection using a Wheatstone bridge

3.2.2 Cantilever Shape

One of the first design decisions is the cantilever shape. Many different designs have been reported in the literature and they can be broadly grouped into one of three categories, rectangular[3] (Figure 3.2(a)), triangular (Figure 3.2(c)) and rectangular with triangular tip (Figure 3.2(e)). A common variation on each of these designs, is to remove the centre of the cantilever to leave two legs supporting the cantilever as shown in Figure 3.2(b,d,f),.

The first design, Figure 3.2(a), is a simple rectangular beam and is a popular design due to its ease of fabrication, indeed the first AFM by Binnig *et. al.*[3] was a rectangular design with a diamond tip.

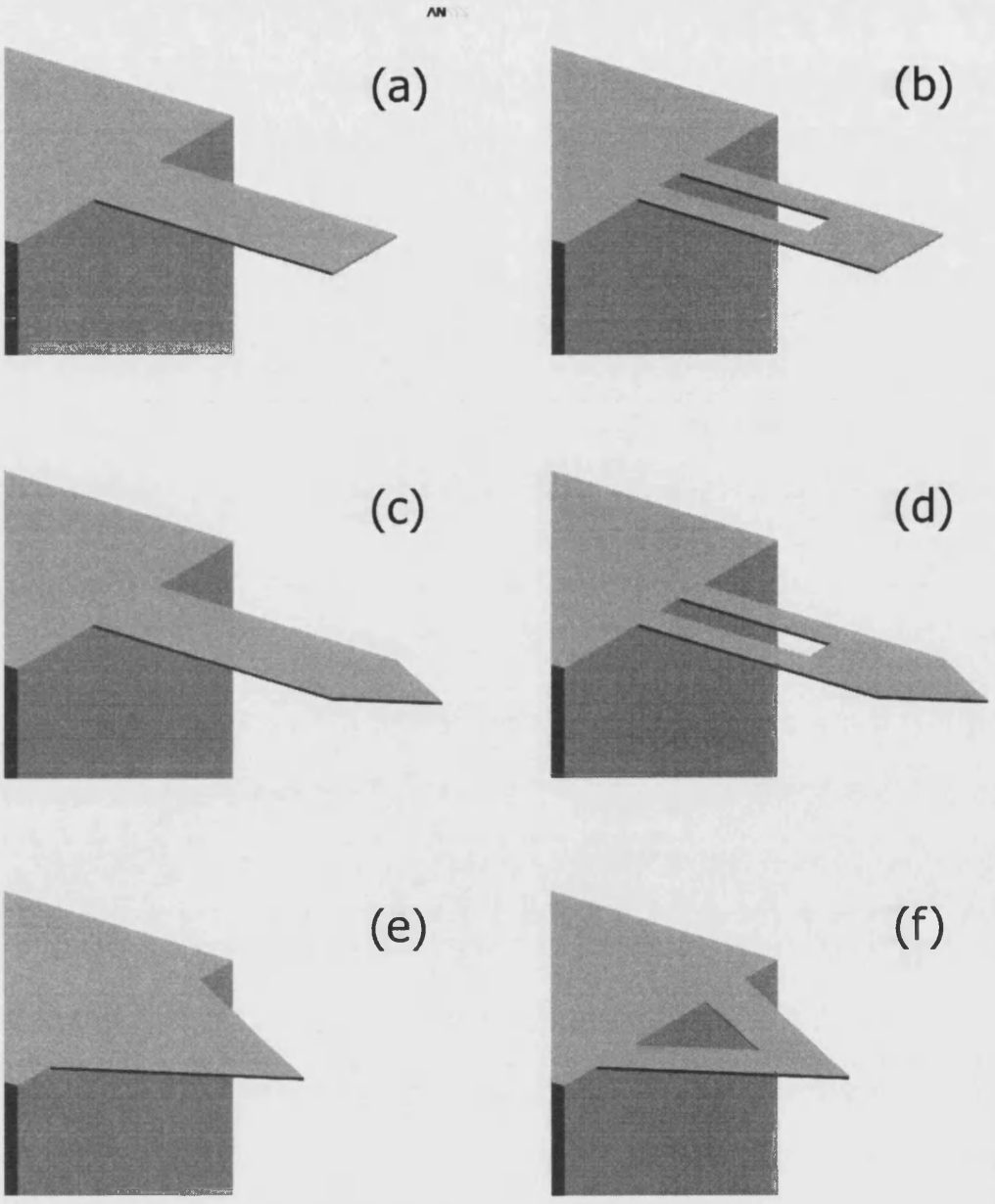

Figure 3.2 Common AFM cantilever designs

The most common piezoresistive designs are based on the cantilevers shown in Figure 3.2 (d)[1] and (f)[4] and are almost exclusively fabricated from silicon. Design (d), first reported by Tortonese *et al.*[1], has three advantages over (a). Firstly the legs define the piezoresistor, requiring no further fabrication to define the piezoresistor. Secondly, by removing the centre section the stress in the two legs is concentrated in the piezoresistive leg regions, and lastly the triangular tip negates the need for a sharp tip for imaging relatively flat samples. Cantilever (f), a triangular cantilever, is

also a two leg design and has the advantage of a roughly constant stress distribution across its surface and a higher resonant frequency. They are also popular due to their perceived resistance to lateral forces in comparison to rectangular cantilevers, though this has recently been shown to be incorrect[5] and the converse to be true, the triangular cantilevers being less stable.

From an integration viewpoint cantilevers (b), (d) and (f) were considered unsuitable due to their reduced surface area which, in turn, would limit the area available to accommodate the two sensors. A novel solution to this problem was recently reported by Willemin *et. al.*[6], showing that it is possible to integrate a second sensor, a current loop, onto a type (d) cantilever by using a third leg to carry the interconnects to the sensor at the end of the cantilever.

During the prototype stages of the project, cantilevers of shape type (c) (Figure 3.3 (a)) were used, as only the piezoresistive element was fabricated, with no tip or Hall probe present. Later designs (Figure 3.3(b,c)) were based on cantilever Fig. 3.2(a) with slight modifications to the rectangular shape as these were found to be more suited to the integration of the two sensors.

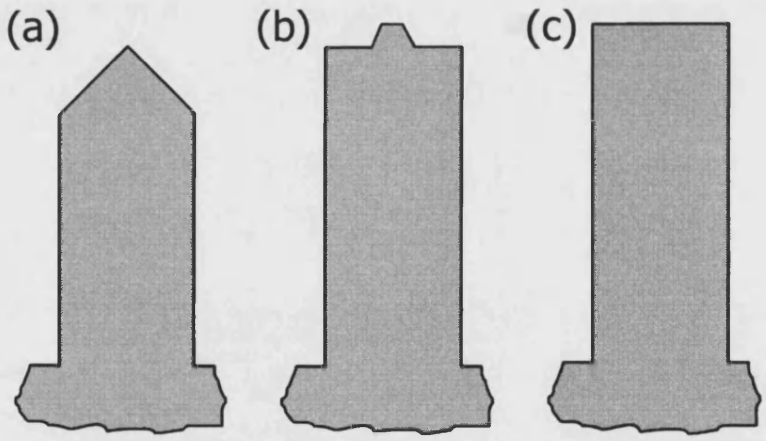

Figure 3.3 Three cantilever designs used during the project

3.2.3 Spring Constant and resonant frequency

The spring constant is a fundamental parameter when designing a cantilever as it determines how the cantilever reacts to a given force. It is a measure of the cantilever 'stiffness', the larger the spring constant the stiffer the cantilever. As discussed in Chapter 1 the spring constant determines the way the cantilever interacts with the sample. The relationship between the spring constant and the resonant frequency is important as it determines the size scale of the cantilever. It is because of this relationship that micromachined cantilevers are required for AFM.

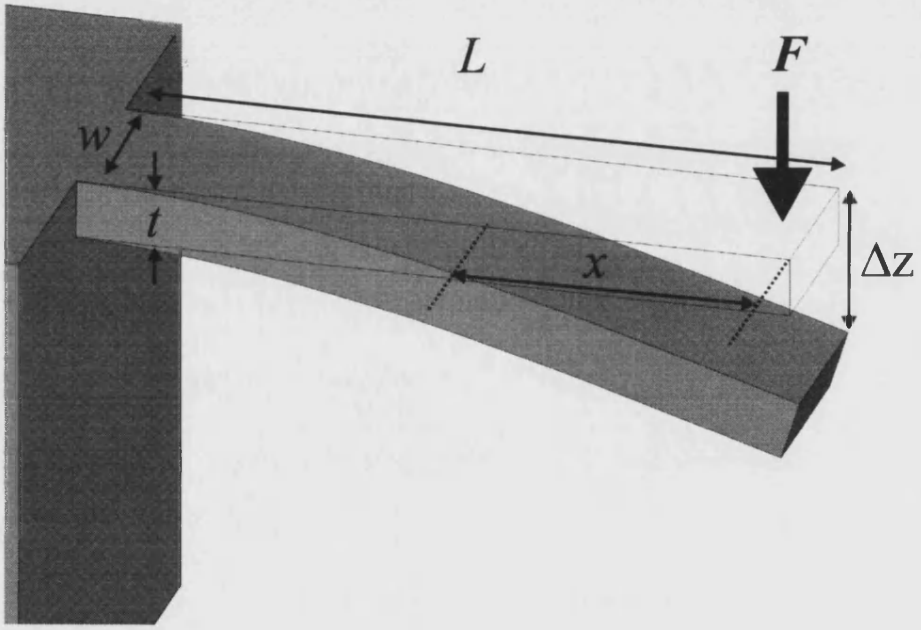

Figure 3.4 Cantilever beam with force acting on the tip

The spring constant is defined by Hooke's Law which states[7]:

Up to some maximum load (known as the limit of proportionality) the extension of a spring is proportional to the applied load.

Hence for small cantilever deflections we can write

$$F = k\Delta z \tag{3.3}$$

where F is the force, Δz the deflection and k is the spring constant. For a rectangular cantilever like Figure 3.2(a) the spring constant is well described by the following expression (Appendix B)

$$k = \frac{Ewt^3}{4L^3} \tag{3.4}$$

where E is the Young's modulus of the cantilever material and dimensions L, w and t are defined in Figure 3.4. From eqn. 3.4 it can be seen that the spring constant is most influenced by cantilever thickness and length. A short thick cantilever would have a large spring constant and a long thin cantilever a small spring constant.

With regard to AFM imaging, stiffer cantilevers are used in non-contact mode as this allows higher sensitivity to deflection and prevents cantilever 'snap down' due to the attractive van der Waals forces. Commercial non-contact cantilevers usually have spring constants ~20 N/m. Small spring constant cantilevers are mainly used in contact mode for measurements of ultra small forces (~100pN) for which cantilevers with spring constants as small as 5×10^{-5} N/m have been reported[8].

The spring constant of the cantilever will therefore determine the overall size of the cantilever. For this project it was decided that NC-AFM/IC-AFM modes would be the most suitable modes of operation, setting a minimum value of spring constant of 10N/m. If we use a rectangular cantilever in our prototype design we can calculate the basic dimensions of the cantilever.

3.2.3.1 Resonant frequency

The natural frequency of the cantilever is related to the spring constant by the following expression[9],

$$f_0 = \frac{\alpha_n}{2\pi}\sqrt{\frac{k}{m}} = \frac{\alpha_n}{4\pi}\frac{t}{L^2}\sqrt{\frac{E}{\rho}} \tag{3.5}$$

where m is the mass of the cantilever, t the cantilever thickness, L the length, ρ the density and α_n are the numerical constants for each normal mode, the first three values being

$$\alpha_n = 2.03, 12.72, 35.62, \ldots$$

where α_1 is the fundamental mode. As the cantilever is to be used in NC-AFM mode it will be operated at a frequency close to its fundamental resonance, a value of considerable importance as it sets the upper limit for the AFM measurement bandwidth, which in turn limits the AFM scan speed. A high resonant frequency also helps suppress 1/f noise present in the measurement, which will be discussed later. Therefore, in order to reduce the spring constant for use in AFM and keep the resonant frequency high enough for a suitable bandwidth, the cantilever mass has to be small. It is for this reason that micromachined cantilevers are used in AFM measurements.

3.2.3.2 Cantilever dimensions

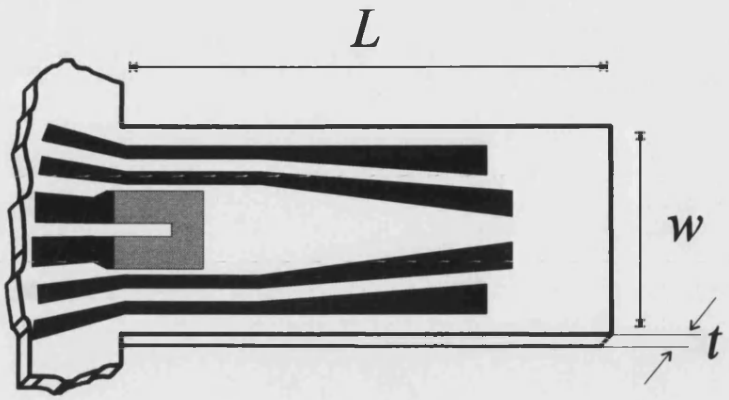

Figure 3.5: Schematic of the three main cantilever dimensions

We are now in a position to determine the main geometrical dimensions of the cantilever. From eqn. 3.4, it is apparent the width is the least important of the dimensions in determining the spring constant and can be assigned dimensions by considering that it needs to be wide enough to fabricate six leads to contact the piezoresistor and the Hall probe as in Figure 3.5. In order to satisfy these considerations a cantilever width of 160μm was chosen. The length and thickness can now be calculated for a range of spring constants and resonant frequencies as in Figure 3.6.

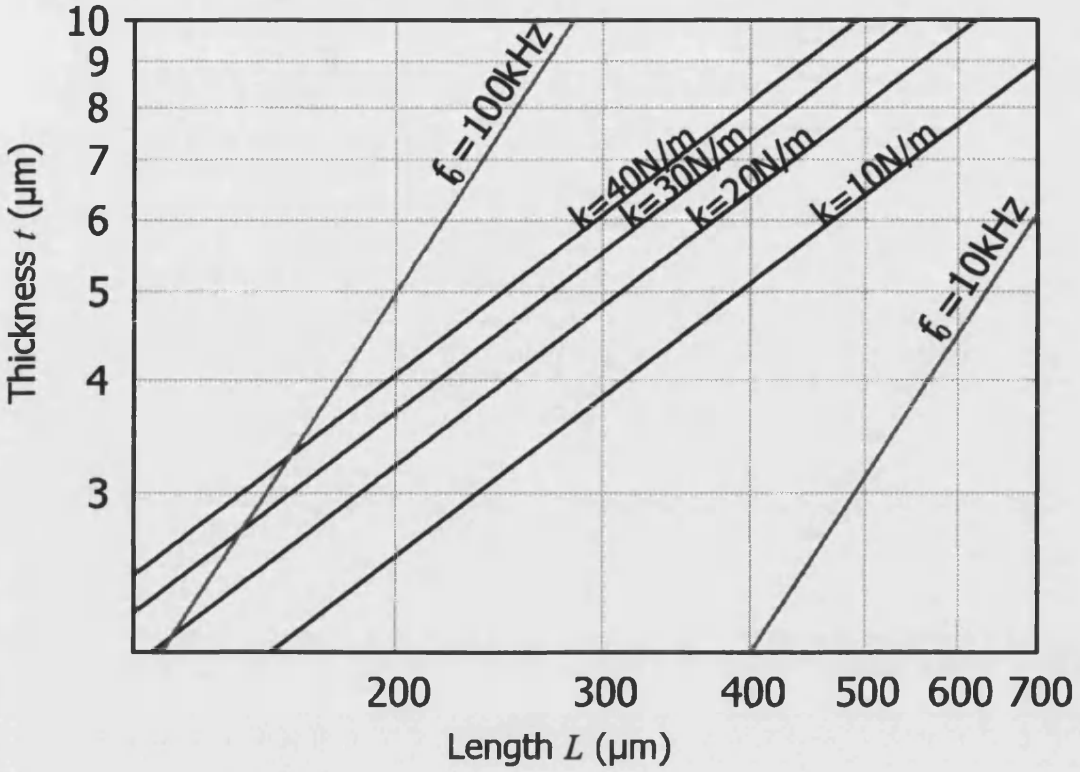

Figure 3.6: Cantilever length vs. thickness for a set of values of spring constant and resonant frequency

The graph shows that for spring constants in excess of 10N/m the resonant frequency is above 10kHz, which would be a minimum working frequency for NC-AFM. The chosen length and thickness was 400µm and 6µm respectively, giving a spring constant k~15N/m and a resonant frequency f_0 = 30.1kHz.

3.2.4 Stress in a cantilever beam

To determine the most suitable placement of the piezoresistive sensor, i.e. the region of highest stress, the stress distribution needs to be known. The stress in a beam undergoing a deflection Δz as in Figure 3.4 is given by (Appendix B)

$$\sigma = \frac{My}{I} \tag{3.6}$$

where the bending moment M = $F(L - x)$, I is the moment of inertia and y is the distance from the neutral axis. This then gives

$$\sigma = \frac{12F(L-x)y}{wt^3} \tag{3.7}$$

The stress distribution is illustrated using finite element analysis (FEA) in Figure 3.7.

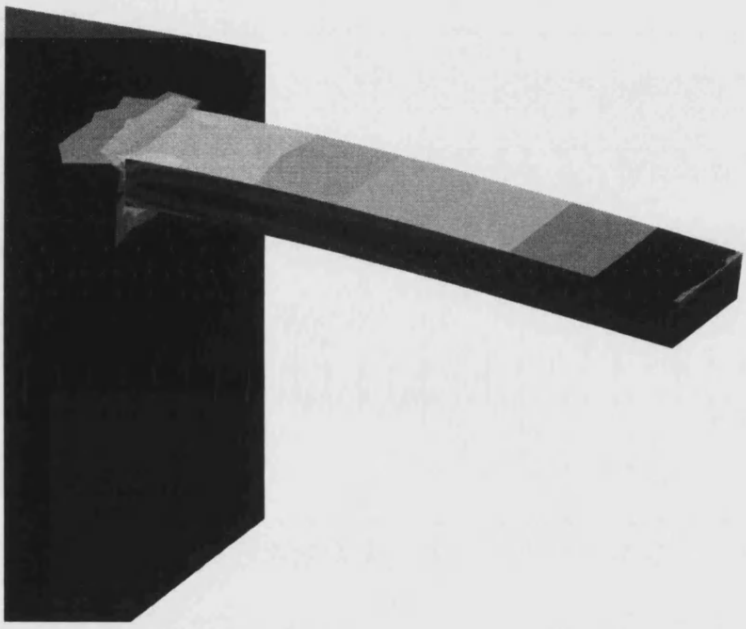

Figure 3.7 Finite element analysis of a stressed beam. Stress varies linearly down through and along the cantilever

The top half of the cantilever is in tensile stress and the bottom half is in compression. At the centre of the beam is a layer called the neutral axis, which experiences zero stress. To first order approximation, the stress distribution increases linearly from a minimum at the tip of the cantilever to a maximum at the base. The stress also varies linearly across the thickness with a minimum at the neutral axis and maximum at either surface. Eqn. 3.6 is a simplified expression of

the real stress as it does not account for the stress in regions such as corners where the cantilever meets its support.

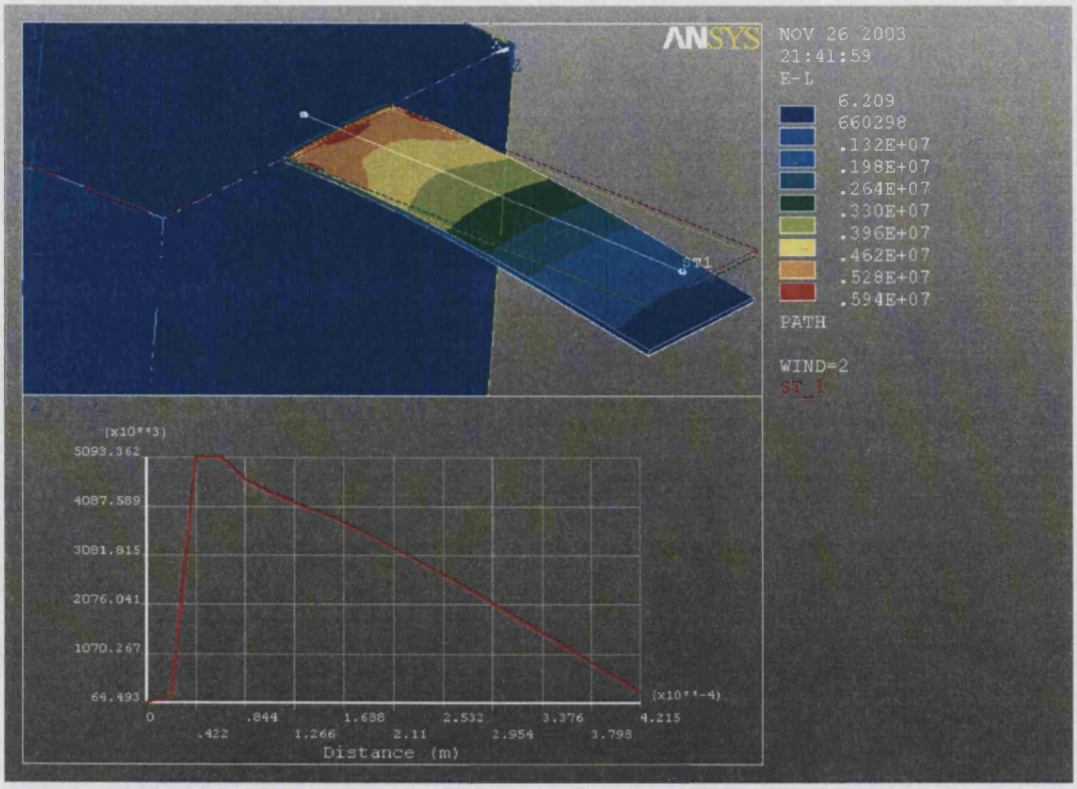

Figure 3.8 (1)The variation of stress along the length of the cantilever due to a deflection of 1μm. (2) The graph plots the path given by ST1. It can be seen the stress extends into the substrate but quickly falls to zero.

We can now place our piezoresistive element in the region of maximum stress. We know that this occurs at the surface and the base of the cantilever. An ideal piezoresistor would therefore be infinitesimally small as it would occupy only the region of maximum stress. In real cantilevers, however, a minimum size is set by fabrication limits.

3.2.5 Piezoresistive sensitivity

Knowing the stress in the cantilever, we can now estimate the response of the piezoresistive sensor to an applied stress. Using eqn. 2.8 and considering only the longitudinal stress we can write

$$\frac{\Delta R}{R} = \pi_L \langle \sigma \rangle \tag{3.8}$$

where π_L is the longitudinal piezoresistive coefficient and $\langle \sigma \rangle$ is the average stress in the piezoresistive element.

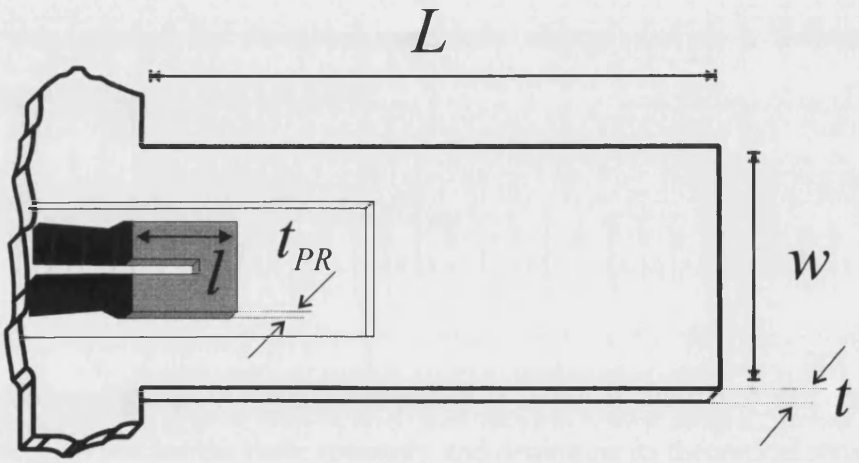

Figure 3.9 Length and thickness of piezoresistive element

The thickness of the piezoresistor is determined by the MBE grown epilayer, and is denoted t_{PR} in Figure 3.9. We can find the average stress in the cross-section of the piezoresistor by integrating over the thickness of the piezoresistor

$$\langle \sigma \rangle_{thickness} = \frac{1}{t_{PR}} \int_{\frac{t}{2}-t_{PR}}^{\frac{t}{2}} \frac{12F(L-x)y}{wt^3} dy \tag{3.9}$$

$$\langle\sigma\rangle_{thickness} = \frac{6F(L-x)(t-t_{PR})}{wt^3} \tag{3.10}$$

Likewise we can integrate over the length of the piezoresistor, giving the total average stress

$$\langle\sigma\rangle = \frac{1}{l}\int_0^l \frac{6F(L-x)(t-t_{PR})}{wt^3}dx \tag{3.11}$$

$$\langle\sigma\rangle = \frac{6F(L-l/2)(t-t_{PR})}{wt^3} \tag{3.12}$$

We now have an expression for the average stress in the piezoresistive sensor; with this we can express the fractional resistance change due to a deflection Δz. combining eqn. 3.3, 3.7 and 3.9, gives

$$\frac{\Delta R}{R} = \frac{3\pi_L Et(1-l/(2L))(1-t_{PR}/t)}{2L^2}\Delta z \tag{3.13}$$

this is equivalent to eqn. 3.2 expressed purely in terms of cantilever properties. It is now possible to finalise the basic geometry and determine its theoretical sensitivity.

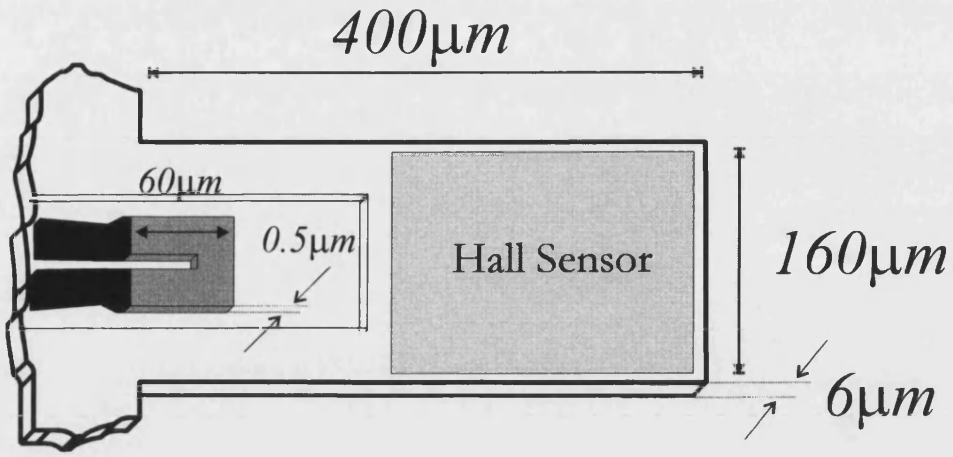

Figure 3.10 Final cantilever design with dimensions

Using the dimensions given in Figure 3.10 and the piezoresistive coefficient for $Al_{0.4}Ga_{0.6}As$, a sensitivity $\Delta R/R\Delta z = 8 \times 10^{-6}$ nm^{-1} is estimated.

3.2.6 Summary of Cantilever design

The main cantilever dimensions and properties are summarised in Table 3.1. These values represent those used to design the most recent cantilever.

Cantilever property	*Value*
Length L (μm)	400
Width w (μm)	160
Thickness t (μm)	6
Piezoresistor length l (μm)	60
Piezoresistor thickness t_{PR} (μm)	0.5
Mass ($L \times w \times t \times \rho^*$) (Kg)	1.8×10^{-9}
Spring Constant (N/m)	16.2
Resonant frequency (kHz)	30.1
Sensitivity ($\Delta R/R\Delta z$)	8×10^{-6} nm^{-1}

Table 3.1 Cantilever design specifications

* *Density of $Al_{0.4}Ga_{0.6}As$=4720 Kg/m^3 (calculated from Table 2.2)*

3.3 Hall probe design

The Hall probe design determines the maximum spatial resolution available with the magnetic sensor. The sole use of optical lithography in the project limited the minimum Hall probe width to ~1μm and the maximum achievable resolution to, in practice, slightly less than this (~0.8μm). The use of e-beam lithography (EBL) enables much higher resolutions to be achieved, and widths of 0.2-0.3μm have already been demonstrated in 2DEG $Al_{0.33}Ga_{0.67}As$ systems[10]. EBL was not used, however, as the physical width of the Hall probe is not the only factor in determining the spatial resolution as Figure 3.11 shows.

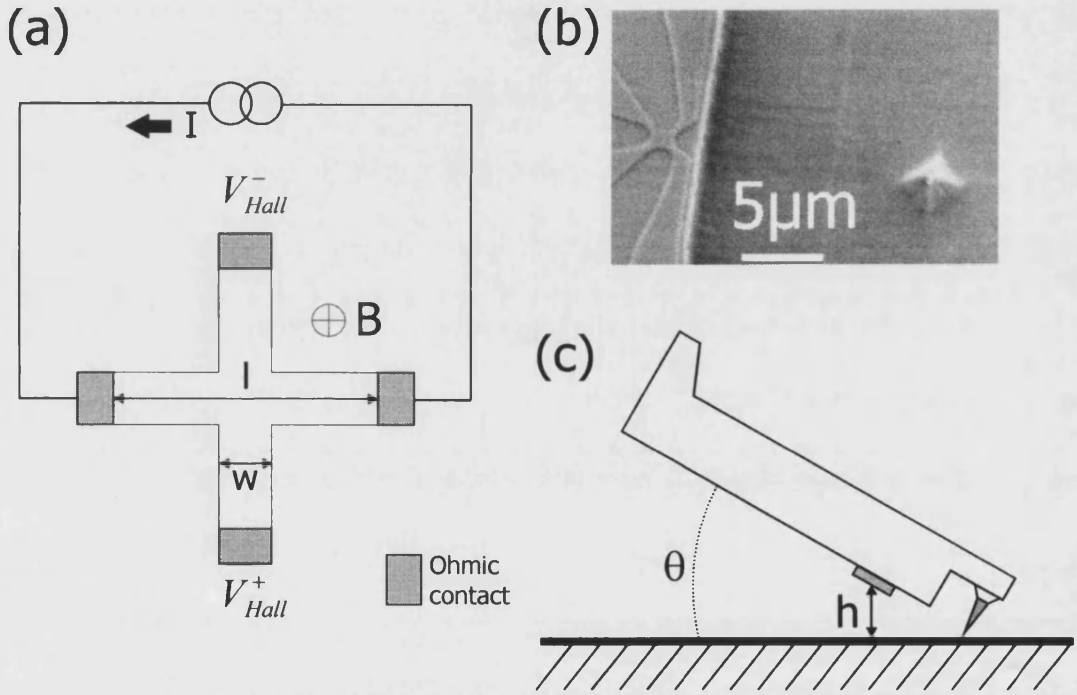

Figure 3.11 Three important factors in Hall probe design. (a) The physical size of the Hall probe. The width, *w*, determines the maximum spatial resolution. (b) Geometrical factors associated with tip to Hall probe distance and (c) sensor angle of elevation limit achievable resolution in practice. SEM (b) shows a fabricated 1μm Hall probe and a pyramidal tip ~15μm which are apart

Whilst the physical width, *w*, of the Hall probe does set the maximum achievable resolution, in practice the resolution is also dependent upon the height of the Hall

probe above the sample, *h*. For a 1μm Hall probe, the probe height can be a maximum of ~1μm for 1μm resolution imaging to be realised. The height of the probe is set by three factors, (i) the depth of the 2DEG which is set by the growth details (~100nm), (ii) the distance from the Hall probe to the tip and (iii) the angle the probe is inclined at with respect to the sample. In STM-SHPM this angle is ~1-2° while for a typical AFM measurement an angle of 11° is often used.

Clearly the tip to sensor separation should be as small as possible. For STM-tracking SHPM this distance can be as small as 5μm between the Hall probe and STM tip. For an AFM based SHPM the distance is limited to ~10-20μm because of the need to fabricate a sharp tip. This combined with a larger angle of elevation (3-4°) for AFM imaging, currently limits the resolution to ≥1μm.

The use of the 2DEG in fabricating the Hall probe provides many advantages, especially at low temperatures. The carriers in a GaAs/AlGaAs 2DEG are trapped in a triangular potential well roughly 100nm beneath the surface, ensuring that the spatial resolution is not limited by the depth of the carriers. The use of the 2DEG also slightly alters the expression describing the relationship between the Hall voltage and current (eqn. 1.3) as it is no longer dependent upon thickness, giving

$$V_H = -\frac{BI}{n_{2D}q} \tag{3.14}$$

where n_{2D} is the two dimensional charge carrier density. The use of the 2DEG at low temperatures greatly increases the carrier mobility, reducing the series resistance of the Hall probe leads by roughly an order of magnitude between room temperature and 77K. This is advantageous as it reduces the noise limited MDF, which will be discussed in Chapter 5.

3.4 Integrated Heterostructure Design

The design of the GaAs/$Al_xGa_{1-x}As$ heterostructure is of vital importance if the sensor is to be able to measure the local magnetic induction and topography simultaneously. As outlined in Chapter 2, the use of MBE techniques allows the growth of doped and alloyed epilayers with sharp interfaces. This allows the growth of heterostructures such as that shown in Figure 3.12

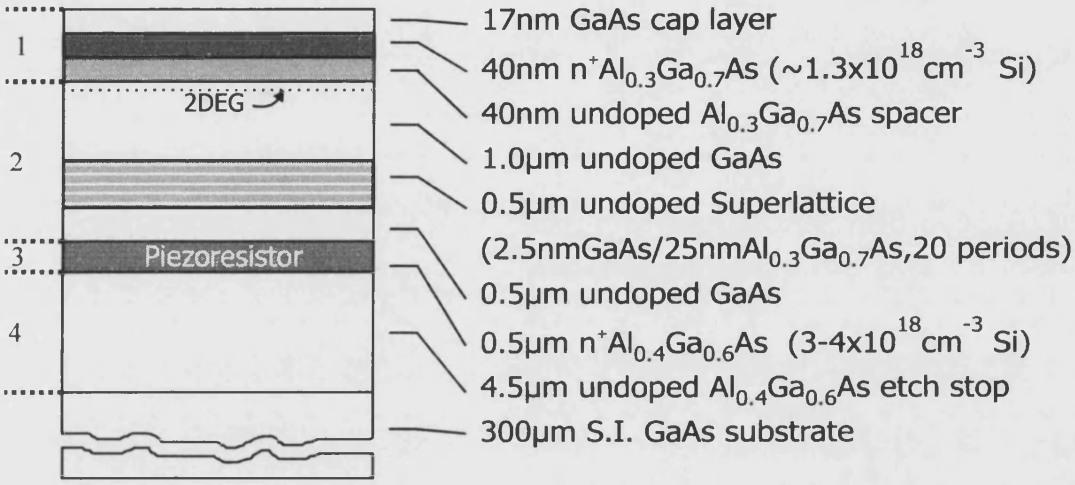

Figure 3.12 A cross-section of the integrated sensor heterostructure. The four main sections are 1) a modulation doped n-AlGaAs/GaAs interface forming a 2DEG. 2) An electrically insulating region. 3) The piezoresistive epilayer. 4) The cantilever bulk and etch stop layer.

The heterostructure design for our integrated sensor (Figure 3.12) can be grouped into 4 main sections. The first section is the modulation-doped structure as in section 2.3.3; this forms a 2DEG at the interface between the undoped $Al_{0.3}Ga_{0.7}As$ and undoped GaAs epilayers, approximately 100nm beneath the surface. The second section is made up of a 0.5μm GaAs/AlAs superlattice sandwiched between two undoped GaAs epilayers and is used as a 'buffer' region to electrically isolate the 2DEG structure from the third structure, the piezoresistive layer, situated beneath it. The piezoresistive layer is a highly doped epilayer of $Al_xGa_{1-x}As$ with an aluminium fraction, x, designed to maximise the piezoresistive response of the material. The fourth and final section is the bulk GaAs/AlGaAs slab forming the mechanical cantilever and an etch stop layer. This section forms the bulk of the cantilever

material and will determine its mechanical properties as previously described. It also serves as an etch stop when defining the cantilever during fabrication and therefore needs to contain an $Al_xGa_{1-x}As$ alloy layer to allow selective etching of the semi-insulating GaAs substrate.

3.4.1 Growth and modifications

Several wafers were grown during the course of the project by various groups to roughly similar designs. Three groups were used for growth of the MBE wafers. M. Henini at the University of Nottingham, A. J. Springthorpe at Nortel Networks, Canada and D. Ritchie and H. Beere, at the Cavendish Laboratory, Cambridge

Wafer ID	*Grower*	*Use*
MBE2239	Nortel Networks	Piezoresistive cantilever, early prototype
NU2157	Nottingham University	Integrated piezoresistive sensor fabrication
NU2187	Nottingham University	Integrated piezoresistive sensor fabrication
NU2188	Nottingham University	Integrated 2DEG sensor fabrication
CUA2525	Cambridge University	Integrated piezoresistive sensor fabrication
MBE3077	Nortel Networks	Integrated piezoresistive sensor fabrication
CUA2730	Cambridge University	Integrated 2DEG sensor fabrication
CUA2779	Cambridge University	Integrated 2DEG sensor fabrication

Table 3.2 Wafers used during the project

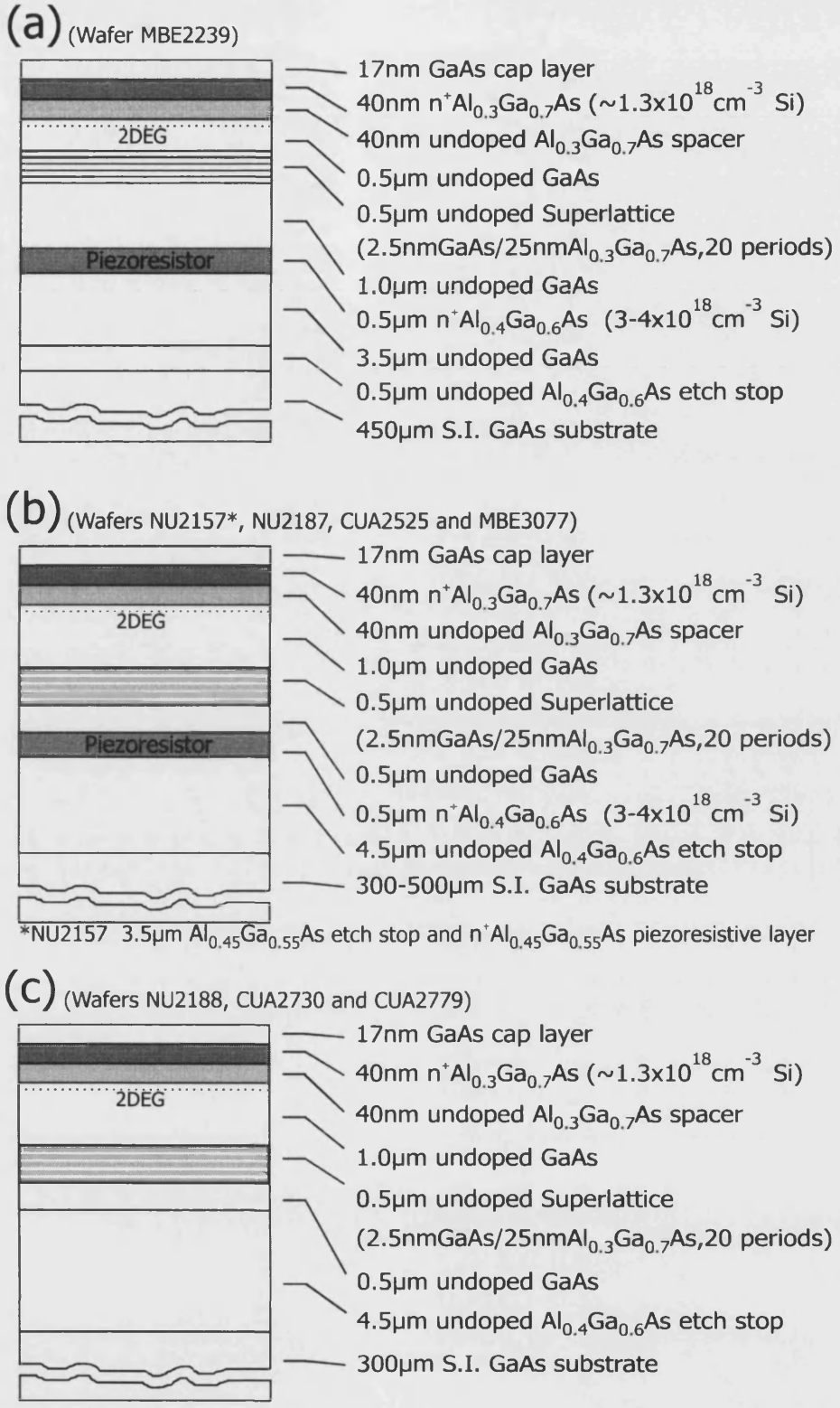

Figure 3.13 The three main heterostructure designs used during the project. The original design (a) was altered in order to solve several problems, which led to design (b). Design (c) was used to fabricate both magnetic and deflection sensors from the 2DEG, removing the need for a piezoresistive layer.

3.4.1.1 Section 1 : The 2DEG

The layer sequence and growth conditions for this structure were already well known from its use in fabricating Hall probes for STM-SHPM sensors. The structure was practically identical for all wafers in Figure 3.13.

3.4.1.2 Section 2 : Electrical isolation or 'buffer' region

The growth of this layer is critical to the sensor performance, as it stops electrical conduction vertically between the 2DEG and the highly doped piezoresistive epilayer. The thickness of this layer and the use of the superlattice are designed to act as a barrier to stop vertical conduction. A major factor that influences the conductivity of this region is the growth temperature of the superlattice, with low growth temperatures used to increase the resistivity[11]. An additional benefit of incorporation of the superlattice is that it should trap dislocations and background impurities and prevent them from reaching the sensitive 2DEG.

The original design[12] in Figure 3.13(a) was altered to accommodate a change in the fabrication procedure, whereby the two GaAs layers were swapped either side of the superlattice. The superlattice was also slightly altered in an attempt to reduce the vertical conductivity, giving the design in Figure 3.13(b).

3.4.1.3 Section 3 : Piezoresistive layer

The piezoresistive layer is the material from which the piezoresistive sensor is fabricated. The piezoresistive response of this material should therefore be as large as possible. In chapter 2 it was explained that this is determined by the aluminium fraction in $Al_xGa_{1-x}As$ and a value of 40% Al was chosen (NU2157 is the only wafer that slightly differed with an Al fraction of 45%). Choosing such a high Al fraction has several consequences, an increased surface roughness and a reduction in active

carriers due to DX centres. This reduction in carriers is graphically represented in Figure 3.14. At an Al fraction of 0.4, only ~1% of the donors are actually active.

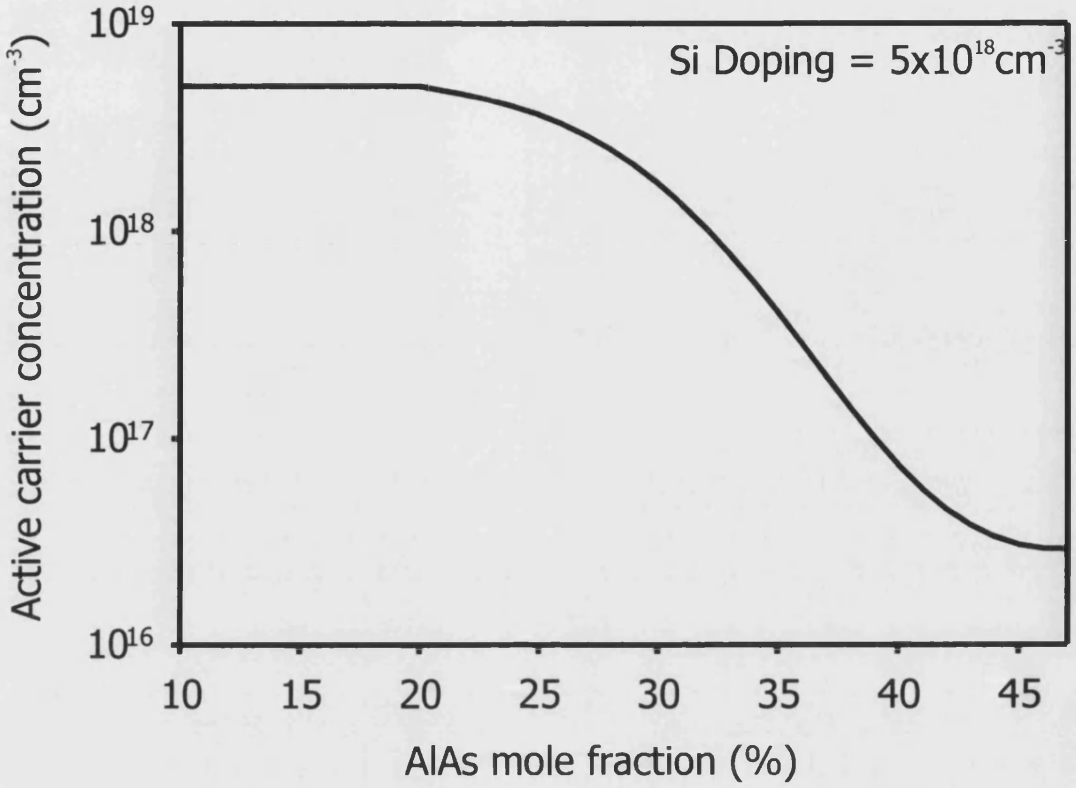

Figure 3.14 The number of active carriers in n-$Al_xGa_{1-x}As$ as a function of AlAs mole fraction for a set Si doping level[13]

The structure shown in Figure 3.13(c) has been designed without a piezoresistive layer; the 2DEG layer is used instead for the fabrication of the piezoresistive sensor as explained in 3.4.2.

3.4.1.4 Section 4 : Cantilever material and etch stop

This layer is used for two purposes; it is the main constituent of the cantilever material giving the cantilever its mechanical properties. It also serves as an etch stop when the cantilever is released from the substrate during the backside etch. The cantilever is released using a wet chemical etch which is selective for $Al_xGa_{1-x}As$ over GaAs, with a greater selectivity for a higher Al fraction.

The original design, Figure 3.13(a), used a 0.5μm $Al_{0.4}Ga_{0.6}As$ epilayer as an etch stop and a 3.5μm GaAs epilayer as the cantilever material. However, it was found that the use of the GaAs underneath the piezoresistive epilayer created a 2DEG at the interface between the two[12] which had the undesirable effect of shunting current away from the piezoresistor. To overcome this, the cantilever was fabricated entirely from $Al_{0.4}Ga_{0.6}As$.

3.4.2 2DEG Piezoresistor and Hall probe

During the early stages of the project it was realised that fabrication of the dual sensor cantilever was far from straightforward, many factors such as the quality of the heterostructure growth and the limitations of GaAs fabrication techniques made fabrication complex. To try and reduce the complexity and increase working sensor yield, a slightly different heterostructure was devised, whereby the 2DEG would be used to fabricate both the Hall probe and piezoresistive sensor (Figure 3.13(c)).

The use of $GaAs/Al_xGa_{1-x}As$ 2DEG systems for piezoresistive detection has not been well documented, but Dana *et. al.* have shown that parametric amplification is possible using a curved 2DEG piezoresistive cantilever[14], thus demonstrating its suitability for AFM detection.

Using the 2DEG to fabricate sensors, the complexity and the time taken to fabricate a complete working cantilever is reduced drastically. It also removes the possibility of parallel conduction between the piezoresistive epilayer and 2DEG. The superlattice and the other epilayers were left in the heterostructure to reduce dislocation and background impurity densities.

The disadvantages of using the 2DEG for the piezoresistor are that it is highly dependent upon temperature and illumination, although these problems can be minimised by the use of a temperature-controlled cryostat. The piezoresistive

response of the 2DEG was also unknown at low temperatures, although it was hoped it would increase at low temperatures.

3.5 References

[1] M. Tortonese, H Yamada, R. C. Barrett and C. F. Quate, *in Proceedings of transducers '91* (IEEE) 448, (1991)

[2] M. Tortonese, R. C. Barrett and C. F. Quate, *App. Phys. Lett.*, **62**, 834 (1992)

[3] G. Binnig, C. F. Quate, Ch. Gerber, *Physical Review Letters* **56**, 930 (1986)

[4] Y. Su, A. Brunnschweiler, A. G. R. Evans, G. Ensell, *Sensors and Actuators* **76**, 139 (1999)

[5] J. E. Sader, *Rev. Sci. Instr.*, **74**, 2438 (2003)

[6] M. Willemin, C. Rossel, J. Brugger, M. H. Despont, H. Rothuizen, P. Vettiger, J. Hofer, H. Keller, *J. App. Phys.*, **83**, 1163 (1998)

[7] R. Muncaster, *Physics*, Stanley Thornes (1992)

[8] J. A. Harley, *Advances in Piezoresistive Probes for AFM*, PhD. Thesis, Stanford University (2000)

[9] D. Sarid, *Scanning force microscopy*, OUP, (1991)

[10] A. Oral, J. C. Barnard, S. J. Bending, I. I. Kaya, S. Ooi, T. Tamegai, an M. Henini, *Phys. Rev. Lett.* , **80**, 3610, (1998)

[11] From discussions with A. J. Springthorpe, Nortel Networks, Canada

[12] J. Pinto, *Microfabrication of a GaAs/AlGaAs AFM cantilever with piezoresistive detection*, M. Phil thesis, University of Bath, (2000)

[13] Empirical data provided by A. J. Springthorpe, Nortel Networks, Canada

[14] A. Dana, F. Ho, Y. Yamamoto, *App. Phys. Lett.*, **72**, 1152 (1998)

Chapter 4

4 Sensor Fabrication

4.1 Introduction

This chapter will discuss the steps taken to fabricate the integrated cantilever sensor. Firstly, the wafer preparation will be discussed, then the fabrication steps and finally the mounting of the cantilever for experimental use. The fabrication of the more conventional sensor with an embedded piezoresistive layer differs from that of the sensor with a 2DEG piezoresistor, and these differences will be presented at the end of the main fabrication section. The sensor fabrication was undertaken in the clean room facilities at the University of Bath.

4.2 Wafer preparation

The GaAs/$Al_xGa_{1-x}As$ wafers used during the project were all (100) wafers. Therefore the most important planes for device fabrication are the {011} planes as these are the natural cleaving planes for a (100) wafer. The wafers, which are usually 3" or 4" in diameter, are cleaved into smaller pieces at the start of the fabrication process to make the handling of the samples easier.

The orientation of the {011} planes determine the shape of the etched facet wall, giving either, a slightly forward sloping facet as shown in Figure 4.1(a) for an (011) plane or a backward sloping facet for a $(01\bar{1})$ plane (Figure 4.1(b)). This property of GaAs needs careful consideration, especially when very deep etches are to be performed, as the forward sloped facet is more pronounced with increased etch rate[1]. The cantilevers can be fabricated along either of the {011} planes as the mechanical properties and piezoresistive properties should be equivalent.

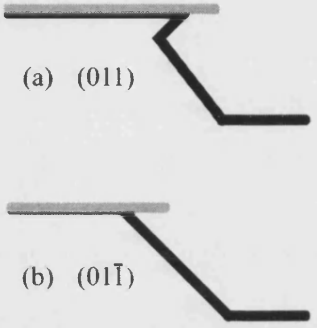

Figure 4.1 Etch profiles for the (011) and $(01\bar{1})$ cross sections

The wafers were scribed asymmetrically into 4.5mm x 5mm rectangular segments; with the short edge determining which of the {011} planes the cantilever is to be orientated along. Usually this was performed along the [011] direction.

Some of the wafers used during the project had a covering of indium on the backside of the wafer, a consequence of being mounted in certain MBE chambers where it was required for better temperature control. The indium was removed by lapping the backside of the sample with a fine (1200 grade) abrasive paper.

4.3 Fabrication Techniques

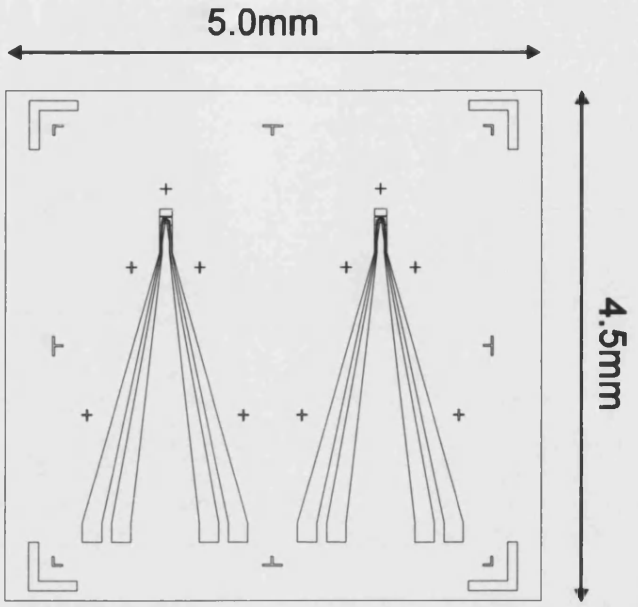

Figure 4.2 Schematic of two cantilevers patterned on one sample

As can be seen in Figure 4.2 each chip sample is used to fabricate 2 cantilevers. By fabricating in small batches device yield is increased, although this is at the expense of increasing the fabrication time. Usually 8-12 samples were processed at a time yielding 24 sensors if all were successful.

4.3.1 Cleaning procedure

The cleanliness of the chip surface is of paramount importance when trying to fabricate devices in a clean room environment. At each stage of the fabrication process the chip sample is kept as clean as is possible by using a combination of solvents, de-ionized water and filtered nitrogen gas (for drying the samples). To further ensure cleanliness, the samples are kept in a covered glass Petri dish during the entire fabrication procedure.

The main cleaning routine involves the use of three different solvents. The solvents and samples are placed in glass beakers then positioned in an ultrasonic bath for 5 minutes at a low power setting to prevent damage to the samples. The first solvent is a chlorinated solvent, trichloroethane, and is used to degrease the samples. This is followed by cleansing in acetone and isopropanol. After this the samples are dried under a stream of N_2 gas.

Following the developing and etching stages, the cleaning procedure involved the use of de-ionized water to thoroughly remove any active substances, which was then followed by the same three-stage solvent cleaning procedure.

Once clean the samples are mounted on glass microscope slides using photo-resist and baked at 90°C for adhesion. This is done to aid the handling of the small samples and prevent damage.

4.3.2 Photolithography

Photolithography is the process whereby a photosensitive material is exposed to a light source through a pre-defined mask to imprint the design onto the photosensitive material. In standard photolithography the material is usually an organic polymer, called photo-resist, which is sensitive to ultra-violet (UV) radiation. This process can be performed with either a positive or a negative resist; a positive resist is soluble in a developing agent when exposed to UV and a negative resist insoluble when exposed to UV light. A positive resist is most commonly used as it is easily removed with acetone once the subsequent fabrication step has been performed, whereas the negative resist is far harder to remove once exposed.

Figure 4.3 illustrates the photolithographic process. The samples are coated with an even layer of photoresist using a resist spinner. This device uses an electric motor to rotate a chuck at rotational speeds controlled by a separate digital regulator. The thickness of the resist film is dependent upon the rotational speed, the resist

viscosity and spin time. The samples are usually spun at a speed of 5000rpm for 30 seconds to achieve a resist thickness of ~1.5μm. The coated samples are then baked at 90°C, in an oven or on a hotplate, to remove any solvents from the resist and harden the film.

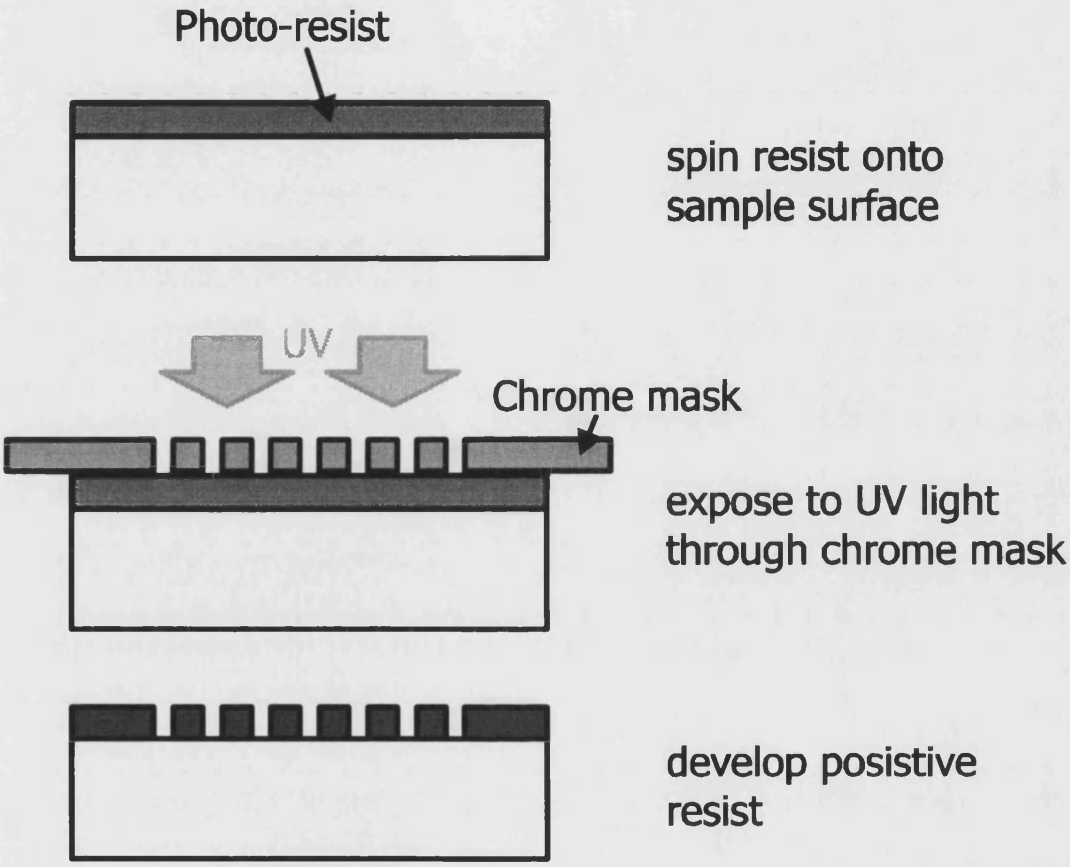

Figure 4.3 Schematic illustration of the photolithography process for a positive resist

The procedure described above is mainly used when an etch is to be performed on the sample. When metal is to deposited onto the sample surface the procedure is slightly different and termed 'lift-off'.

The controlled deposition of metals is achieved by using the resist as a sacrificial surface that is removed leaving only the metallised areas which were not originally covered with resist. For this process the samples are spun at a speed of 4000 rpm for 30 seconds, to produce a thicker resist. This process is illustrated in Figure 4.4.

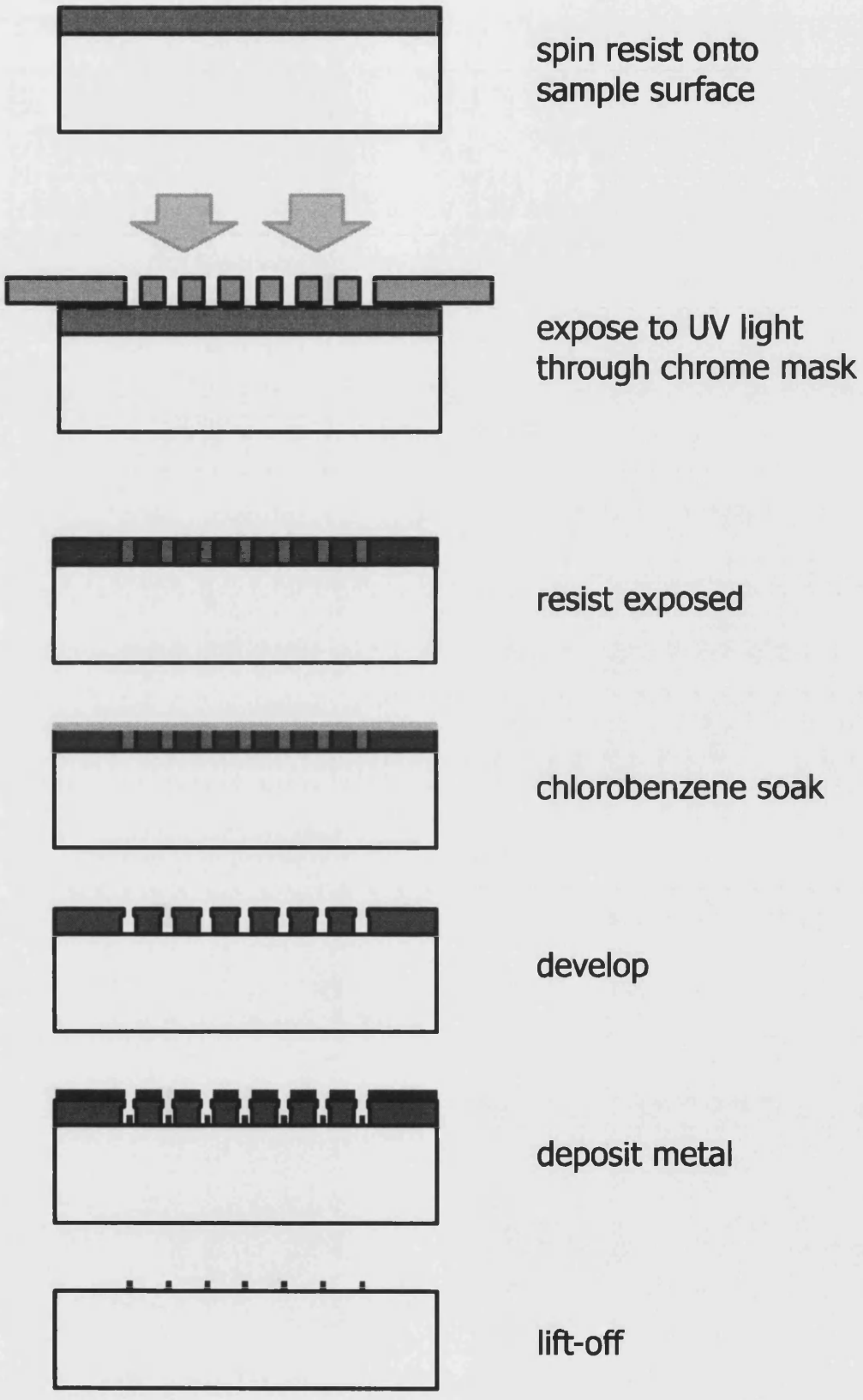

Figure 4.4 Lift-off process

The process is similar to the normal photolithographic process except that after the photo-resist is exposed, the sample is then soaked in chlorobenzene. The chlorobenzene alters the surface of the photo-resist by removing the lower molecular weight resin and thereby reducing the dissolution rate when developed[2]. The effect of this is to produce a developed resist with an overhang profile as shown in Figure 4.4 which ensures sharp edge profiles after metal deposition.

4.3.3 Etching

Wet etching was exclusively used in the fabrication of the cantilevers. This was accomplished by placing the sample in a beaker of etchant, which was agitated using a magnetic stirrer. The etching solutions used for the fabrication of the cantilevers can be divided into three, not necessarily exclusive categories: selective, non-selective and temperature-dependent. Dummy 'test' samples were used at each stage of the fabrication process to determine the exact etch rate for each solution. The main etchants are summarised in Table 4.1

No.	Etchant	Volume Ratio	Type	Etch rate (μm/min)	Temp (°C)
1	$H_2O:H_2O_2:H_2SO_4$	1000:8:1	Non-Selective	0.038*	22
2	$H_2O:H_2O_2:H_2SO_4$	160:8:1	Non-Selective	0.26*	22
3	$H_2O:H_2O_2:H_2SO_4$	80:8:1	Non-Selective	0.54*	22
4	$H_2O:H_2O_2:H_2SO_4$	1:8:1	Non-Selective	14.6*	22
5	$H_2O:H_2O_2:H_3PO_4$	1:1:12	Non-Selective	0.5†	0
6	NH_4OH/H_2O_2	N/A‡	Selective	2 - 4§	22

Table 4.1 Summary of the wet etches used for fabrication

* D. W. Shaw, *J. Electrochem. Soc.*, 874 (1981)

† Calculated in section 4.4.7

‡ H_2O_2 plus a few drops of NH_4OH for pH of 8.4

§ Calculated in section 4.4.6

4.4 Cantilever with piezoresistive layer

The fabrication procedure for the piezoresistive cantilever is complicated and involves many steps. The cantilever steps (and design) have also been changed / revised since the original work[3] on piezoresistive GaAs cantilevers. The steps given here represent the current 'best method' used to produce the most recent cantilevers.

4.4.1 Step 1 : Sample preparation

The first step is one of the most crucial as it affects the whole fabrication procedure, the steps described in 4.2 and 4.3.1 are carried out in a rigorous manner to ensure the samples are clean and free from scratches and defects.

4.4.2 Step 2 : Hall sensor definition

The first etch step is to define the Hall sensor. Previously this step was carried out much later in the fabrication procedure, which had two pitfalls. Firstly, if the Hall sensors etch was unsuccessful, all the preceding fabrication steps would be in vain as the sensor would be rendered unusable. Secondly, the etch requires high resolution lithography (~1μm), which is far easier to achieve with a 'virgin' sample surface as this allows good edge definition to be obtained. There is however an increased risk of sensor damage during fabrication using this method, but this risk is far outweighed by the problems posed by performing the etch later in the process.

The Hall probe etch requires high resolution photo-lithography to achieve a 1μm Hall cross. For photo-lithography we use a Karl-Suss mask aligner which has a maximum resolution limit of ≥0.5μm. Achieving 1μm resolution therefore requires the resist to be as flat as possible, as this allows the mask and sample to be brought into very close proximity and thereby limit unwanted diffraction effects. The

flatness of the resist is determined by the resist spinner. When the resist is spun it forms edge beads at the boundary of the sample, and these 'beads' can be many times higher than the resist in the middle of the sample. To remove these beads a mask was devised which removed all the resist from the edges of the sample. The sample is therefore developed twice, first to remove the edge resist, and second to define the Hall probe on the flat resist remaining. This 'double' developing is carried out at all lithography stages.

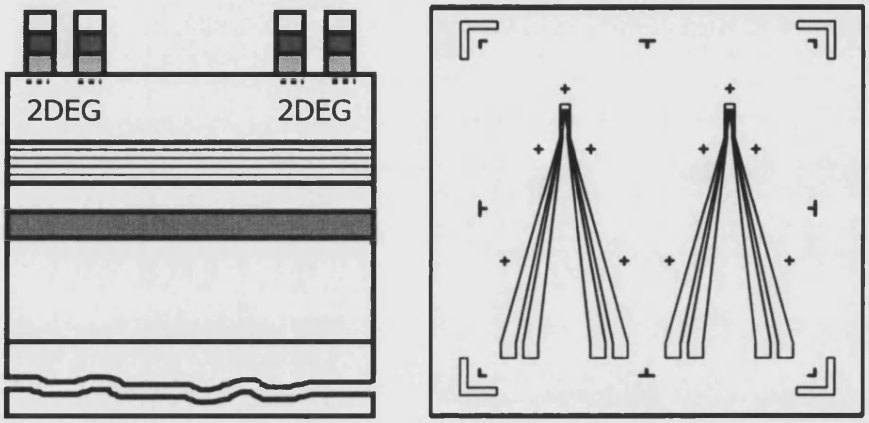

Figure 4.5 Epilayer and plan view after the first etch to define the piezoresistor. The epilayer structure is the same as Figure 3.11 (not to scale)

Once the Hall sensor is lithographically defined, it is etched using etchant 1 (Table 4.1) for ~2 minutes to a depth of 70nm. The etched sample is shown schematically in Figure 4.5. A set of typical images of etched Hall probes is shown in Figure 4.6. Once the sample is etched it is cleaned as described in 4.3.1, this cleaning procedure is performed after each step or sub-step.

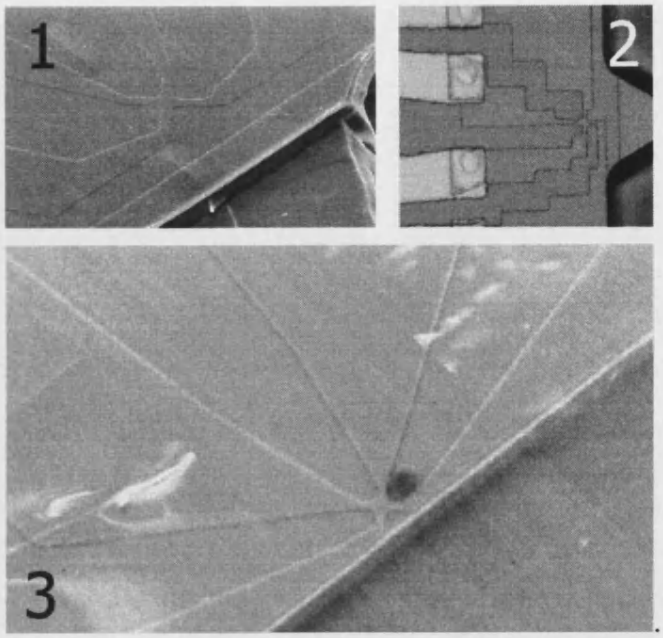

Figure 4.6 3 Different Hall probe designs used during the project. (1) 2μm wire width 1st generation Hall sensor (2) 2μm wire width 2nd generation (3) 1μm wire width 3rd generation design.

4.4.3 Step 3 : Piezoresistor definition etch

The definition of the piezoresistor is achieved using two consecutive non-selective etches. The samples are first etched for 6 – 7 minutes to a depth of ~1.8 μm using etchant 2. The lithographic mask used for this etch covers only the active region surrounding the Hall sensor (Figure 4.7(a)). This is performed to ensure the piezoresistor is at the bending-axis surface, as from eqn. 3.6 we know that the largest stress is at the surface of the cantilever at its base. The sample is etched to a depth of 1.8μm which is just above the highly doped piezoresistive layer. Approximately 100nm of undoped GaAs is left at the interface of the doped AlGaAs layer to reduce the resistivity of the piezoresistive sensor due to surface depletion (discussed further in Chapter 5).

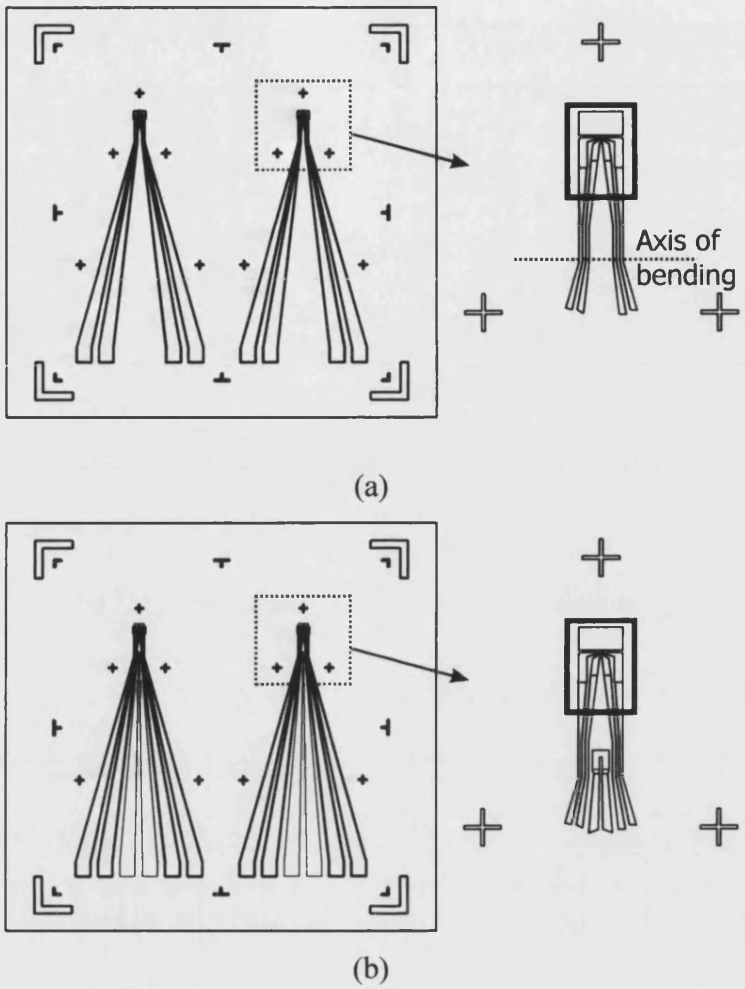

Figure 4.7 The two stage process for piezoresistor definition. (a) Define Hall sensor isolation pad, (b) piezoresistor definition

The definition of the piezoresistor is now achieved using a further non-selective etch (etchant 2) for ~3 minutes to a depth of 0.8μm, this ensures there is no electrical short between the two channels of the piezoresistor as shown in Figure 4.7(b).

4.4.4 Step 4 : Ohmic contact deposition

To electrically contact the devices ohmic contacts need to be deposited onto the surface of the samples. Ohmic contacts are deposited in three stages for the piezoresistive cantilever. The first stage is the deposition for contact to the piezoresistor itself. This contact is a simple ohmic contact using the following metal layer sequence

Metal	Thickness (nm)
Ge	27
Au	54
Ni	6
Ti	20
Au	200

Table 4.2 Metal layer sequence for ohmic contacts

The deposition of nickel after the first gold layer is to stop balling of the Ge during alloying and to enhance Ge diffusion[4]. The Ti and second Au layer are used to allow gold bond wires to be contacted directly to the ohmic pads on the sample. To deposit the metals on to the samples the photoresist is first prepared as outlined in Figure 4.4, after which they are placed in an Edwards 306 metal deposition chamber, and the metals deposited under a vacuum of ~$1x10^{-6}$ mbar. The coated samples are then placed in a bath of (warm) acetone to achieve 'lift off' of the unwanted metal. After several hours the samples can be removed from the bath and cleaned. The samples are now coated as shown in Figure 4.8. The ohmic contact to the carriers in the piezoresistive layer is achieved by annealing the samples in a forming gas (90%N_2:10%H_2) atmosphere at a temperature of 420°C for 45 seconds.

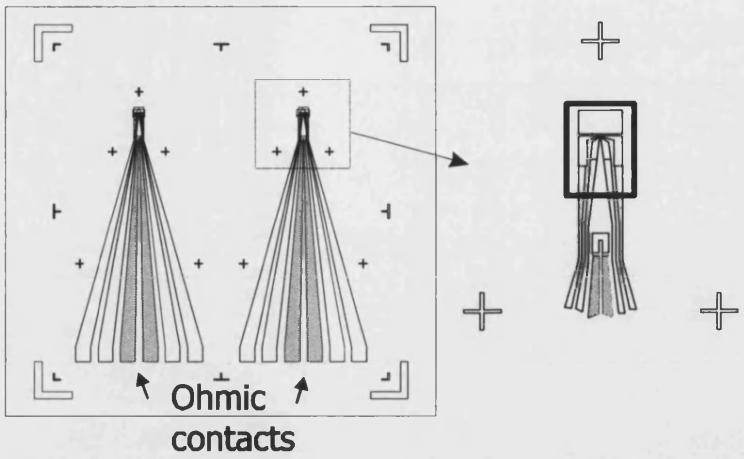

Figure 4.8 First deposition for ohmic contact to the piezoresistor

The second and third depositions are used to create a shallow ohmic contact to the 2DEG. When alloying, great care must be taken not to generate a short between the two parallel conducting systems in the 2DEG and the piezoresistor. To limit this possibility a 'shallow' ohmic contact formulation is used. The sequence of metal depositions is as follows

Metal	Thickness (nm)
Ge	66
Au	134
Ti	20
Au	200

Table 4.3 Metal layer sequence for 'shallow' ohmic contacts

The deposition is performed in two stages, the first is the deposition of the 66nm Ge and 134nm Au layers onto small pads at the base of the Hall sensor, as in Figure 4.9(a). The second stage is the deposition of 20nm of Ti and then 200nm of Au on top of the pads and the contact leads to the bonding pads (Figure 4.99(b)). The samples are then annealed in a forming gas atmosphere at 350°C for 15 seconds.

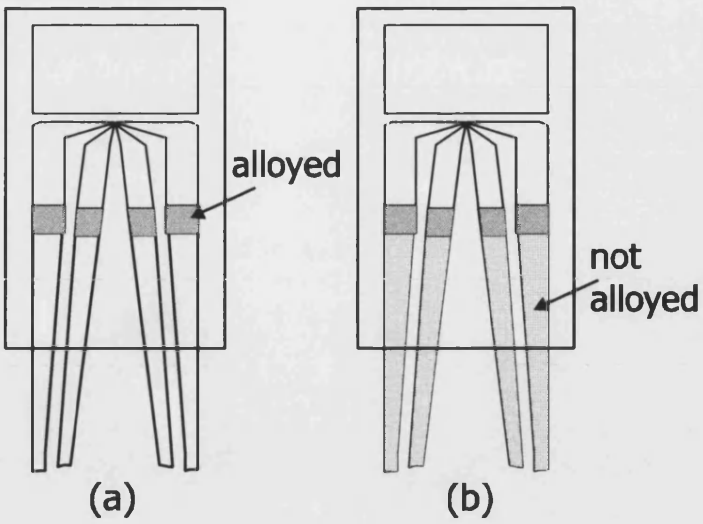

Figure 4.9 Second and third deposition to make 'shallow' ohmic contacts to the Hall sensor

An SEM of a finished cantilever is shown in Figure 4.10, clearly showing the annealed pads and the raised active region for the Hall sensor.

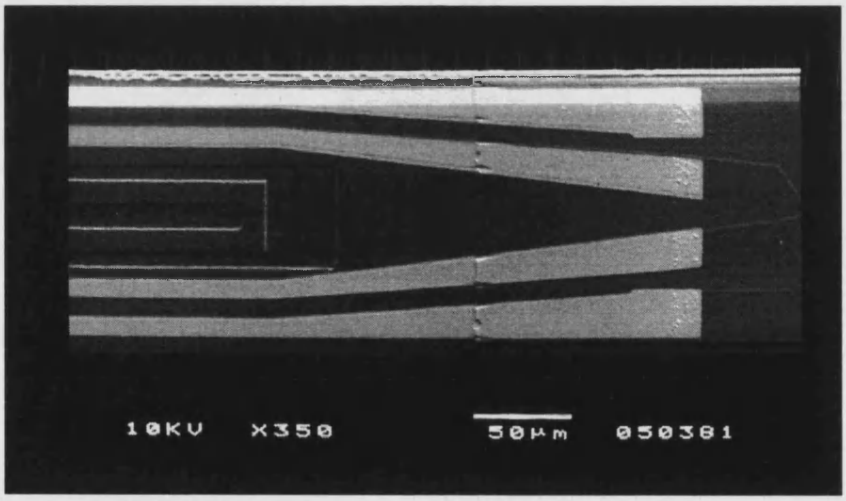

Figure 4.10 SEM of a finished cantilever clearly showing the annealed ohmic contacts

An important consideration when depositing the metallisation layers, as in Figure 4.9(b), is the orientation of the crystallographic planes to be covered. If the cantilever is orientated along the [011] direction, the metal is deposited onto a facet with a profile similar to Figure 4.1(a), which can cause the contact between the

lower and upper levels to be broken. It is easier to deposit contacts onto facets as in Figure 4.1(b), with the cantilever oriented along the $[01\bar{1}]$ direction. A side view of the cantilever is shown in Figure 4.11.

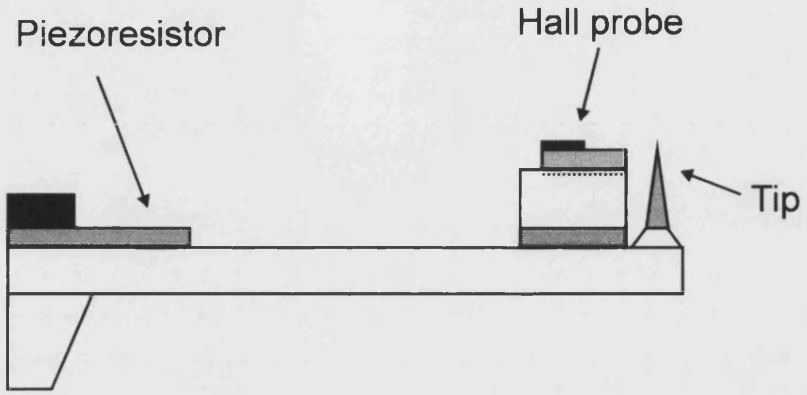

Figure 4.11 Side view of the cantilever, showing the raised mesa with fabricated Hall sensor on top (not to scale)

4.4.5 Step 5 : Cantilever definition etch

This step is used to define the cantilever shape i.e. its width and length. The sample is etched using a non-selective solution (etchant 3) for duration of ~8 minutes to a depth of 4μm. This should result in an etch to approximately the bottom of the 4.5μm AlGaAs etch stop layer. Figure 4.12 shows a cantilever after the cantilever definition etch, fabricated to a slightly different (older) design.

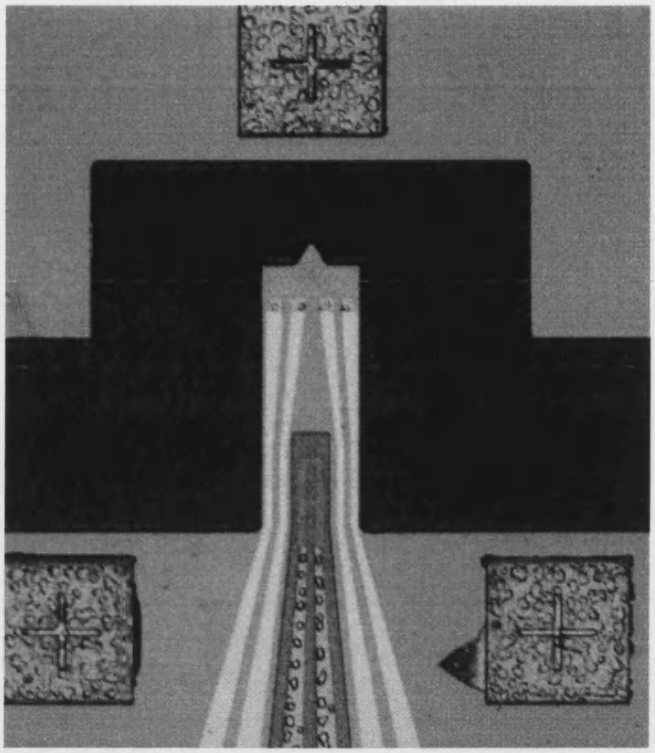

Figure 4.12 Optical micrograph of cantilever after the cantilever definition etch (old design)

4.4.6 Step 6 : AFM tip etch

This step is used to define a sharp tip at the very end of the cantilever. The method we used was first presented by Yamaguchi *et. al.*[5] in which they fabricated pyramidal tips with diameters of ~50nm. The method they employed was to use a H_3PO_4-based etchant and a 10x10μm square etch mask orientated in a direction at 45° to the normal {011} planes, i.e. the [010] direction. They found that the tip shape and quality was also highly dependent upon the etchant temperature and they further showed that a temperature of 0°C produced a sharp tip with a high aspect ratio.

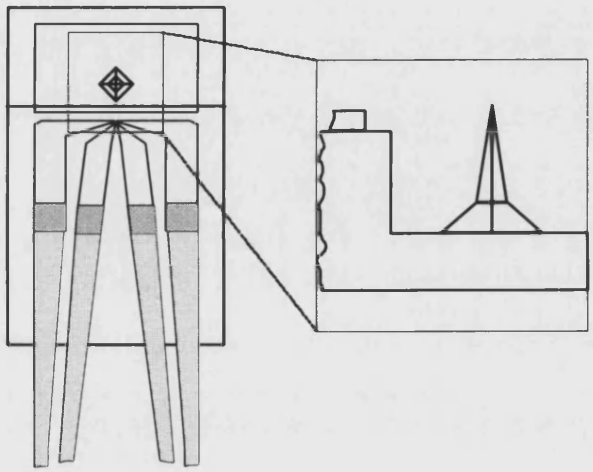

Figure 4.13 Tip etch, plan and side views of the multi-faceted tip produce using the etchant proposed by Yamaguchi *et. al.*

A sketch of the desired high aspect ratio tip can be seen in Figure 4.13. The lower portion of the tip is composed of shallow {110} facets, and the long sharp upper portion of the tip is made up of steep {150} facets. This is illustrated in Figure 4.14. A high aspect ratio tip is advantageous in AFM as it allows one to map deep fine features.

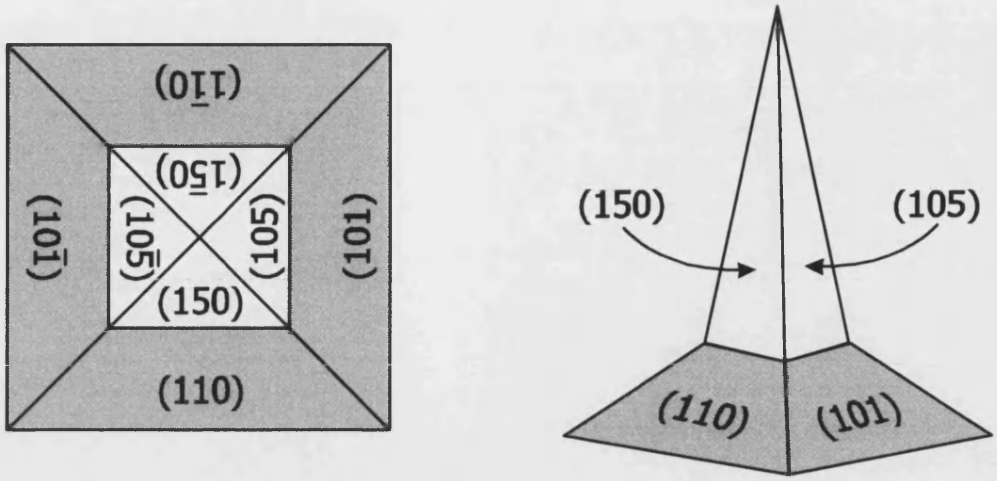

Figure 4.14 Illustration of the facets exposed during the H_3PO_4 etch

The method proposed by Yamaguchi *et. al.* is however not directly suitable for our cantilever as they fabricated their tips from a GaAs substrate which had been etched to a depth of many micrometers (>20μm). As our cantilevers have a maximum depth of ~7μm a slight revision of the method is required. The first parameter that needed to be determined with some precision was the etch rate of the H_3PO_4-based etch solution, which was previously unpublished. All etches were performed at 0°C, as Yamaguchi *et. al.* had shown that the best tip shapes are produced at this temperature. The etch solution used was based on the volume ratios quoted in a more recent publication using the same etchant[6]. The etchant used was a H_2O:H_2O_2:H_3PO_4 solution in a 1:1:12 volume ratio.

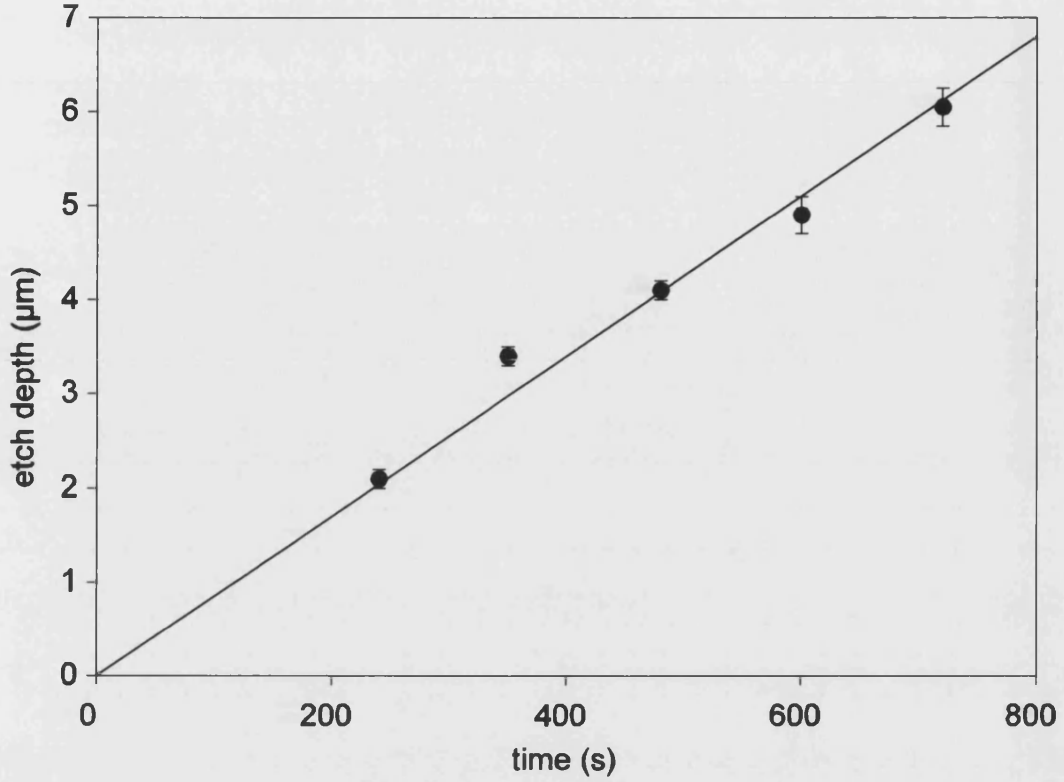

Figure 4.15 Graph showing etch depth as a function of time for an $H_2O:H_2O_2:H_3PO_4$ solution in a 1:1:12 volume ratio at 0°C

Figure 4.15 shows several test etches for etchant 5 at 0°C for varying lengths of time. The etch rate was found to be approximately 0.5 µm/min.

The next parameter to be determined was the required size of the etch mask. To try and find the dimensions of a suitable square, masks with side lengths of 2, 5, 7.5 and 10µm were designed and tested.

The 2x2µm square mask was found to be too small to obtain the necessary lithographic resolution, producing a circular shaped mask after developing, due to corner rounding. This mask was therefore not used for etching.

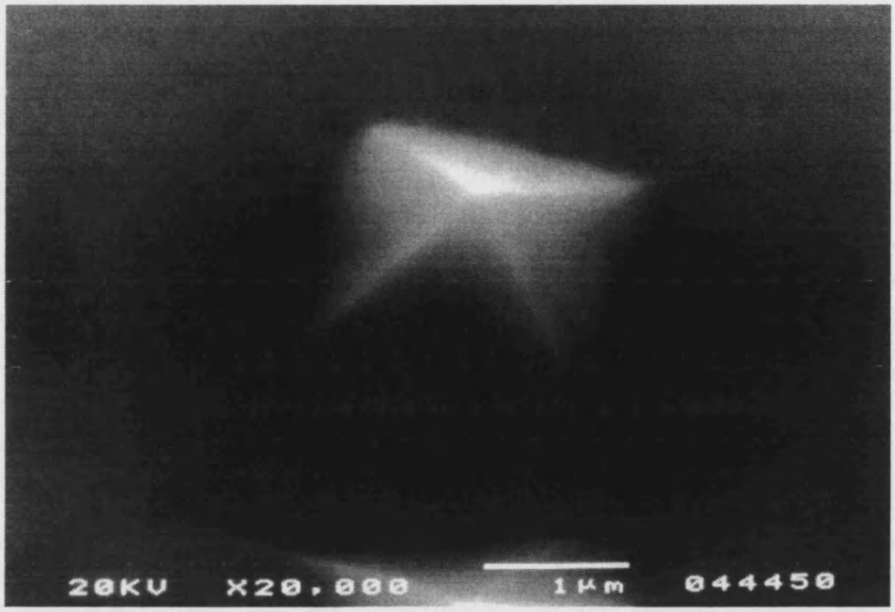

Figure 4.16 Etch using the 5x5μm square mask. After 4 minutes of etching, only the {110} facets are revealed.

The first mask to be etched was the 5x5μm mask and the resulting etch is shown in Figure 4.16. After 4 minutes of etching a pyramidal tip is formed, but this is composed of only the {110} facets, with no high aspect {150} facets present. The low aspect ratio tip, although sharp, is not suitable for AFM measurement as it would have difficulty measuring fine deep features.

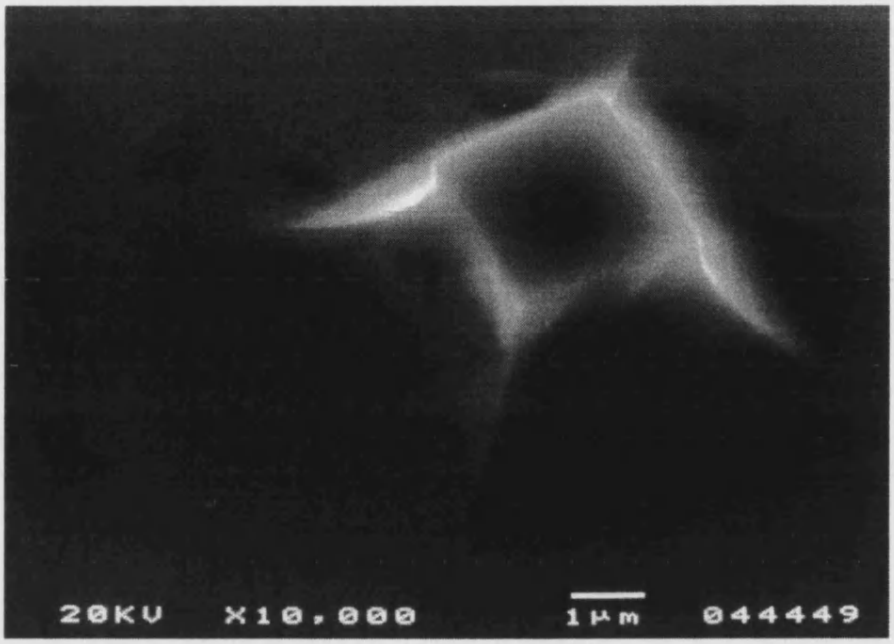

Figure 4.17 Etch using the 10x10μm square mask. After 12 minutes of etching, the {150} facets have started to form but further etching is needed for a sharp tip

The next mask to be tested was the 10x10μm square. The results are shown in Figure 4.17. It can be seen that after 12 minutes the {110} facets have been formed and the high aspect ratio facets are visible but they have not converged at the sample surface to produce a sharp tip. Further etching would be needed to produce a sharp tip, but would require an etch depth in excess of the cantilever depth and was therefore deemed unsuitable. This type of structure is similar to that used by Weaver *et. al.*[7] to pattern a Bismuth Hall sensor on the square plateau that is formed.

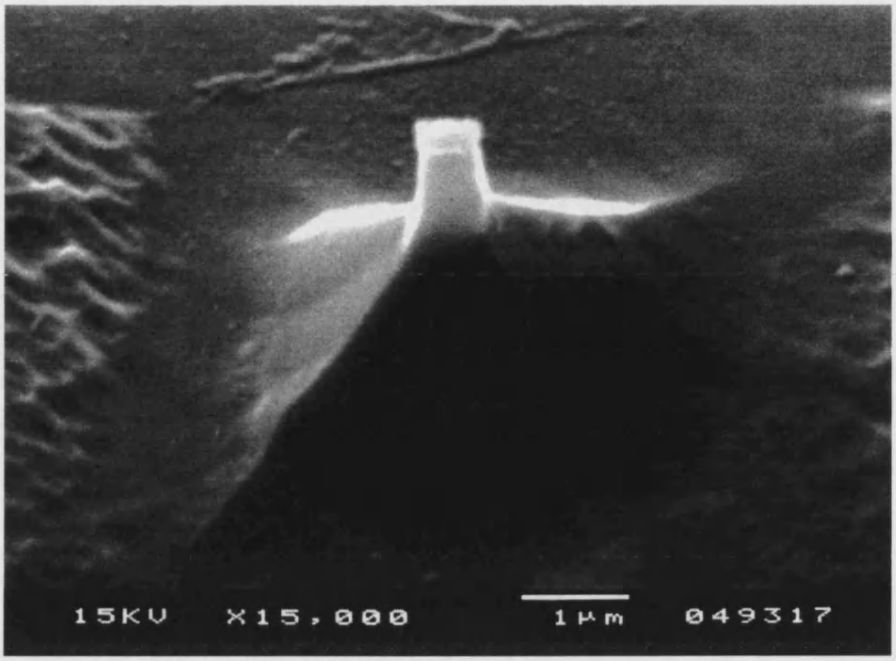

Figure 4.18 Etch using the 7.5x7.5μm square mask. After 6.5 minutes of etching (~3μm depth), both the {110} and {150} facets are clearly visible.

After the failure of the 5μm and 10μm square masks a 7.5x7.5μm square mask was designed and tested, hoping it would produce a high aspect tip within the fabrication limits. The results are shown in Figure 4.18. A reasonably sharp tip was obtained after etching for 6.5 minutes. It can be seen that the tip is not ideally sharp as a small ~0.5x0.5μm square is still present at the very tip. However, very sharp tips were produced after a further 30 - 40 seconds of etching, with tip diameters approaching the 50nm limit cited in the original Yamaguchi *et. al.* paper. During etching the size of the tip was estimated using an optical microscope, the tip was assumed sharp when a square could not be observed at the end of the tip, using a magnification of 200x. A sharp tip etched in this fashion is shown in Figure 4.19. The tip is in this case is only poorly resolved due to charge build up at the apex of the uncoated tip during SEM imaging.

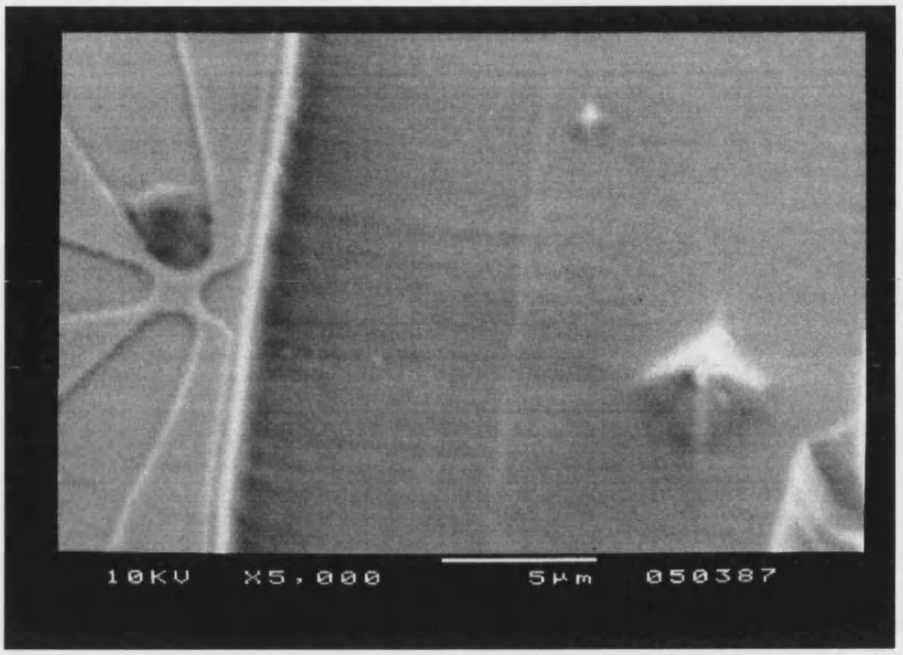

Figure 4.19 SEM picture of a 7.5x7.5µm tip

As has already been stated the temperature of this etch is critical with regard to defining the tip shape and aspect ratio. One further factor of note regarding this etchant is the lifetime of the etch solution. It was found that after 9-10 tip etches, or approximately an hour, the solution would start etching in a less predictable manner. The tip shapes would become poor and ill undefined, often resulting in a cantilever with no tip. The cause of this change in solution behaviour was undetermined but may arise from contamination of the etchant. To overcome this, the solution was replaced after every 5 or 6 etches.

4.4.7 Step 7 : Backside etch

The final step in the fabrication process is to release the cantilever from the substrate. This can also be the most problematic step in the whole fabrication procedure. This step requires the use of a selective etch to remove the substrate from the back of the AlGaAs cantilever. The substrate can be as thick as 500µm and the fastest selective etch (GaAs over $Al_xGa_{1-x}As$) known to the author has an etch rate of

~5μm/min[8] for x = 0.45. The etchant (6) is a mixture of hydrogen peroxide (H_2O_2) and ammonium hydroxide (NH_4OH) and the etch rate is strongly dependent on the solution pH. Ammonium hydroxide is added drop wise to the hydrogen peroxide until the desired pH is achieved. At a pH of 7.3 and 0°C the solution has a selectivity of ~30 and an etch rate of ~0.2μm/min for x = 0.8[8]. As the pH is increased the etch rate also increases but selectivity diminishes. At pH 8.4 the etch rate is ~5μm/min but the selectivity is ~10 for x = 0.8. The selectivity is also reduced for smaller Al fractions, the selectivity for x = 0.4 will be less than 10 for a pH of 8.4. The etch rates quoted above are for jet chemical polishing machine at 0°C, and will differ slightly to the rotating solution sample assembly at room temperature, which was used for all release etches in this project. Other selective etches for GaAs over $Al_xGa_{1-x}As$ have been reported, many using a citric acid based solutions giving very high selectivity's[9] (260 for x = 0.45) but with low etch rates, (a maximum of ~1μm/min[10]) making them unsuitable for our purpose.

Previous studies[3] have shown that at 25°C the etch rate of etchant 6 was ~5μm/min with a selectivity of 230 at pH = 8.40 in a rotating solution sample assembly. In several attempts to reproduce this etch rate the maximum recorded was 3.5μm/min. At this pH the surface became highly contaminated by the oxide and other by-products of the chemical reaction, further reducing the etch rate over time. These contaminants were removed by placing the sample in a $HCl:H_2O$ (1:1 volume) bath for 45 seconds. At this etch rate the 500μm substrate would take 142 minutes to remove. One problem that was encountered with long exposure to the etch solution was that at such a high pH the solution starts to dissolve the photo-resist, requiring the resist to be re-applied every 60 minutes.

To solve many of these problems it was decided that the back etch be performed in two stages. The first would be a fast non-selective etch to a depth 60-80nm from the cantilever surface and the second would be a selective etch to the AlGaAs etch stop layer. This procedure is illustrated in Figure 4.20. Note that the crystallographic orientation of the cantilever needs to be known at this point, as this determines the

border of the initial etch mask on the backside of the sample. At this stage the sample was also cleaved into two halves, resulting in double the number of samples with one cantilever per sample. This ensured that if an etch went wrong only one cantilever would be lost.

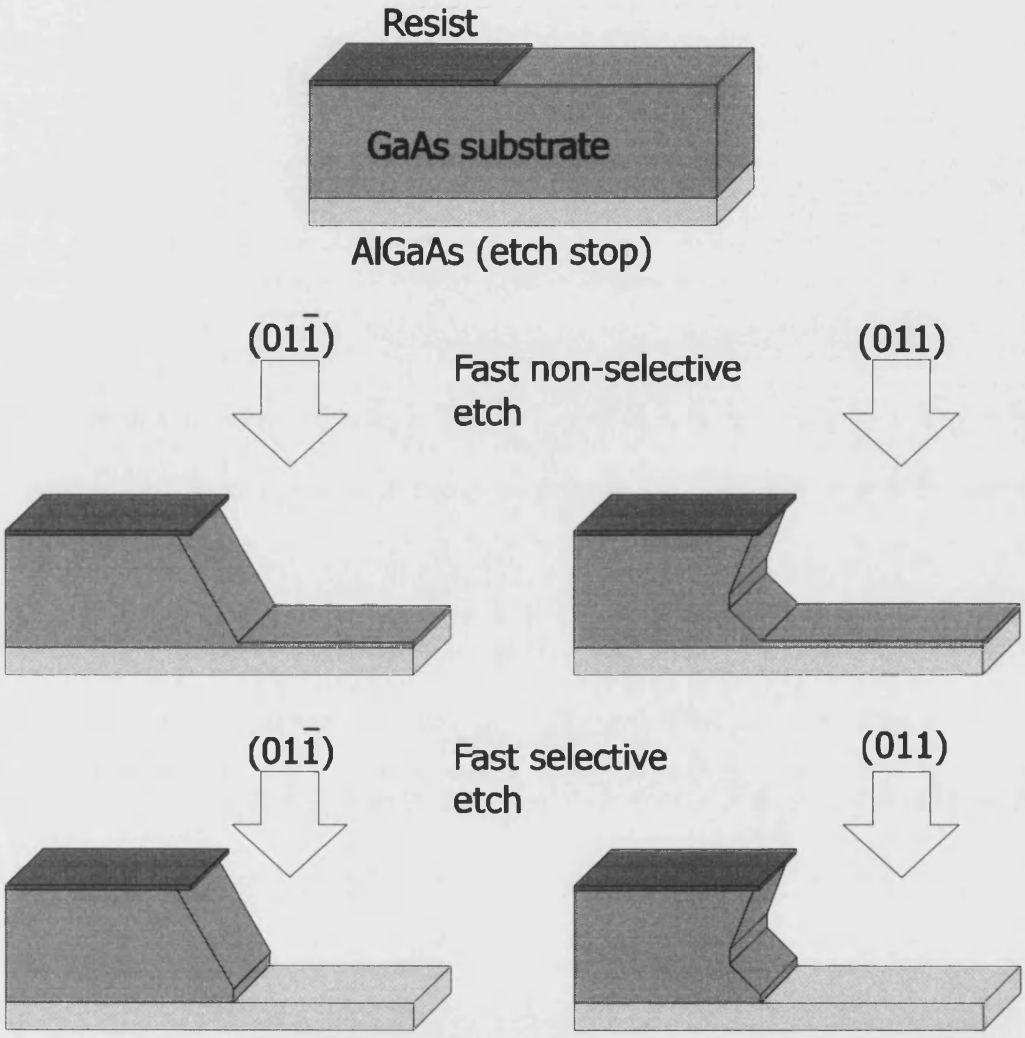

Figure 4.20 Illustration of the two-stage release etch process

The samples were mounted top side down onto microscope slides and resist spun on the back surface at 4000rpm. The etch pattern used was a simple rectangular mask, exposing the end of the sample beyond a desired point. This point was calculated from knowledge of the crystallographic orientation of the cantilever and the depth of the sample, which is estimated using a graduated microscope.

Once developed, the sample is etched in the fast non-selective etchant (etchant 4) to within 60-80μm of the sample surface. The etch rate of this solution, after it was allowed to cool to room temperature, was found to be ~10μm/min. The etch depth is monitored frequently using the graduated microscope until the desired profile is achieved. The sample is then removed from the slide in a bath of acetone and gently dried in N_2 gas. The sample is subsequently remounted on another microscope slide using black wax. The un-etched backside surface is then covered with resist, applied using a fine paint brush.

The remounted sample is then placed in the selective etchant solution at a pH of 8.30. The pH was lowered to reduce the build-up of contaminants and to increase the selectivity of the etch. A calibration of the solution etch rate is shown in Figure 4.21, where the two curves show the effect of cleaning the sample after 10 minutes in the $HCl:H_2O$ bath. The average etch rate drops from 2.8μm to 2μm if the sample is not cleaned.

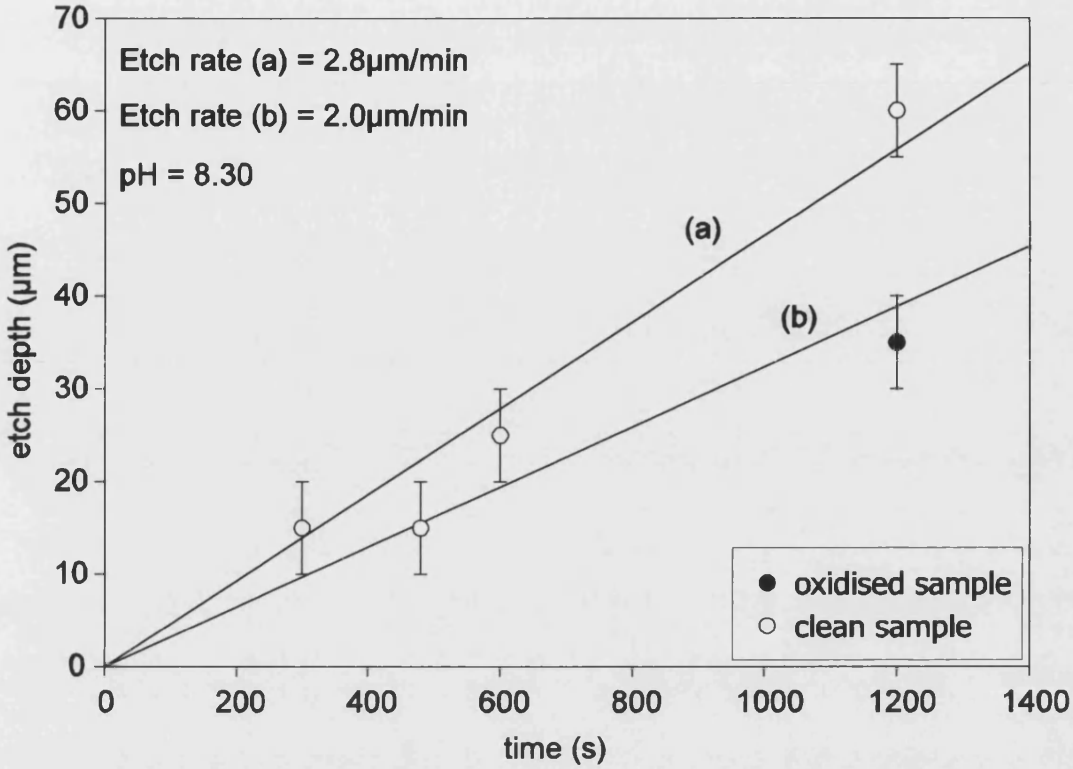

Figure 4.21 Calibration of etchant 6 at room temperature and pH = 8.30

The sample is etched for approximately 20 – 30 minutes in the selective etch solution, de-contaminating the sample every 10 minutes, until the cantilever is fully released from the substrate.

Figure 4.22 Released cantilever still encased in wax

Once released from the substrate the sample is placed in an acetone bath for 10 minutes to remove the resist and dried gently in N_2 gas, at this stage the cantilever is still fixed to the slide with black wax (Figure 4.22). The sample is then placed in a chloroform bath for up to 2 hours to remove the wax securing the sample to the slide. Once removed from the wax the cantilever is allowed to dry in air and placed on lint free tissue ready for mounting. The backside of a released cantilever is shown in Figure 4.23

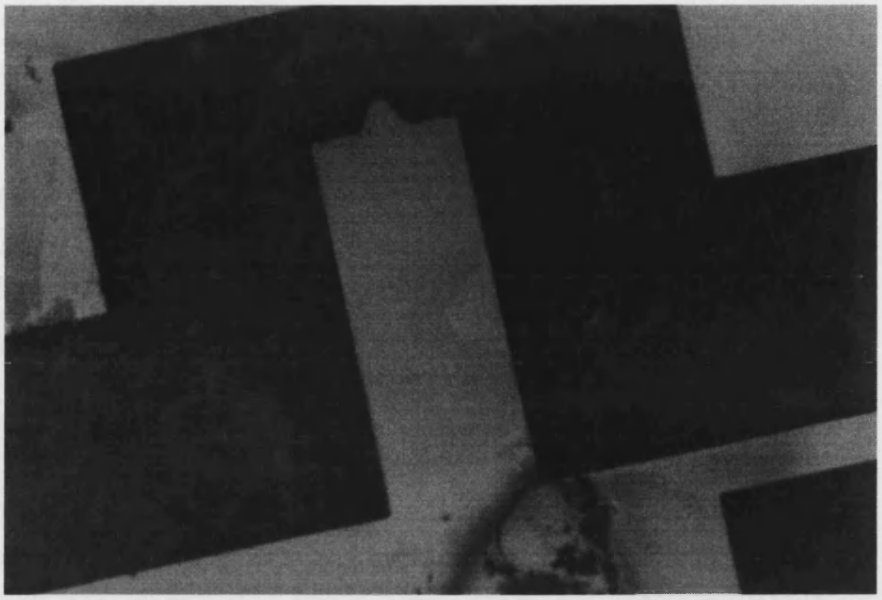

Figure 4.23 Released cantilever (backside)

4.5 Cantilever with 2DEG piezoresistive layer

The fabrication of the cantilever using the 2DEG for both the Hall sensor and the piezoresistive sensor has many advantages over the design with a separate sensor epilayer, the main advantages are:

- A reduced number of fabrication steps
- Removal of the possibility of parallel conduction between the two active epilayers
- Less complicated heterostructure design

There are, however, some drawbacks to this approach, which are:

- Increased sensitivity of the piezoresistive sensor to light and temperature changes
- Less control over the piezoresistive properties
- Unknown piezoresistive coefficient of 2DEG as well as its temperature-dependence.

Reducing the number of fabrication steps is the major advantage as the sensor yield is increased and fabrication time is reduced enormously. The disadvantage of the increased sensitivity to light and temperature is not a major problem, as the sensors are designed for use in a closed, temperature controlled cryostat. The inability to tailor the material properties should not present a problem so long as there is a reasonable piezoresistive response comparable to that of the dedicated piezoresistive cantilever.

The piezoresistive coefficient of the 2DEG system is unknown and has, to date, not been characterised in the literature. It does however exhibit a piezoresistive

response, as it has been exploited to achieve parametric amplification in a GaAs cantilever[11].

The 2DEG cantilever follows the same fabrication process as the n-AlGaAs piezoresistive cantilever with a few steps removed as they are now redundant. The following is a brief outline of the process, only detailing where the process has changed.

4.5.1 Step 1 (2DEG) : Sample preparation

Same as 4.4.1

4.5.2 Step 2 (2DEG) : Hall sensor and piezoresistor definition etch

Again the Hall sensor is defined as in the first etch, but now the piezoresistor is also defined in the same step. The etch depth is again ~70nm to ensure no conduction between the Hall sensor and the piezoresistor.

4.5.3 Step 3 (2DEG) : ohmic contact deposition

The deposition can now be performed in one step. The piezoresistor and the Hall sensor are contacted using the 'shallow' ohmic metal layer sequence. Once 'lift off' has been achieved the samples are alloyed at 400°C for 45 seconds, as there is no parallel conduction problem to consider.

4.5.4 Step 4 (2DEG) : Cantilever definition etch

Same as 4.4.5

4.5.5 Step 5 (2DEG) : AFM tip etch

Same as 4.4.6

4.5.6 Step 6 (2DEG) : Backside etch

Same as 4.4.7

The overall process still has six steps but far fewer sub-steps, reducing the fabrication time to approximately half that of the n-AlGaAs piezoresistive cantilever. A fabricated 2DEG cantilever is shown in Figure 4.24.

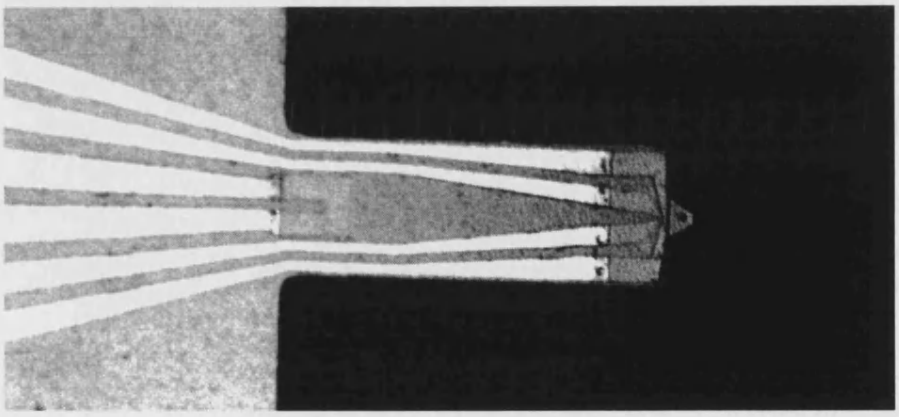

Figure 4.24 Fabricated 2DEG cantilever

4.6 Cantilever Mounting

For operation in a cryostat the cantilever is mounted on a custom made chip carrier or package as shown in Figure 4.25. The cantilever is fixed to the chip carrier using a two-component Oxford Instruments epoxy developed for use at low temperatures.

The cantilever sensor is electrically connected to the chip carrier using 12μm gold wire which is ultrasonically bonded to the cantilever at one end, and the package at the other. The cantilever is then ready to be attached to the low temperature scanning Hall probe microscope system.

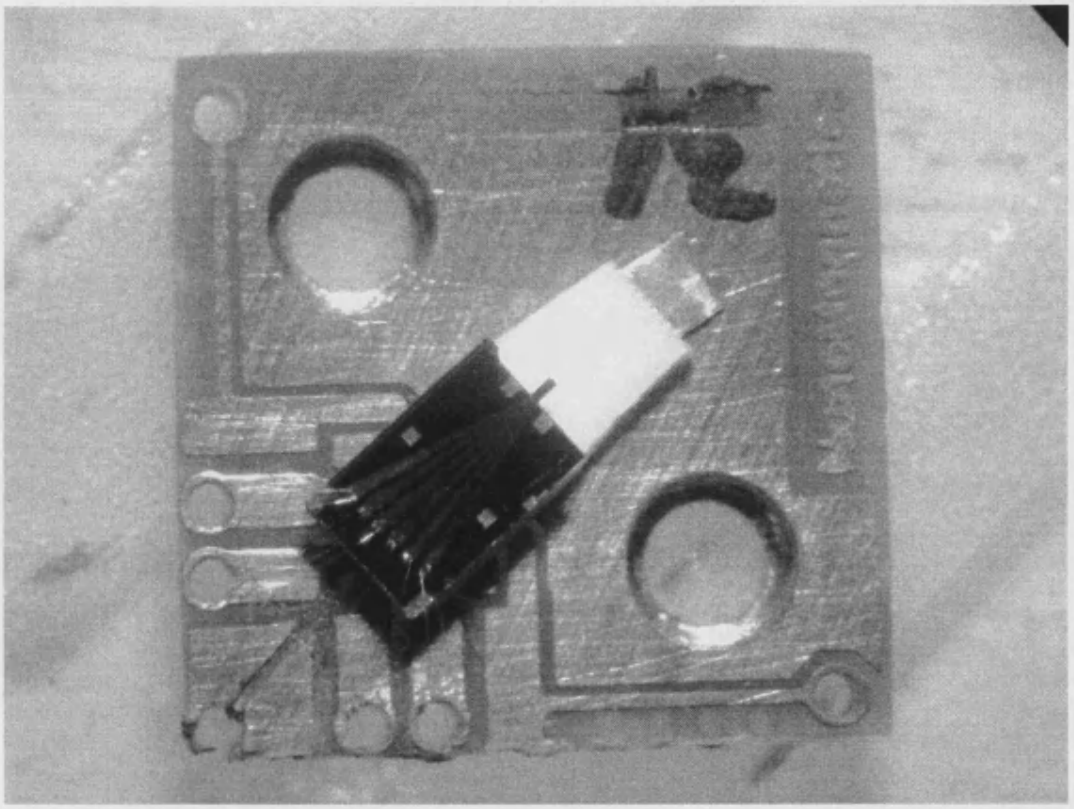

Figure 4.25 Mounted cantilever

4.7 Cantilever Bending

When mounting the cantilevers it was noticed that cantilevers were not entirely straight but exhibited a slight curvature along their length. This bending is due to the difference in thermal expansion coefficients of the GaAs/AlGaAs cantilever and the ohmic leads deposited on its surface, resulting in a cantilever that curves slightly downwards. This can be readily seen in Figure 4.24, where the tip of the cantilever

is in focus and the base is not. The magnitude of the bending is not simple to quantify, but it was found that annealing the ohmic leads onto the surface of the cantilever further accentuated the effect. The bending can be seen clearly in Figure 4.26. From the figure the one can estimate distance the tip has been displaced, $\Delta z \approx 10\mu m$.

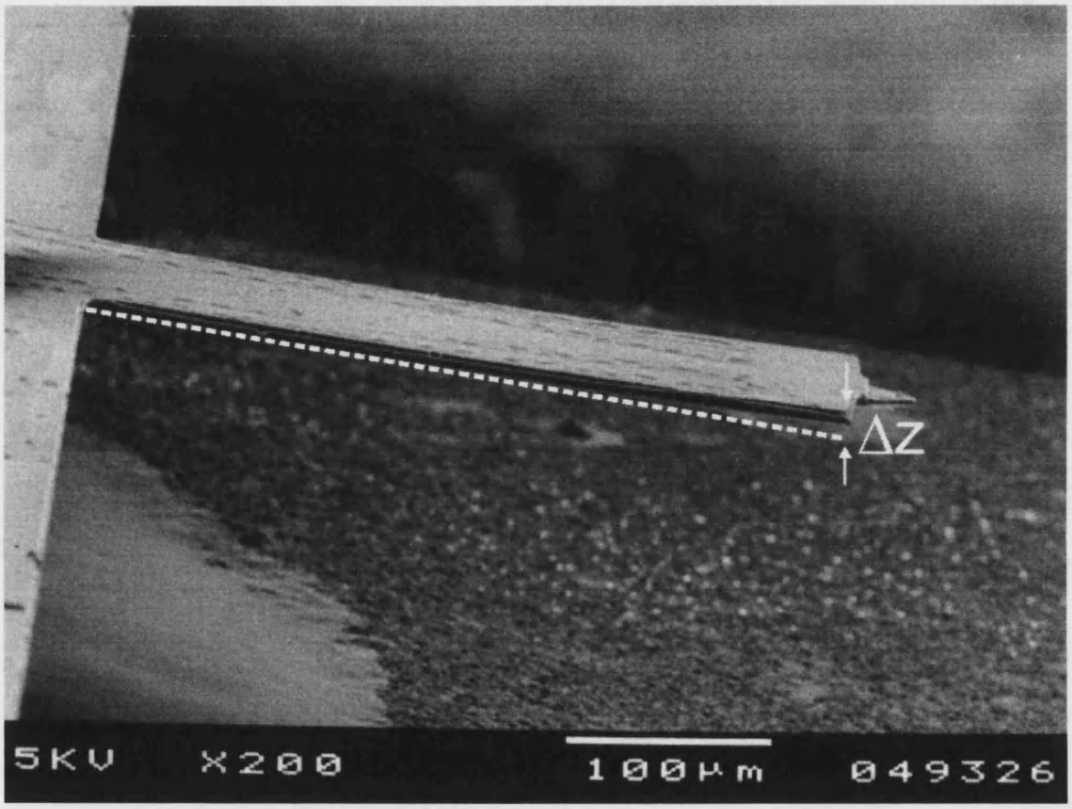

Figure 4.26 A cantilever exhibiting bending due to the cantilever – ohmic contact interface

4.8 References

[1] D. W. Shaw, *J. Electrochem. Soc.*, 874 (1981)

[2] M. Hatzakis, B. Canavello, and J. Shaw, *IBM J. Res. Develop.*, **24**, 452 (1980)

[3] J. Pinto, *Microfabrication of a GaAs/AlGaAs AFM cantilever with piezoresistive detection*, M. Phil thesis, University of Bath, 2000

[4] R. E. Williams, *Gallium Arsenide processing techniques,* Artech House (1984)

[5] K. Yamaguchi and S. Tada, *J. Electrochem. Soc.*, **143**, 2616 (1996)

[6] R. Shinohara, K. Yamaguci, Y. Suzuki, and W. Nabhan, *Jpn, J. Appl. Phys.*, **37**, 7151 (1998)

[7] B. K. Chong, H. Zhou, G. Mills, L. Donaldson, and J. M. R. Weaver, *J. Vac. Sci. Technol.* A **19**, 1769 (2001)

[8] J. J. LePore, *J. Appl. Phys.*, **51**, 6441 (1980)

[9] E. Moon and J. Lee, *J. App. Phys.*, **84**, 3933 (1998)

[10] T. Kitano, S. Izumin, H. Minami, T. Ishikawa, K. Sato, T. Sonoda, and M. Otsubo, *J. Vac. Sci. Technol. B*, **15**, 167 (1997)

[11] A. Dana, F. Ho, and Y. Yamamoto, *App. Phys. Lett.*, **72**, 1998

Chapter 5

5 Characterisation and Performance

5.1 Introduction

This chapter details some of the most important physical characteristics of the integrated sensor, such as the height and field resolution of the piezoresistor and the Hall sensor respectively. Other characteristics of the sensor such as the resonant frequency and Hall constant are also presented.

5.2 Piezoresistor

From previous studies[1] it is known that piezoresistors fabricated from $Al_{0.4}Ga_{0.6}As$ epilayers exhibit a piezoresistive response that is comparable with that of commercial p-Si cantilevers. The sensors produced in this earlier work were fabricated from a heterostructure whose structure is shown in Figure 5.1. Although this epilayer structure was found to produce cantilevers with a high piezoresistive response, it was also discovered that a 2DEG was formed at the interface between the piezoresistive n-$Al_{0.4}Ga_{0.6}As$ layer and the 3.5μm undoped GaAs epilayer placed underneath it. This resulted in a piezoresistor whose net resistance decreased rapidly with decreasing temperature, which would lead to a sensor with poor temperature stability. As mentioned in Chapter 3, in order to solve this problem cantilevers were fabricated entirely from $Al_{0.4}Ga_{0.6}As$ (Figure 3.12(b)).

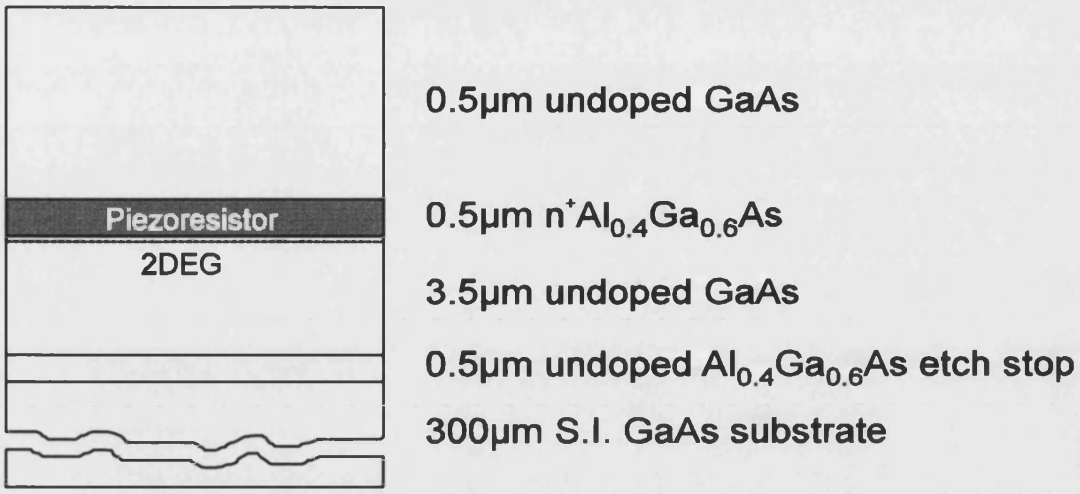

Figure 5.1 Piezoresistive Cantilever heterostructure from reference 1

Replacing the GaAs with AlGaAs in the cantilever did, however, introduce some additional problems. An increase in surface roughness was observed as was an (expected) large increase in the piezoresistor resistance.

5.2.1 Resistivity

The resistivity of the n-type doped $Al_{0.4}Ga_{0.6}As$ (1×10^{19} cm^{-3}) layer was previously measured[1] to be ~2.50×10^{-3} Ωm (300K), which would result in a piezoresistor (as in Figure 3.9) with a resistance of ~75kΩ. In practice it was found that the series resistance of the piezoresistors was ~25kΩ, a discrepancy which could be accounted for by the fact that a slightly different heterostructure was used in the previous study. It was found, however, that another important factor that determined the resistance of the piezoresistor was the presence of the undoped GaAs layer adjacent to the highly doped piezoresistive layer (Figure 5.2(a)). If this undoped GaAs layer was not present (Figure 5.2(b)) the resistivity was found to increase by at least an order of magnitude. This resulted in piezoresistors with series resistances of ~360kΩ.

This increase in resistivity almost certainly arose due to carrier depletion at the free-etched surface of the piezoresistor without the GaAs cladding layer. Lee *et. al.*[2] have

shown that when removing an undoped GaAs capping layer from an n-$Al_{0.23}Ga_{0.77}As$ layer ($7.0x10^{16}cm^{-3}$ Si doped, 50nm depth) the contact resistance is increased, although by only a few percent, not an order of magnitude. Their active system however, was a 2DEG underneath the n-$Al_{0.23}Ga_{0.77}As$ layer, so the situation is not directly comparable. They found that removal of the cap layer led to the rapid formation (less than 1 minute) of Al_2O_3 oxide at the sample surface. They further found that when alloyed a number of oxygen atoms diffused into the n-$Al_xGa_{1-x}As$ layer providing deep DX-like levels which trap the carriers as explained in section 2.2.7. and thus increasing the resistivity of the n-$Al_xGa_{1-x}As$ layer.

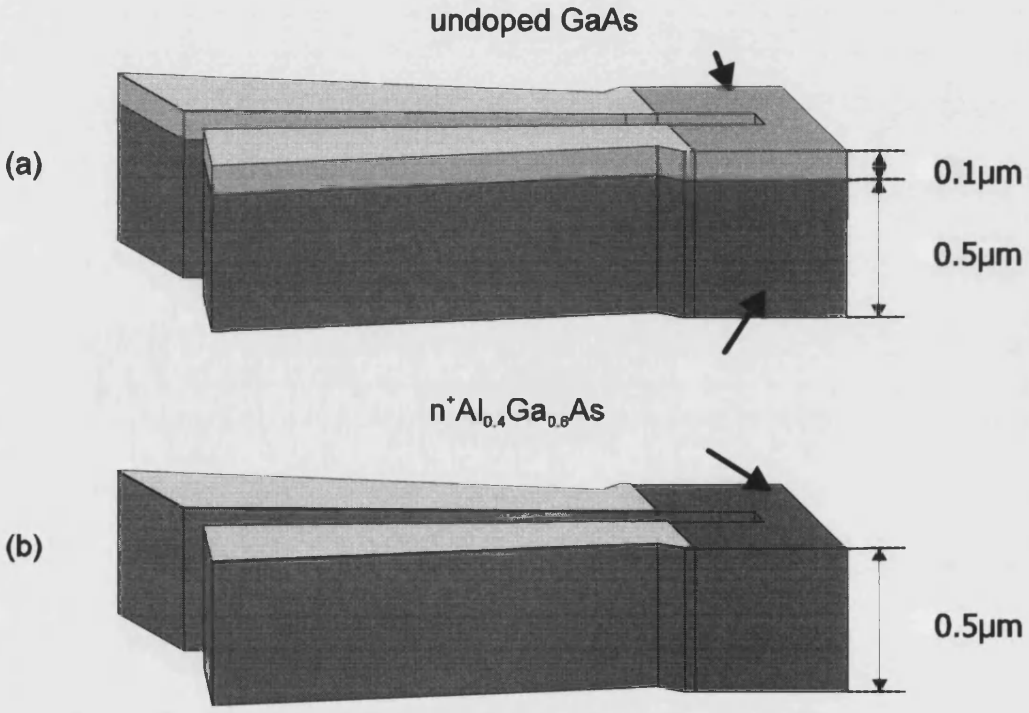

Figure 5.2 Side view of the piezoresistive sensor. (a) A thin layer of undoped GaAs left at the surface of the piezoresistor reduces its resistivity by up to an order of magnitude over a piezoresistor without it (b)

At low temperature (77K) the presence of the undoped GaAs layer has an even greater affect on the piezoresistor resistance. It had been reported that for piezoresistors fabricated from the epilayer design MBE2239 (Figure 3.12(a)), where an undoped GaAs epilayer is situated directly beneath the piezoresistive layer, resistances dropped from 25kΩ to 5kΩ at low temperature[3]. This would certainly

indicate the formation of a 2DEG when an undoped GaAs layer is adjacent to the piezoresistive epilayer.

For this reason the design of the epilayer structure was changed to prevent the 2DEG being formed, resulting in a cantilever made entirely of AlGaAs (Figure 3.12(b,c)). The resistance of piezoresistors fabricated from the new epilayer designs were found to be in excess of 20MΩ at low temperature if an undoped GaAs capping layer was not present. Although the formation of oxides and deep levels probably contributes we consider it likely that this primarily arises from carrier depletion due to Fermi energy pinning at the free-etched surface, an effect which would be most pronounced at low temperature. When the capping layer was present at low temperature, the series resistance for the piezoresistor was found to be approximately equal to the value at room temperature or slightly higher (~25-30kΩ). Consequently the undoped GaAs layer was required in all cantilevers using the later epilayer designs.

5.2.2 Resolution and Noise

One consequence of the increased series resistance of the piezoresistor can be a reduction in sensor height resolution, also known as the minimum detectable deflection (MDD). This is a measure of the cantilever's maximum vertical resolution, which is limited by its sensitivity and the noise within the measurement system. The sensitivity is determined by the piezoresistive coefficient of the material and the cantilever geometry (eqn 3.11). The main sources of noise are illustrated in Figure 5.3; these are the thermo-mechanical noise of the cantilever, Johnson noise of the piezoresistor and resistors in the bridge and the noise originating from the amplifying electronics. The other main source of noise (not shown in the diagram) is 1/f noise.

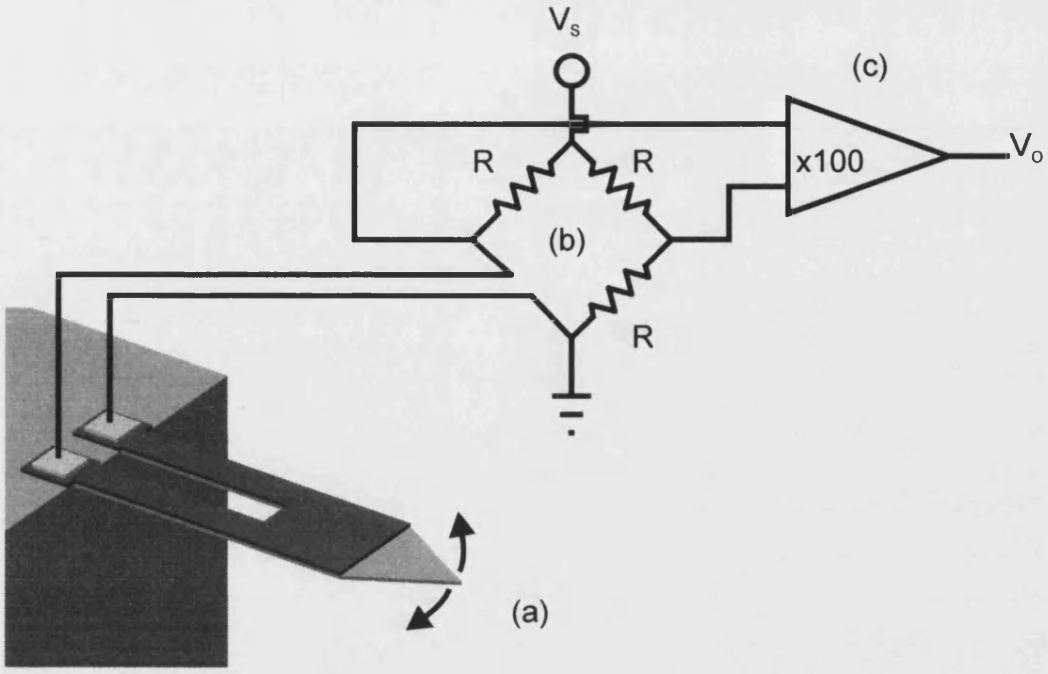

Figure 5.3 Three sources of noise in a piezoresistive AFM measurement. Thermo-mechanical noise (a), Johnson noise in the piezoresistor and bridge (b) and noise introduced by the amplifying electronics (c)

5.2.2.1 Thermo-mechanical noise

The intrinsic noise limit in an AFM measurement system is due to the thermo-mechanical noise of the cantilever (thermal excitation of the cantilever)[4]. This noise can be estimated from the following[5]

$$\left\langle \delta z_v^2(\omega = \omega_0) \right\rangle^{1/2} = \sqrt{\frac{4k_B T Q \Delta f}{\omega_0 k}} \qquad \text{(at resonance)} \quad (5.1)$$

$$\left\langle \delta z_v^2(\omega < \omega_0) \right\rangle^{1/2} = \sqrt{\frac{4k_B T \Delta f}{Q \omega_0 k}} \qquad \text{(off resonance)} \quad (5.2)$$

where the root mean square (rms) displacement noise due to thermal vibrations δz_v(rms), is dependent upon the temperature T, Boltzmanns constant k_B, the spring constant of the cantilever k, the bandwidth Δf, the quality factor of the resonance Q and the resonant frequency w_0. This gives δz_v(rms) = 0.001 nm/√Hz at resonance and δz_v(rms) = 0.01pm/√Hz off resonance. It is possible, with the use of optical AFM methods such as those mentioned in Chapter 1, to actually approach this

thermo-mechanical noise limit. For piezoresistive cantilevers, however, the MDD is degraded by 1/f, thermal Johnson and pre-amplifier noise. To compare the thermo-mechanical noise figures with the others it needs to be presented as a voltage fluctuation so we assume a typical sensitivity $S = 2 \times 10^{-6}$ nm^{-1} and a bridge voltage of 5V. The output of the measurement shown in Figure 5.3 would be (if R = resistance of piezoresistor)

$$V_O = \frac{1}{4} V_S S G \delta z \tag{5.3}$$

where V_S is the supply voltage, S is the sensitivity, G the gain and δz the distance moved by the cantilever tip. This would result in a thermo-mechanical noise output voltage before amplification of δV_v(rms) = 2.5 nV/√Hz at resonance and δV_v(rms) = 25 pV/√Hz off resonance.

5.2.2.2 1/f noise

1/f noise is a much studied, little understood phenomenon that is present in nearly all physical systems. Occasionally called "flicker noise" or "pink noise", it is a type of noise whose power spectra, P(f), as a function of the frequency f behaves like P(f) = $1/f^{\alpha}$, where the exponent α is usually close to 1. In contact AFM this is the main noise limit to the sensor's resolution as it is a static measurement. Non-contact AFM modes avoid this noise by sampling at frequencies close to the resonant frequency of the cantilever, greatly reducing its effect. It can be estimated from the empirical relation given by Hooge[6,7]

$$\left\langle \delta V_f^2 \right\rangle^{1/2} = \sqrt{\frac{\alpha}{fN} V^2} \tag{5.4}$$

where $\alpha = 2 \times 10^{-9}$ is an empirical parameter, f the frequency, N the number of carriers in the device and V the bridge voltage. This relationship is plotted in Figure 5.4. It can be seen that at low frequencies the noise amplitude is very large exceeding 0.1μV/√Hz below 1Hz. At higher frequencies, however, the noise drops

off sharply, approaching 1nV/√Hz at 1kHz. As all our measurements were conducted at frequencies much higher than this, 1/f noise should be negligible.

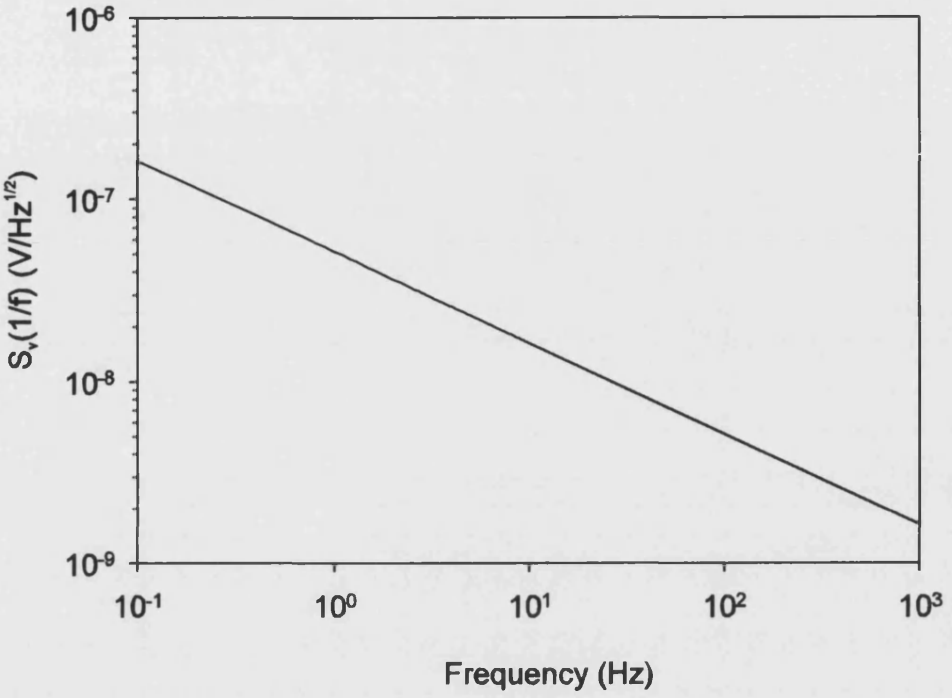

Figure 5.4 Plot of the 1/f noise spectrum as given by eqn. 5.4

5.2.2.3 Amplifier noise

Amplifier noise is due to the noise introduced by the amplifier electronics. A low noise amplifier is used to amplify the small fluctuations in the piezoresistor resistance via a Wheatstone bridge (Figure 5.3(c)). The amplifiers used in this project were all ultra low noise AD625 amplifiers with a noise stated as 4nV/√Hz[8].

5.2.2.4 Johnson noise

Johnson noise is the noise generated by thermal agitation of electrons in a conductor. Also known as "white" or "Gaussian" noise it has a noise spectrum given by P(f) = $1/f^0$, therefore is equal for all frequencies. The voltage fluctuation in a resistor under load is given by

$$\left\langle V_J^2 \right\rangle^{1/2} = \sqrt{4k_B TR\Delta f} \qquad (5.5)$$

where R is the total resistance of the piezoresistor and the bridge and Δf is the measurement bandwidth. For a typical cantilever $R_{piezoresistor}$ = 25kΩ, giving R_{eff} = 2R, yielding V_J(rms) = 28nV/√Hz. This makes Johnson noise, for measurements above 1Hz, the dominant noise contribution. Therefore, for two identical piezoresistive cantilevers with equal sensitivities their MDD will be a function of the square root of their series resistance, e.g. if R_1 = 25 kΩ and R_2 = 300kΩ, R_1 will have a MDD √12 smaller than R_2.

As we have determined Johnson noise to be the limiting noise floor to our experiment we can determine the MDD for our cantilever presented in Chapter 3. Recalling that the sensitivity is given by

$$S = \frac{\Delta R}{R\Delta z} = \frac{3\pi_L Et(1-l/(2L))(1-t_{PR}/t)}{2L^2} \tag{5.6}$$

and combining eqns. 5.3, 5.5 and 5.6 we can obtain an expression for the MDD (with no gain)

$$MDD = \frac{4V_J(rms)}{SV_S} = \frac{8}{3}\frac{V_J(rms)L^2}{V_S\pi_L Et(1-l/(2L))(1-t_{PR}/t)} \tag{5.7}$$

Using the parameters given in Chapter 3 (Table 3.1), MDD = 2.8pm/√Hz. We can compare this value to that given for commercial p-Si piezolevers[9], which for a NC cantilever has a MDD = 0.7pm/√Hz, giving a higher resolution, much of which can be attributed to the lower resistance of the p-Si piezoresistor (~2kΩ). At low temperature, assuming a constant sensitivity and resistance, the MDD is simply

$$MDD(77K) = MDD(300K) * \frac{\sqrt{77}}{\sqrt{300}} \cong \frac{MDD(300K)}{2} \tag{5.8}$$

Using a spectrum analyser it is possible to measure the noise spectrum of the piezoresistors. We used a HP 3562A spectrum analyser, with a frequency range of 0-100kHz to do this.

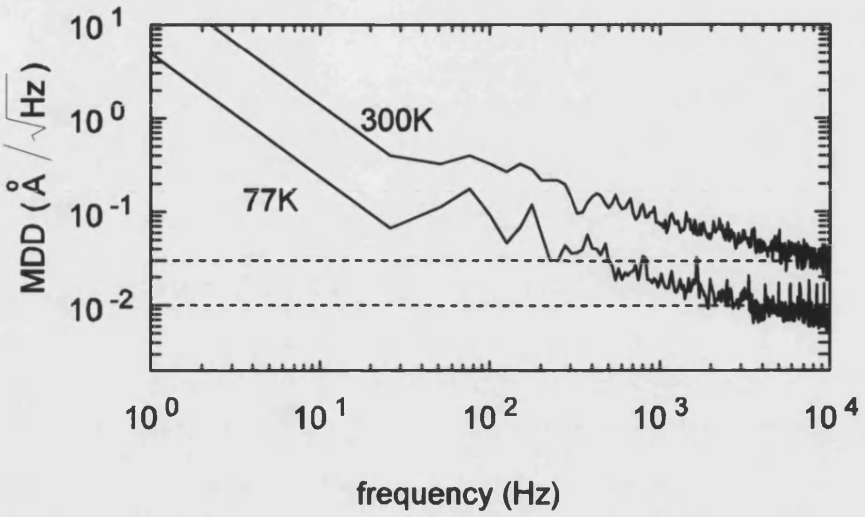

Figure 5.5 Noise spectrum of a CUA2525 piezoresistor at 300K and 77K. Dashed lines are Johnson noise limit at 300K and 77K

From Figure 5.5 it can be seen that the noise of the piezoresistors approaches the Johnson noise limit at higher frequencies. The amount of 1/f noise is, however, much larger than expected from eqn. 5.4. This has been found to be true in many piezoresistive cantilevers and the 1/f noise is found to increase as the thickness of the cantilever decreases[10].

5.2.3 Sensitivity

The sensitivity of the cantilevers can be determined experimentally by applying a known force or displacement to the tip of the cantilever. This can be achieved in a variety of ways, including attaching small weights to the end of the cantilever[11] or using a second calibrated AFM cantilever. The method we employed used a calibrated scanning Hall probe microscope scanner tube to apply a known deflection to the tip of the cantilever and measure the resulting change in voltage across the bridge (Figure 5.6).

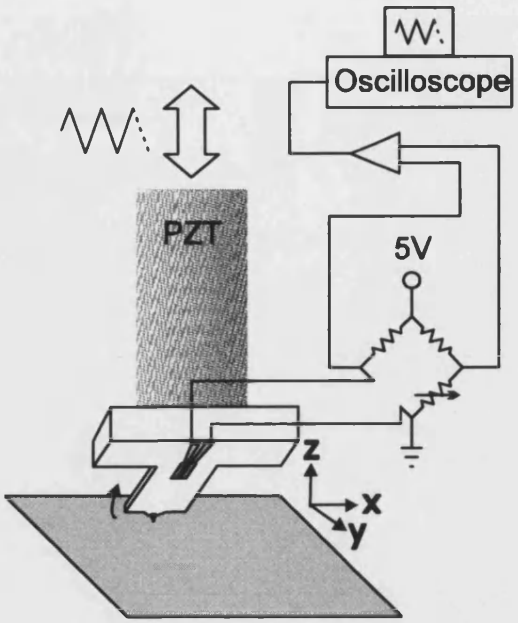

Figure 5.6 Setup for determining the cantilever sensitivity

A sawtooth voltage pattern is applied to the piezo tube and the resulting cantilever response is recorded using a storage oscilloscope, the sensitivity can then be calculated using eqn. 5.3. Using this technique the sensitivity of various cantilevers was recorded and these are shown in Table 5.1. The sensitivity is given for both types of piezoresistor as described in Chapter 4, containing bulk-doped and 2DEG piezoresistors. The results, where available, are given at 300K and 77K.

The results in Table 5.1 highlight the problems encountered when using GaAs devices during measurement, their fracture strength being much lower than those fabricated from silicon. Many cantilevers were partially or totally damaged either during characterisation or operation. From the values that were obtained, sensitivities were observed close to those predicted by eqn. 3.11.

Cantilevers 12 and 16 were based on an older design that restricted the amount of stress applied to the piezoresistor, which accounts for their reduced sensitivity. Cantilever 19 was fabricated to the design described in Chapter 3 and should therefore be the most appropriate device to compare with the theoretical sensitivity

of 8 x $10^{-6}nm^{-1}$ (cantilever 19 actually slightly exceeds this). Cantilever 1 was fabricated using the 2DEG for both the piezoresistor and Hall sensor. As the piezoresistive coefficient of the 2DEG was unknown the expected piezoresistive response could not be estimated. The sensitivity recorded is comparable to that of the cantilevers with the dedicated bulk-doped piezoresistive epilayer and actually exceeds the sensitivity of the cantilevers of the same design (12 and 16). Data from a commercially available p-Si piezoresistive cantilever is also given in Table 5.1 for comparison.

Table 5.1 Cantilever Sensitivity

Cantilever Number	Wafer Source	Piezoresistor type	Sensitivity (nm^{-1}) 300K	Sensitivity (nm^{-1}) 77K
1	NU2188	2DEG	8.00×10^{-6}	N/A*
12	CUA2525	Piezoresistive	1.20×10^{-6}	N/A†
16	CUA2525	Piezoresistive	1.55×10^{-6}	3.40×10^{-8}
19	CUA2525	Piezoresistive	1.17×10^{-5}	N/A‡
Piezolever§		p-Si Piezo	4.00×10^{-6}	N/A

* Resistance of piezoresistor >20MΩ at 77K

† Resistance of piezoresistor 78kΩ at 77K, response too small to measure

‡ Coupling between Hall probe and piezoresistor prevented measurement

§ Data from Veeco Metrology Group, PiezoleversTM, datasheet

5.2.4 2DEG cantilevers

The sensitivity of a 2DEG piezoresistive cantilever is shown in Table 5.1. The use of the 2DEG as a piezoresistor has several drawbacks as outlined in section 4.5. One further problem encountered with 2DEG devices is the fact that there is a maximum current which can be passed through the device before it is permanently damaged. As a result of this the Wheatstone bridge must be slightly modified to reduce the amount of current which is passed through the piezoresistor as shown in Figure 5.7.

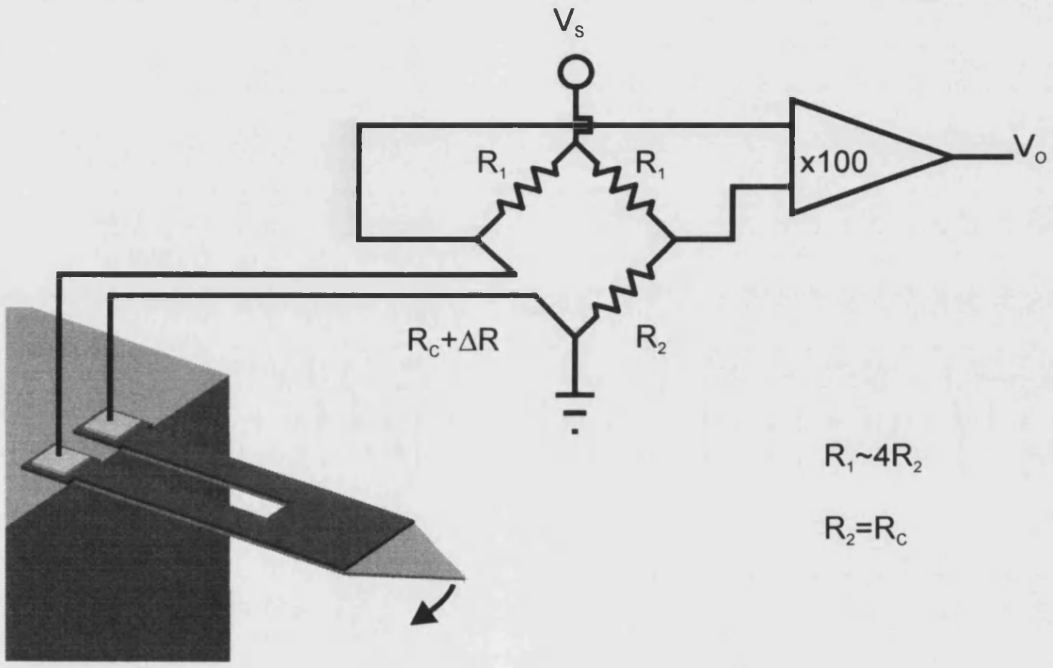

Figure 5.7 Bridge arrangement for a 2DEG piezoresistive cantilever

The two top resistors (R_1) are chosen with values approximately 4 times the resistance of the 2DEG piezoresistor, which has a resistance of approximately 20kΩ at room temperature. At low temperature this can fall to ~2kΩ, so the bridge needs to be changed accordingly. This bridge arrangement reduces the sensitivity of the measurement, as the current through the piezoresistor is now reduced by a factor of 4.

The change in output voltage can be found from (not including gain)

$$\begin{aligned} V_O &= V_S \frac{(R_C + \Delta R)R_1 - R_2 R_1}{(R_C + \Delta R + R_1)(R_1 + R_2)} && \Delta R << R_C \\ &\approx V_S \frac{\Delta R R_1}{(R_C + R_1)(R_1 + R_2)} && R_2 = R_C \\ &= V_S \Delta R \frac{R_1}{(R_C + R_1)^2} \end{aligned} \tag{5.9}$$

Comparing this with eqn. 5.3 we can see that if $R_C = R_1$ we arrive at the same answer. Writing eqn. 5.9 in the same terms as 5.3, and $R_1 = 4R_C$, gives

$$V_O \approx \frac{1}{6} V_S GS\delta z \tag{5.10}$$

resulting in a reduction of output voltage of approximately 50% for a 2DEG cantilever with the same sensitivity.

5.2.5 Resonant frequency

Every micro-machined cantilever has a natural frequency at which its vibration amplitude is strongly amplified as outlined in section 3.2.3.1. This natural frequency (known as the resonant frequency) is different for each cantilever due to slight differences which occur during the fabrication process. Recalling eqn. 3.5 for the first resonant frequency

$$\omega_0 \approx \sqrt{\frac{k}{0.24m}} \tag{5.11}$$

where k is the spring constant of the cantilever and m the mass. If we excite the cantilever with a sinusoidal waveform at a certain frequency ω and amplitude a_0, we

can calculate the amplitude of the driven vibrating cantilever from the standard formula[5]

$$A(\omega) = \frac{a_0 Q}{\left[Q^2(1-\omega/\omega_0)^2 + \omega^2/\omega_0^2\right]^{1/2}} \tag{5.12}$$

where the amplitude $A(\omega)$ of the cantilever tip is a function of the frequency ω, the resonant frequency ω_0, the driving amplitude a_0 and the quality factor Q. The quality factor is a measure of the energy stored divided by the energy lost during a single cycle. It is dependent upon many factors such as the shape of the cantilever, the material and the medium in which the cantilever is vibrated. The resonant frequency spectra for cantilever 19 under different conditions are shown in Figure 5.8

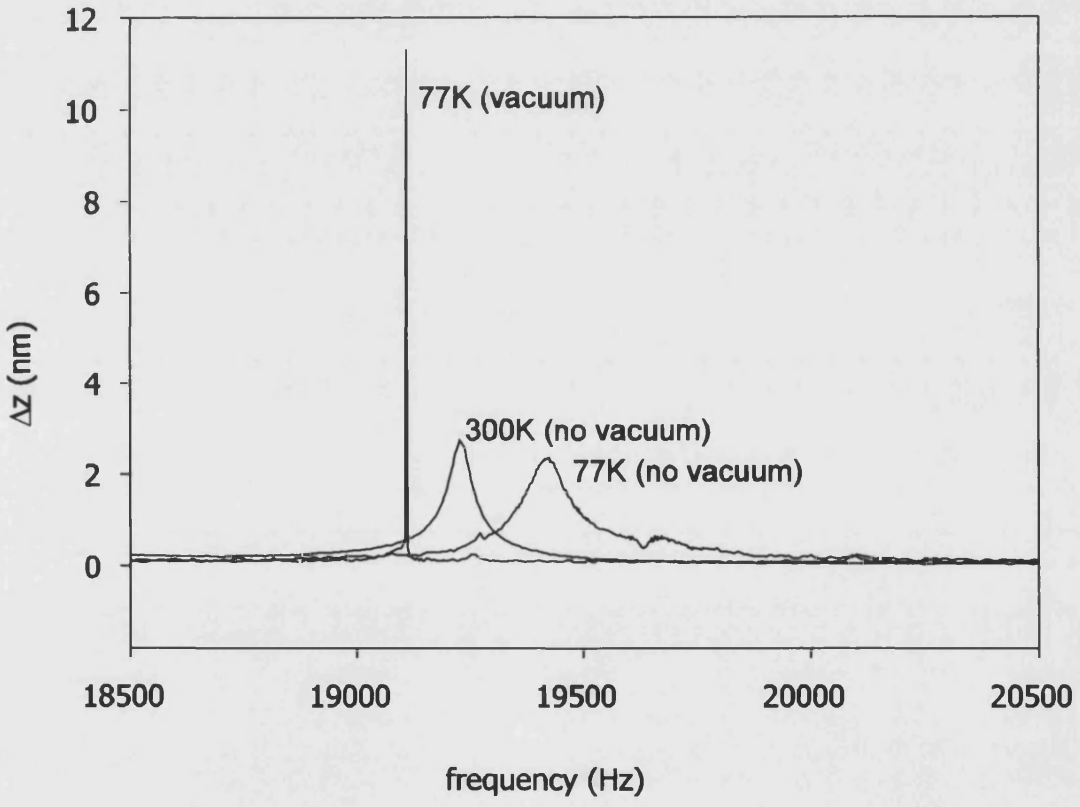

Figure 5.8 Resonant response of a cantilever under different ambient conditions

5.3 Hall Probe

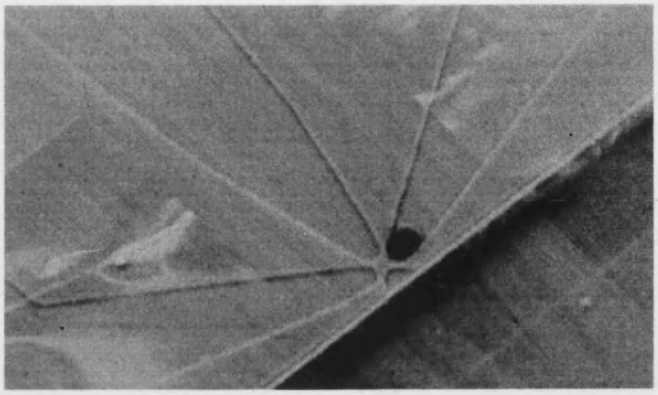

Figure 5.9 1μm Hall cross fabricated at the end of a cantilever

The 2DEG Hall probe fabricated at the end of the cantilever was based on designs used to fabricate standard STM-tracking SHPM Hall probes. The heterostructure, and to a certain extent the design, is very similar to those used for Hall probes already demonstrated using an AlGaAs 2DEG[12] and as such the properties of the Hall sensor were expected to be very similar.

The presence of the piezoresistor on the same chip does, however, introduce some problems not present in standard STM-SHPM probes, as any cross-coupling between the two sensors would be detrimental to the performance of both. This coupling was found to occur with several cantilevers and was attributed mainly to, (a) etches that were not deep enough to totally isolate both devices (b) incorrect alloying of the shallow ohmic contacts which then shorted to the piezoresistive layer allowing parallel conduction between the 2DEG and the piezoresistive layers. Under these circumstances simultaneous use of the sensors was not possible, only one of the sensors could be used at a given time.

5.3.1 Hall coefficient R_H

The Hall coefficient for the 2DEG Hall sensors was found to be fairly constant for all sensors and only varied slightly from room to low temperature. Table 5.2 lists the Hall coefficient for several sensors, with the value at room temperature being consistently smaller than that at low temperature.

Table 5.2 Hall Coefficients for several cantilevers

Cantilever Number	Hall Coeff (300K) (ΩmT^{-1})	Hall Coeff (77K) (ΩmT^{-1})
1	1.7	3.2
12	2.0	2.9
16	2.5	3.0
19	2.6	N/A

5.3.2 Voltage offset

When a current is passed through a Hall sensor it produces a characteristic offset voltage that arises due to any slight asymmetry of the Hall voltage leads. This misalignment produces a voltage drop across the contacts, superimposing an offset voltage on the Hall voltage, which must then be "nulled" using the measurement electronics. The value of the offset can vary depending on the fabrication quality of the Hall sensor, with better fabricated Hall sensors producing smaller offset voltages.

5.3.3 Noise and resolution

Noise in the Hall sensor arises from most of the same sources as those outlined in the previous section for the piezoresistor. 1/f noise once again dominates at low frequencies and amplifier noise is also present (the same amplifiers were used for Hall voltage and piezoresistor amplification), and the dominant noise contribution at high frequencies is once again due to Johnson noise. The Johnson noise, particularly at room temperature, determines the field resolution of the Hall sensor known as the minimum detectable field (MDF). The MDF is analogous to the MDD in so far that it is the limit at which a signal can be measured above the noise in the measurement system. It can be expressed by combining eqn. 3.12 and 5.5 to give

$$MDF = \frac{\sqrt{4k_B T R_V \Delta f}}{I_H R_H} \tag{5.13}$$

where R_v is the series resistance of the Hall sensor, Δf is the measurement bandwidth, I_H the Hall current and R_H the 2D Hall coefficient. It can be seen from eqn. 5.13 that the MDF can be reduced greatly at lower temperature due to a number of factors. Firstly the MDF is directly proportional to the square root of the temperature; secondly the Hall junction resistance R_v is reduced by up to an order of magnitude between 300K and 77K due to the nature of the 2DEG Hall sensor. Lastly the Hall current I_H has a limit, called I_{max}, above which the 1/f noise increases abruptly. At room temperature I_{max} is approximately 4μA for a 1μm Hall sensor and at low temperature (77K) I_{max} can be increased to 20μA or more depending on the sensor, without a significant increase in noise.

To estimate the MDF at room temperature we can use the following figures from cantilever 16, $R_v = 45k\Omega$, $R_H = 2.5\Omega mT^{-1}$, $I_H = 4\mu A$ and $T = 300K$, which results in an MDF (300K) = 2.7×10^{-6} T/√Hz. At low temperature, $R_v = 10$ kΩ, $R_H = 3\Omega mT^{-1}$, $I_H = 16\mu A$ and $T = 77K$ which gives MDF (77K) = 1.4×10^{-7} T/√Hz.

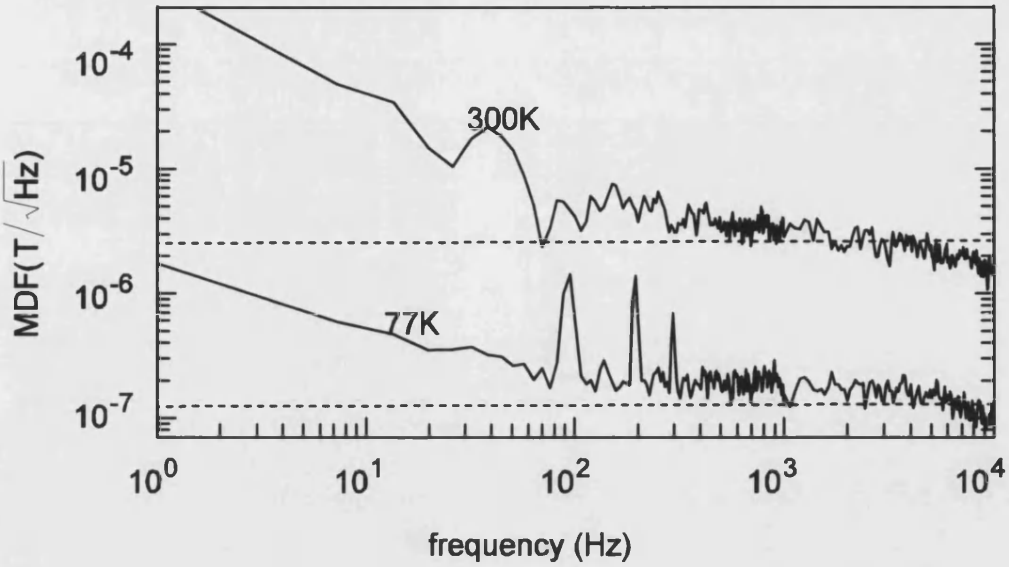

Figure 5.10 Frequency response of the Hall sensor at 300K and 77K for cantilever 16. Dashed lines are the Johnson noise limit at 300 and 77K

The noise spectrum for cantilever 16 is shown in Figure 5.10, the 1/f noise is seen to be dominant up to ~100Hz after which the noise approaches the MDF limit imposed by the Johnson noise. After ~10kHz the noise drops off at roughly 10dB per decade due to the amplifier.

5.4 References

[1] J. Pinto, *Microfabrication of a GaAs/AlGaAs AFM cantilever with piezoresistive detection*, M. Phil thesis, University of Bath, 2000

[2] J. Lee, Y. Kim, H. M. Yoo, G. Y. Lee, *J. Vac. Sci. Technol. B,* **17**, 1034 (1999)

[3] J. Pinto, Unpublished

[4] D. P. E. Smith, *Rev. Sci. Inst.*, **66**, 3191 (1995)

[5] D. Sarid, *Scanning force microscopy*, OUP, 1991

[6] F. N. Hooge, *Phys. Lett. A*, vol. 29, 139 (1969)

[7] O. Hansen and A. Boisen, *Nanotech.*, **10**, 51 (1998)

[8] Analog Devices, Datasheet AD625

[9] Veeco Metrology Group, Piezolevers™, datasheet

[10] J. A. Harley, *Advances in piezoresistive probes for Atomic Force Microscopy,* PhD. thesis, Stanford University, 2000

[11] J. P. Cleveland, S. Manne, D. Bocek, P. Hansma, *Rev. Sci. Instum*, **64**, 403 (1992)

[12] A. Oral, S. J. Bending, and M. Henini, *App. Phys. Lett.*, **69**, 1324 (1996)

Chapter 6

6 Results and discussion

6.1 Introduction

This chapter is presented in two parts, firstly the scanning system and scanning method are discussed, secondly, the experimental results, obtained using the fabricated sensors, are presented and discussed. Results for several different sensors and samples are given. These were obtained using the SHPM facilities at Bilkent University, Turkey and the University of Bath.

6.2 Scanning system

To achieve AFM-guided scanning Hall probe microscopy, a customized STM-guided SHPM was used (Figure 1.3). Several modifications to the STM system were needed for AFM operation. Firstly the connection to the piezoresistor needed to be addressed. The STM system uses four connections to the Hall probe and one connection to the STM tip, the AFM requires four connections to the Hall probe and two to the piezoresistor. This requires a slight modification when mounting the sensor on the chip carrier as shown in Figure 6.1.

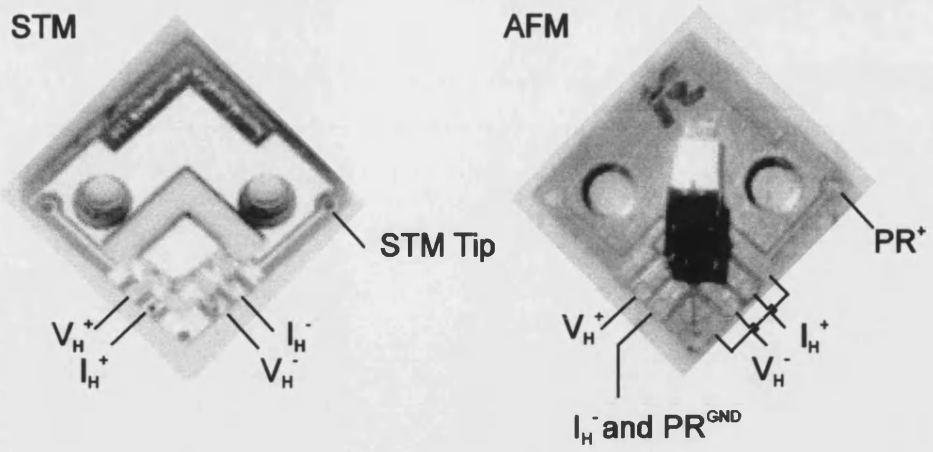

Figure 6.1 Mounted STM and AFM guided Hall sensors

A typical STM guided Hall probe is shown on the left of Figure 6.1, on the right is an outline of how an AFM guided Hall probe is connected to the chip carrier. The problem of only 5 connections on the microscope mounting head was overcome by connecting both the negative Hall current connection and the piezoresistor ground connection to a common ground. A further problem that was encountered was connecting the positive piezoresistive lead to the STM tip junction. This was solved by splitting the ground junction at the bottom of the chip carrier, and connecting the half (which was then isolated from earth) to the STM tip junction by the use of silver epoxy. The chip was then mounted on the STM-SHPM head.

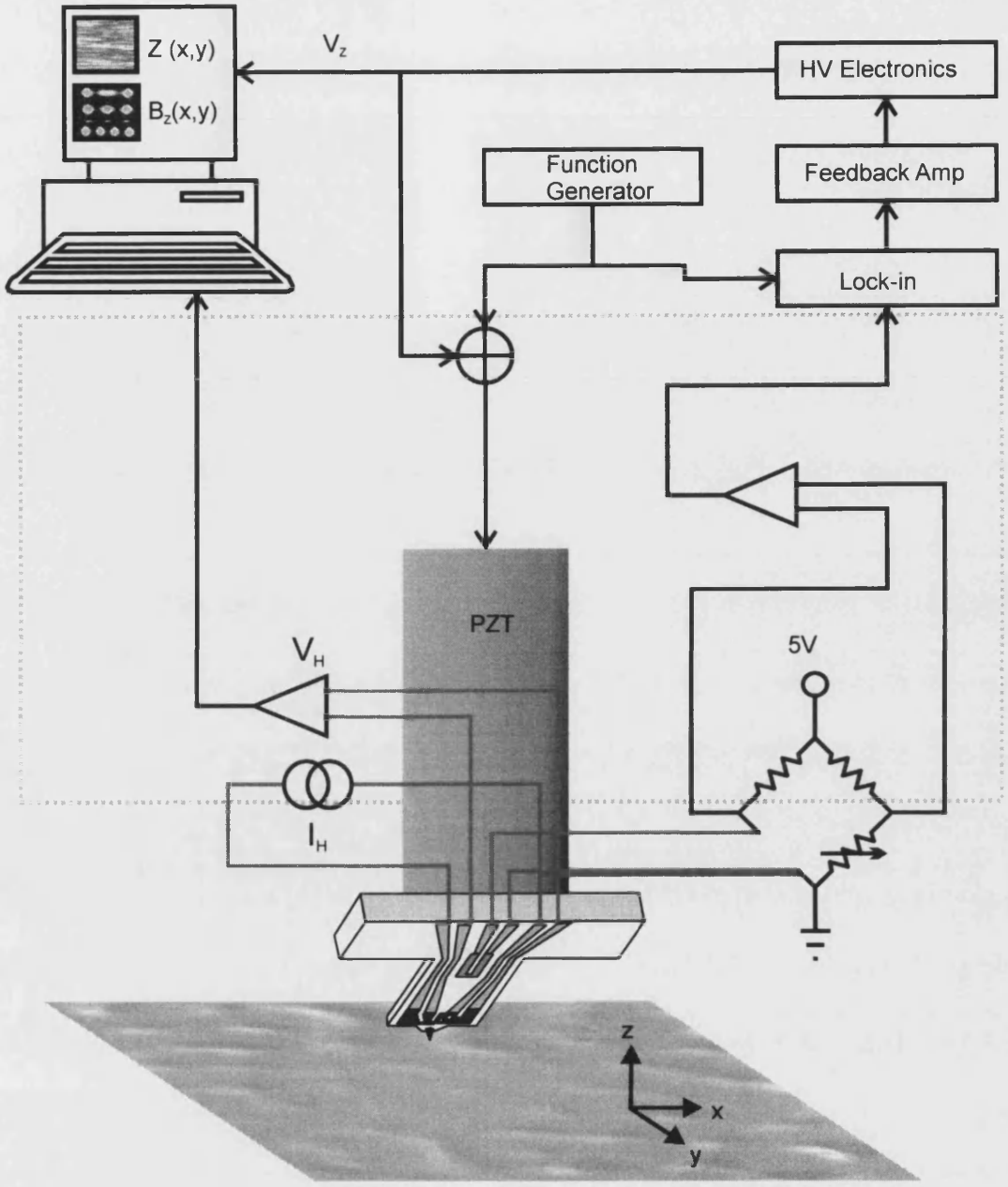

Figure 6.2 Diagram of the AFM guided SHPM measurement system

The AFM guided SHPM system is shown schematically in Figure 6.2. The system is made up of three main components. The first component, the sensor, is mounted at the end of the microscope piezotube using the chip carrier. The second component is the pre-amplifier (bordered broken grey line in Figure 6.2) which is built in a separate shielded metal enclosure to ensure minimal electrical interference. Both the Hall voltage pre-amplification and piezoresistor amplifiers are situated in this

enclosure. Typical figures for gain were 1000x for the Hall voltage and 100x for the Wheatstone bridge amplification. The Hall signal from the preamplifier can then be further amplified (1-1000x) in the main control electronics. The latter provide the high voltage (HV) signals to drive the piezotubes used to position the microscope head in x, y and z, the feedback for the z positioning, the Hall current and the additional Hall voltage amplification. The control electronics are connected to a PC which is used to set certain control parameters (e.g. Hall current, feedback level etc.) and record the values of desired experimental values (e.g. Hall voltage, sensor height).

6.3 Topographic Scanning method

Topographic scanning of a sample using the measurement system shown in Figure 6.2 first requires certain parameters of the sensor to be known. The resonant frequency of the cantilever is one of the most fundamental if the scans are to be performed in non-contact/intermittent contact mode (section 1.2.3.2-3). In this mode the cantilever is oscillated by the use of a precision frequency generator whose signal is added to the z voltage of the piezotube (as in Figure 6.2). It is oscillated on or close to the resonant frequency and then the cantilever is brought within close proximity to the sample and a change in resonant amplitude or frequency is used to control the cantilever height.

During experiments it was found that the amplitude of the cantilever motion was attenuated as it got closer to the sample, even at relatively large distances >20μm. At these distances this is not due to an interatomic interaction, but is caused by air damping of the resonance due to the proximity of the sample surface. This was verified by measuring the Q factor of the cantilever as it approached the surface. The Q factor was found to reduce by up to an order of magnitude as it went from a free cantilever to a cantilever ~1-2μm from the sample surface.

As the system was not optimised for AFM detection, intermittent contact mode was used, as this had the largest observable change in amplitude as the tip just comes

into contact with the surface. Using the value of the amplitude of the cantilever motion just before the cantilever starts to "tap" the surface as a reference; the feedback was set to 82% of this amplitude, as this has been shown to be the point of maximum inflection in the force gradient[1].

Using this method (known as "slope detection method" [2]) it is possible to achieve high sensitivity with cantilevers with a large Q factor but at the expense of increased response times of the cantilever. The response of the system can be estimated from[2]

$$\tau = \frac{2Q}{\omega_0} \tag{6.1}$$

This is effectively a bandwidth limitation, restricting the speed at which the cantilever can be scanned across the sample surface. Therefore high Q cantilevers will require a low scan speed. It was found during our experiment that cantilevers with Q factors above 10000 were not suitable for AFM operation in the slope detection mode. There are several solutions to this, which were not attempted in this project, including a frequency modulation detection system[2] or active Q control techniques[3].

6.4 Magnetic Scanning method

The Hall sensor is used to measure the local surface magnetic induction as the cantilever moves over the sample under the guidance of the AFM sensor. This should keep the sensor distance from the sample constant throughout the scan. The bandwidth of the Hall sensor can be set in the control electronics, with lowest setting used (100Hz) for most low speed scans to minimise noise. For high speed (real time) scanning it can be increased up to 100 kHz, with a corresponding increase in noise ($\propto\sqrt{\Delta f}$).

The Hall current is also set in the control electronics. As detailed in Chapter 5, the maximum current at room temperature is ~4μA, at 77K this can be increased to

~20μA when the Hall sensor permits. The corresponding Hall voltage that is measured by the control electronics is not an absolute value as each Hall probe has a characteristic offset voltage, introduced by asymmetric Hall cross fabrication. This offset voltage is nulled in the control electronics and a relative value recorded.

6.5 Test samples

To verify the topographic scanning capability of the AFM cantilever several test samples were imaged. These samples are arrays of primitive shapes such as rectangles and triangles with sizes of the order of several tens of micrometers.

6.5.1 Test sample 1

The first test sample was a patterned 100nm thick gold film comprising of triangles (side length 5μm) in a hexagonal array with a 10μm period along a given lattice vector (Figure 6.4).

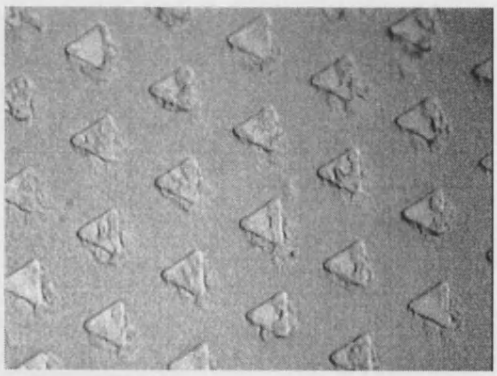

Figure 6.3 Optical micrograph of test sample 1

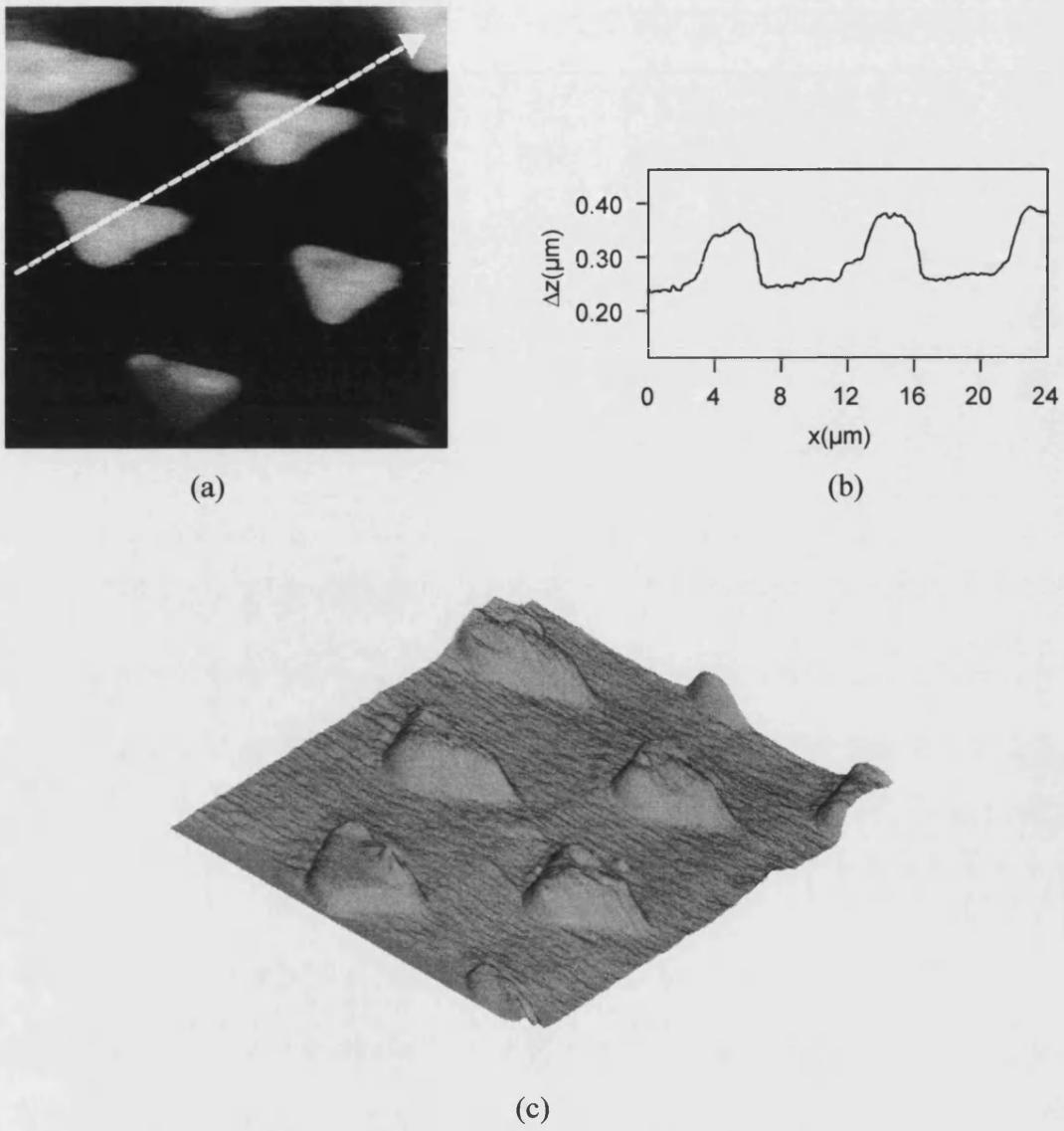

Figure 6.4 (a) AFM scan of the sample (greyscale spans 100nm, 25x25μm), (b) linescan in the direction indicated in (a). (c) 3D render of (a).

The triangular test pattern was scanned at a speed of 2μm/s using cantilever 1 at room temperature. The microscope chamber was evacuated to a pressure of ~$1x10^{-2}$ mbar, resulting in a resonant Q factor of 606 close to the sample surface.

The AFM scan (Figure 6.4(a)) of the sample clearly shows a good representation of the triangles shown in the optical micrograph and even the surface roughness on the triangles is reproduced. From the linescan (Figure 6.4(b)) it can be seen that the

height is also close to that expected ~100nm. The 3D render does however indicate some sloping at the edges of the triangles. This is due to the slow response time of the feedback mechanism. This can be attributed to both the feedback electronics (which are designed for STM i.e. logarithmic feedback) and the high Q of the cantilever resonance. This is not such a problem for sample 1 as the triangles are spaced relatively far apart, but for closer deeper features this does present a problem.

6.5.2 Test sample 2

The second test sample was an array of 2 x 10μm rectangles with a spacing of 2μm in the direction parallel to the shortest length (Figure 6.5). The sample has a 100nm coating of NiFe under 50nm of Au providing some magnetic features that can be measured simultaneously using the Hall sensor. The total height of the rectangles is ~250nm. The structure of the sample is shown in Figure 6.5(b).

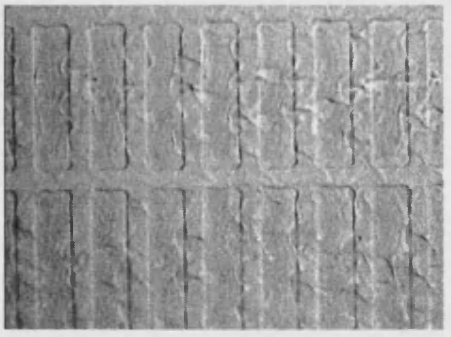

(a)

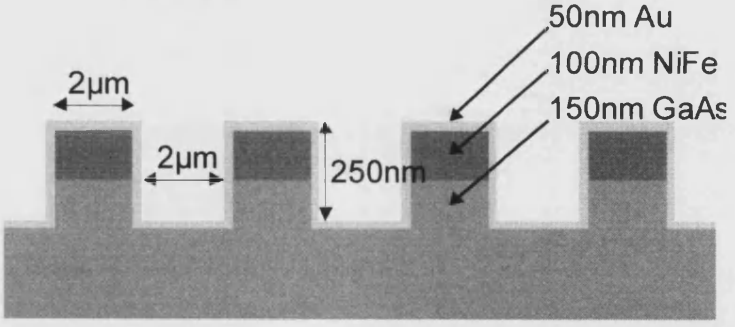

(b)

Figure 6.5 (a) Optical micrograph of test sample 2 (b) cross section schematic of the sample

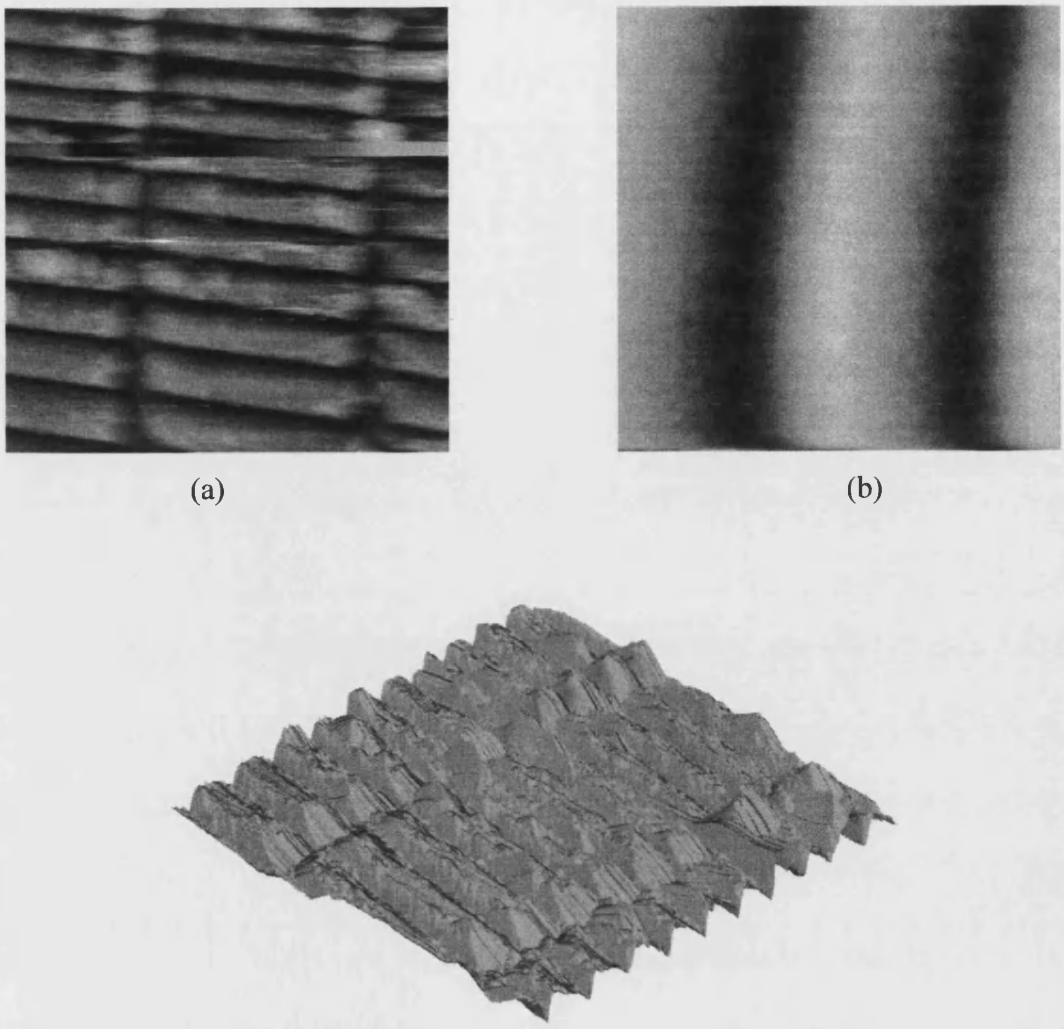

Figure 6.6 (a) Room temperature AFM scan of test sample 2 (greyscale spans 400nm, 25x25μm). (b) Corresponding magnetic scan recorded simultaneously as (a). (c) 3D render of (a)

At room temperature the second test sample pattern was scanned at a speed of 1μm/s using cantilever 16. The microscope chamber was again evacuated to a pressure of ~$1x10^{-2}$ mbar, resulting in a resonant Q factor of 289.

The second test sample proved a far more challenging sample to scan due to the close spacing of the rectangles. At room temperature the array of rectangles is

clearly resolved in the AFM scan (Figure 6.6(a)). Some artefacts are present within the scan where the feedback signal was lost. The 3D rendering shows how the feedback response is too slow at the transition from the top of the rectangle to the surface floor resulting in large ramp-like effects at the rectangle ends. The magnetic image is not so clear. The spatial resolution of the Hall cross on cantilever 16 was ~1.5μm and this, combined with the distance of the Hall cross from the sample surface, meant that the multi-domain magnetic structure of the NiFe bars was unresolved. The image is more representative of a spatially-averaged field rather than that of local features. It is also important to note that the area scanned by the AFM tip is not the same as that scanned by the Hall sensor. The Hall sensor is up to 20μm from the tip in some cantilever designs, resulting in a Hall image and an AFM image of two different areas which are up to 20μm apart.

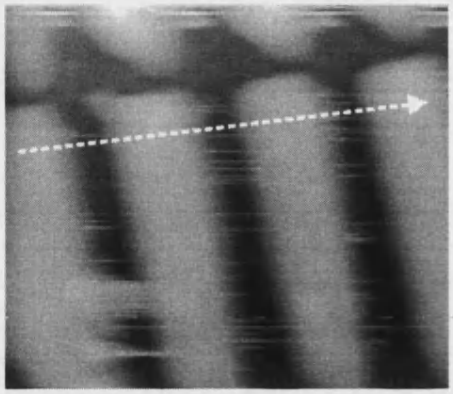

(a)

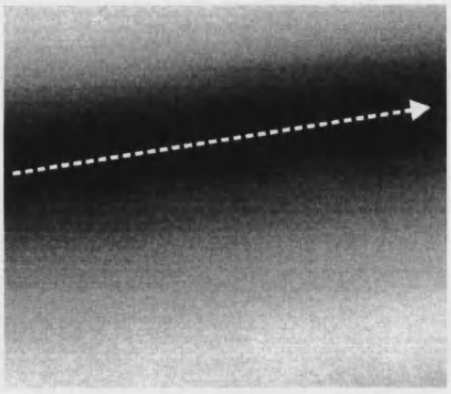

(b)

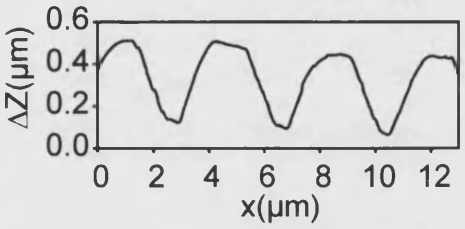

(c)

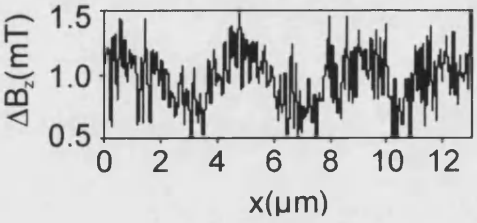

(d)

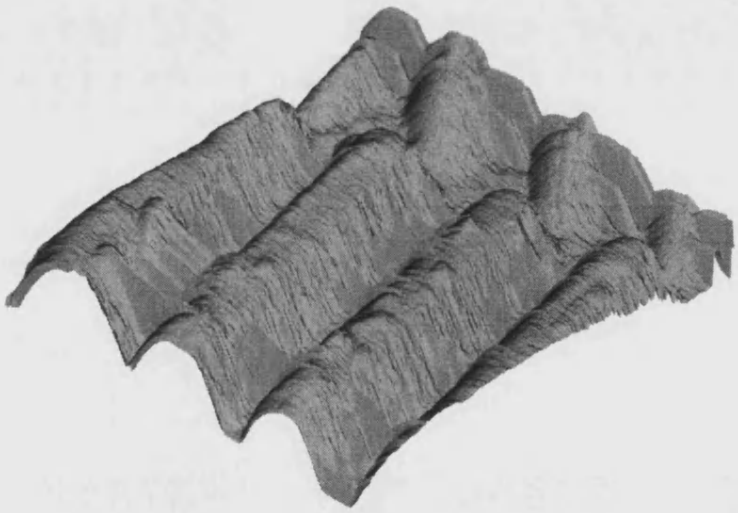

(e)

Figure 6.7 (a) AFM scan of test sample 2 at 77K (greyscale 450nm, 12x10μm). (b) Corresponding magnetic scan recorded simultaneously as (a) (greyscale ~6mT). (c) & (d) are linescans in the directions indicated on (a) and (b) respectively.

At low temperature the second test sample pattern was scanned at a speed of 1μm/s using cantilever 16. The microscope chamber was evacuated to a pressure of ~$1x10^{-2}$ mbar and then cooled to 77K, the final pressure not being known due to the chamber being isolated. The resonant Q factor was found to be ~2000 at the surface.

The low temperature AFM scan (Figure 6.7(a)) is over a smaller scan range than the room temperature scan. This is due to the piezoelectric response of the piezotube being ~3.5 times smaller at 77K than at 300K. The maximum scan size is correspondingly reduced from 50μm to ~14μm at 77K. The scan was also captured in a direction perpendicular to that of the room temperature scan. It was found that scanning the cantilever up and down over the sample rather than side to side allowed far better edge resolution. This is clearly shown in the line scan (Figure 6.7(c)) of the AFM image, where the bottom of the sample between the rectangles is well resolved. The 3D view (Figure 6.7(e)) also illustrates the better edge definition and the fine features on top of the rectangles, the problem of the edge slopes are still evident, however. Although the AFM image is better defined at low temperature, the magnetic image (Figure 6.7(b)) is still rather poorly defined, although some detail is present in the line scan (Figure 6.7(d)). Again this is due to the limited spatial resolution of the Hall sensor.

6.5.3 Feedback (Error) Signal

Whilst the slow response time of the feedback loop does introduce some loss in detail at the transitions between large features, some detail can be recovered by examining the feedback (or error) signal. This error signal, which would be zero for a perfect feedback system, allows a qualitative view of surface details missed in the AFM height scan.

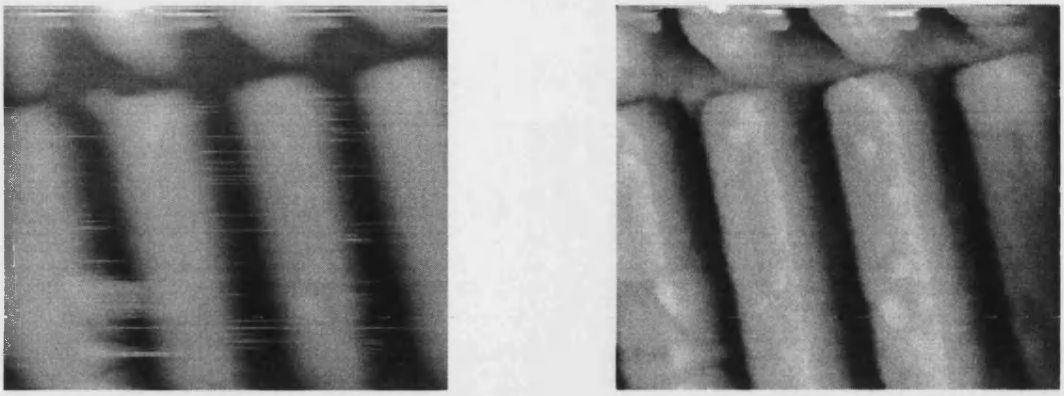

(a) (b)

Figure 6.8 (a) AFM scan of test sample 2. (b) Error signal from scan (a).

This is well illustrated in Figure 6.8. The AFM scan on the left shows the rectangles with some detail visible. The error signal on the right however clearly shows the detail on the surface of the rectangles which is not immediately apparent in the AFM scan. The source of the large error signal is almost certainly due to the feedback system used in the experiments. The feedback electronics are based on a logarithmic amplifier designed for STM measurement, not the linear feedback usually employed in AFM feedback systems.

6.6 MIRS NIST sample

The magnetic imaging reference sample (MIRS) from the national institute of standards and technology (NIST) is a high density data storage disk sample with a complex bit track written on it with a repeat distance of ~10.5μm[4].

6.6.1 Topography

The topography of the sample consists of a striped pattern due to laser texturing performed to smooth the surface prior to writing the magnetic bit tracks.

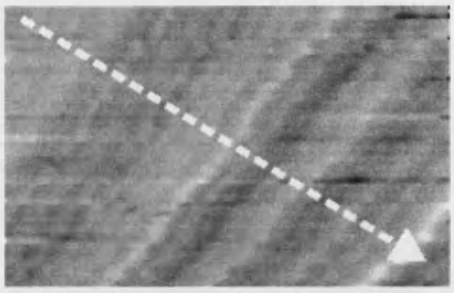

(a)

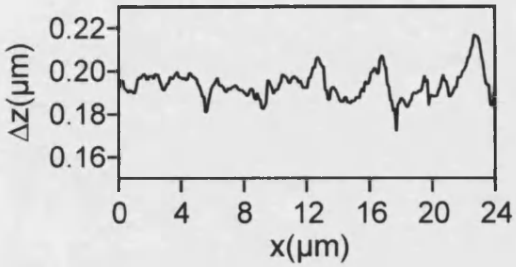

(b)

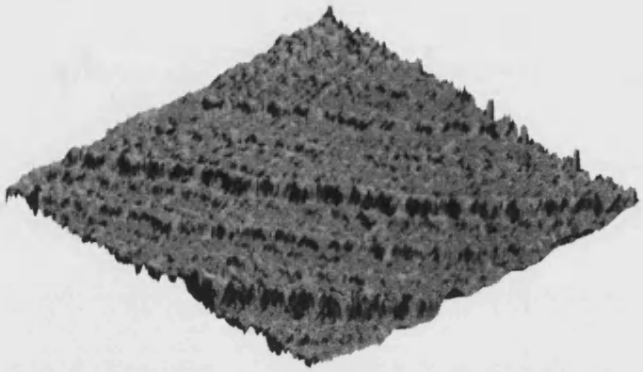

(c)

Figure 6.9 (a) Topographic scan of the NIST sample at 300K (greyscale 80nm, 20x10μm). (b) linescan in the direction indicated in (a). (c) 3D render of AFM scan.

The scan was performed using cantilever 1 at a speed of 1μm/s at room temperature. The striped surface of the NIST sample is resolved by the AFM, the surface height varies by approximately 40nm.

6.6.2 Magnetic scan

Due to problems with the Hall sensor on cantilever 1 the magnetic scan was not captured at the same time as the topographic scan. The magnetic scan shown in Figure 6.10(a) was recorded at room temperature using cantilever 24, a 2DEG cantilever with a 1μm Hall sensor, in contact mode.

(a) (b)

Figure 6.10 (a) Magnetic scan of NIST sample at 300K (greyscale 20mT, 20x20μm), (b) linescan indicated in (a)

The bit track, with the expected periodicity of ~10.5μm, is clearly resolved in the magnetic scan, with two distinct tracks running parallel to each other. The linescan (Figure 6.10(b)) reveals further detail, small peaks and valleys of the order of ~1μm being resolved.

The scan at 77K was recorded using cantilever 19, as cantilever 24 broke after recoding the scan in Figure 6.10.

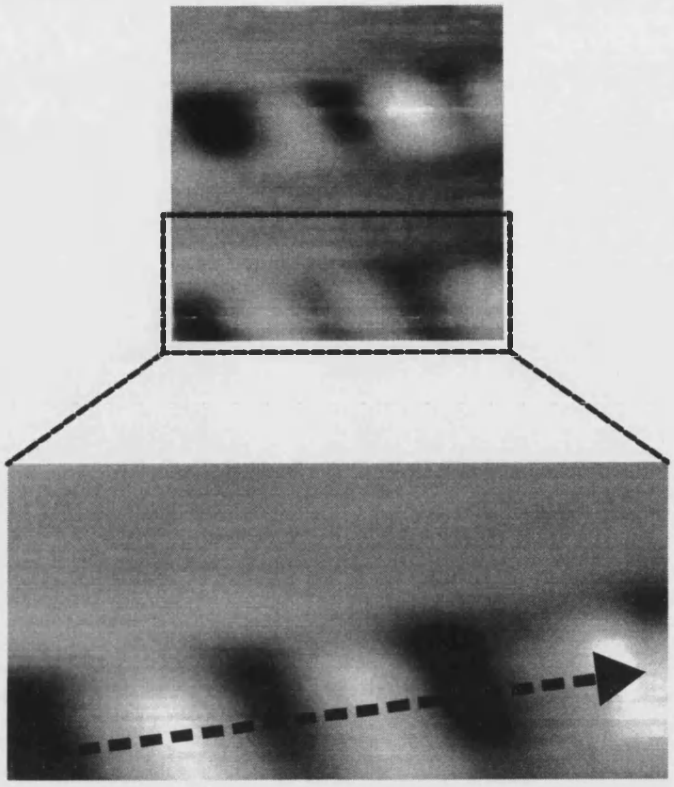

(a)

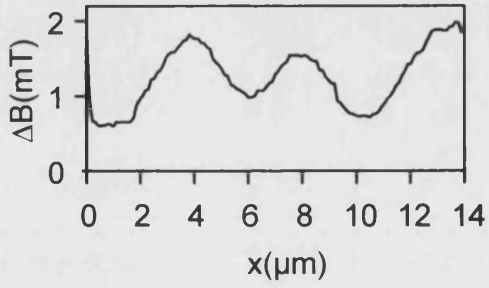

(b)

Figure 6.11 (a) Magnetic scan of NIST sample at 77K (greyscale 2.5mT, 14x14μm, higher resolution image 14x6μm), (b) linescan indicated in high res. image (a)

As can be seen in Figure 6.11(a) the image at 77K does not appear to contain such fine detail. This is not what is usually expected as the SNR is much higher at low temperatures. It can be seen that there is a large reduction in noise, but there is also a large decrease in response, almost an order of magnitude. This is clearly seen by comparing the linescans, Figure 6.10(b) and Figure 6.11(b). The former spans approximately 20mT and the latter only 2mT. The loss of detail could be due to the change in sensor and the Hall sensor resolution.

It is more likely that it is due to the Hall sensor being much closer to the sample surface in the room temperature scan. This change in distance could be attributed to the different sensor, as the distance between the tip and Hall probe is slightly different for each cantilever. It is probably not the full explanation however. A more subtle effect of cantilever bending was noticed when mounting the Cantilevers in the SHPM microscope, which could dramatically affect the sample-sensor spacing.

The cantilevers bend due to strain at the interface between GaAs/AlGaAs and the Ohmic contacts due to their different coefficients of thermal expansion. The effect was found to increase with increased alloying temperature during fabrication. The effect this has on the magnetic scanning is simple, the larger the cantilever bending, the larger the Hall sensor to sample distance. At low temperatures the degree of this effect is largely unknown; it is entirely possible that the bending increases at low temperatures, further increasing the distance between the Hall sensor and the surface.

6.7 YBCO square sample

The 0.35μm thick (001) $YBa_2Cu_3O_{7-\delta}$ (YBCO) film was grown on an MgO substrate at 690°C by electron beam co-evaporation of the metals. It was patterned into an array of 5μm squares in a 10μm period square array using optical lithography and Ar ion milling, and subsequently annealed in oxygen to optimise the stoichiometry. The sample was zero field-cooled to 77K when a 2.5 mT field was applied perpendicular to the film. The sensor was then scanned across the sample at a constant height of ~1μm.

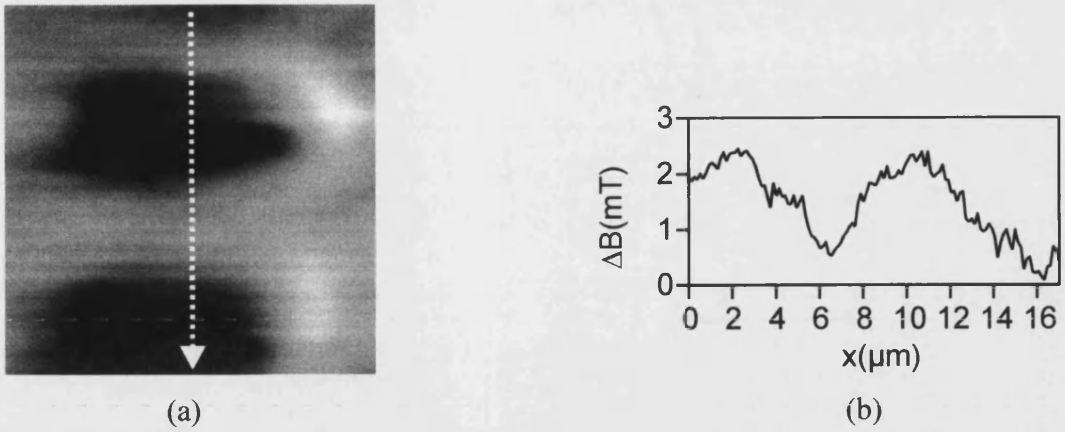

Figure 6.12 (a) Magnetic scan over 2 YBCO squares (greyscale 2.5mT, 16×16μm), T=77K, $\mu_0 H_z$=2.5mT. (b) Linescan in the direction indicated in (a).

Figure 6.12(a) shows a 77K magnetic image of part of the array of 5μm YBCO squares. Dark areas where the superconducting squares have screened the penetration of flux are well resolved and can be seen more clearly in the adjacent linescan (Figure 6.12 (b)).

The topography of the YBCO sample was not measured due to a problem with scanning electronics; this required that the Hall probe be scanned in constant height mode. The cantilever was brought into contact with the surface using the piezoresistor voltage as a guide, and then backed off ~1μm. At this fixed z-extension of the piezotube the sensor was scanned across the sample and the output recorded. The main disadvantage of this mode is that the sensor-sample spacing is inevitably not constant throughout the measurement due to imperfect manual alignment, requiring post processing of the image to remove the slope which appears in the image.

6.8 References

[1] D. Sarid, Scanning force microscopy, OUP, 1991

[2] T. R. Albrecht, P. Grutter, D. Horne, and D. Rugar, *J. App. Phys.*, **69**, (1991)

[3] T. Sulchek *et. al.*, *App. Phys. Lett.*, **76**, (2000)

[4] P. Rice, S.E. Russek, J. Hoinville, M.H. Kelley, *IEEE Trans. Mag.*, **33**, 4065 (1997).

Chapter 7

7 Conclusions and future suggestions

7.1 Conclusions

We have successfully demonstrated the possibility of combining the technologies of SHPM and AFM for the production of a novel integrated sensor that can simultaneously measure sample topography and local surface magnetic induction. Using the AFM-guided SHPM technique it is now possible to image samples that could not be previously imaged using the STM-guided SHPM system. The unique advantages of SHPM can now be extended to the imaging of non-conducting or topologically unconnected magnetic samples.

We have also shown that by using GaAs/$Al_xGa_{1-x}As$ epilayer systems we can achieve sensitivities comparable to those of more popular p-Si cantilevers. Using either a dedicated n^+-$Al_xGa_{1-x}As$ epilayer or a GaAs/$Al_xGa_{1-x}As$ 2DEG to define the piezoresistive sensor, large piezoresistive responses can be achieved enabling the imaging of fine (sub-micron) topographical detail.

We have utilised the technique of piezoresistive detection, which had previously been demonstrated almost exclusively in p-type silicon, and fabricated cantilevers using III-V materials with little loss in sensitivity. We have shown that by using standard as well as more novel GaAs processing techniques it is possible to fabricate

a cantilever with a highly sensitive piezoresistive deflection sensor, 1μm Hall probe and a sharp (<100nm diameter) AFM tip, all integrated onto one cantilever.

We have shown that cantilevers can be fabricated from one of two methods. Either using a dedicated n^+-$Al_xGa_{1-x}As$ piezoresistive layer, allowing the properties of the layer to be altered by the use of MBE techniques. Alternatively one can use a GaAs/$Al_xGa_{1-x}As$ 2DEG system for both the Hall sensor and the piezoresistor, which results in deflection sensitivities near and sometimes in excess of those of the n^+-$Al_xGa_{1-x}As$ piezoresistive cantilevers. The ability to use the 2DEG for both sensors also enables the fabrication time to be reduced by half and reduces the complexity of the fabrication procedure.

7.2 Future suggestions

7.2.1 Design

The design of the cantilever was altered many times during the course of the project. These revisions were usually implemented to either solve a problem with the old design or to increase the performance of the current design. Some of the more subtle problems, such as cantilever bending due to the difference in thermal expansion coefficients of the ohmic contacts and the GaAs cantilever, were not identified until operation in the SHPM system towards the end of the project. Some design flaws therefore still remain in the current sensor generation. With this in mind it is it is possible to recommend a design based upon the knowledge gained from both the fabrication and experimental usage of the cantilevers.

The first recommendation would be to use the 2DEG for both the Hall sensor and piezoresistive sensor. This removes many problems inherent with the separate epilayer design such as parallel conduction and complex fabrication procedures with little, if any, loss in sensitivity. It also greatly reduces the complexity of the cantilever fabrication, which in turn greatly reduces the fabrication time and

improves device yield. There are some drawbacks to using this technique however, as discussed in chapter 4, the major effect is that the sensor becomes far more temperature and light dependent.

Other recommendations are presented schematically in Figure 7.1. In order to increase the sensitivity of the cantilever a technique that is used in many AFM designs is to remove a centre channel (or channels) to increase the stress in the piezoresistor for a given deflection. The design in Figure 7.1, whilst introducing three stress enhancing channels, also doubles the length of the piezoresistor, further increasing sensitivity as in Tortenese's[1] original piezoresistive cantilever design.

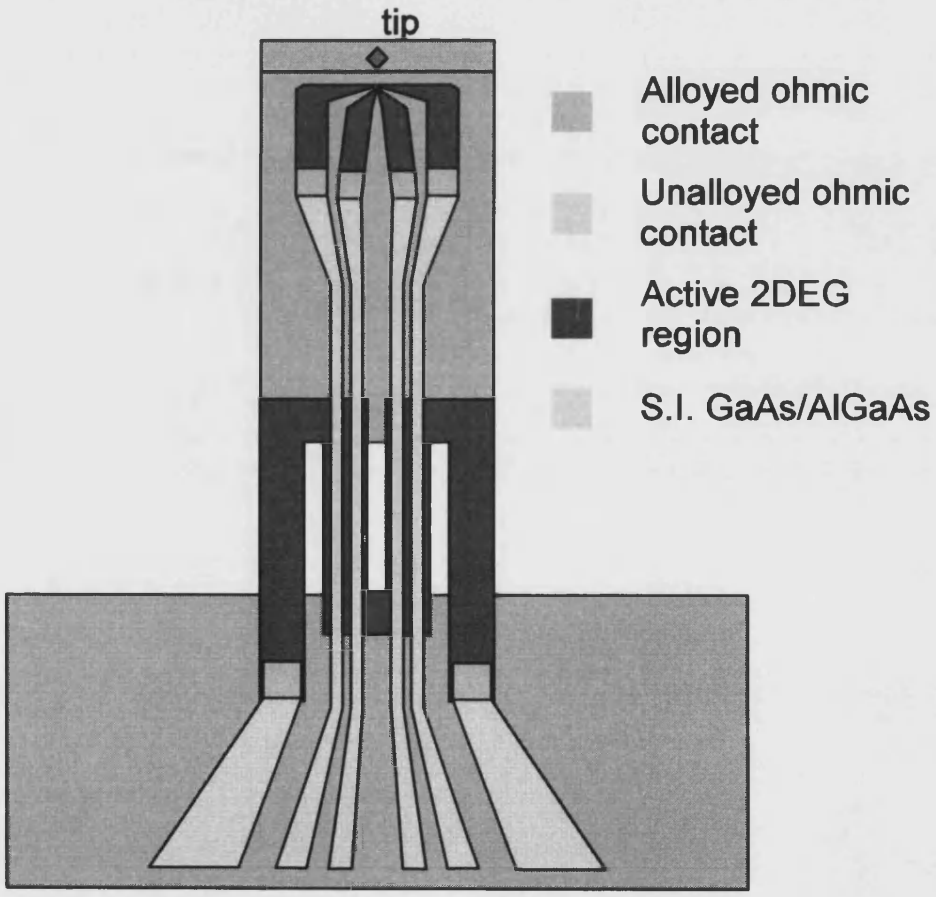

Figure 7.1 Future cantilever design

One benefit of this design is that the mounting of the cantilever in the SHPM system is far simpler as there is no need to modify the commercial chip carrier before the sensor can be mounted. In the new configuration, the four Hall probe connections are between the two piezoresistor connections, and mounting can be achieved in the same way as a regular STM-SHPM sensor. The problem of cantilever bending is also addressed by only using small alloyed ohmic pads which are electrically contacted using un-alloyed Au/Ti leads deposited on top of the pads.

7.2.2 Scanning electronics

As the primary goal of this project was to design and fabricate the sensor, little time was left for the optimisation of the control electronics used to operate the sensor in the SHPM system. The scanning method used to obtain the results in Chapter 6 was capable of producing reasonably detailed AFM scans when scanned at a slow rate but was definitely not the optimum method for producing high precision AFM data. Modern AFM imaging techniques use dedicated hardware incorporating FM detection[2] methods and active Q control[3], allowing high speed, high detail images to be produced. If the AFM-SHPM technique is to be further used it would benefit greatly from dedicated control electronics, which would permit high speed imaging to be performed. This would represent a significant advance for SHPM, allowing high speed topographic imaging with feedback, and real-time SHPM has already been demonstrated whilst scanning in fixed height mode[4].

7.2.3 2DEG piezoresistive characterisation

If the 2DEG is to be used as the piezoresistive sensor, the stress related properties of the material should be further investigated. The process by which piezoresistance arises in the 2DEG is not fully understood and little information is to be found in the literature, the work by Dana *et. al.*[5] being the only known implementation of piezoresistance using a $GaAs/Al_xGa_{1-x}As$ 2DEG.

The piezoresistive response of the 2DEG could be evaluated using a method similar to that outlined in section 2.3.5. A better understanding of the piezoresistive process within the 2DEG would allow further optimisation of the material with regard to piezoresistive response.

7.2.4 Piezoelectric actuation

It has been shown that by integrating a ZnO piezoelectric actuator onto a p-Si AFM cantilever high speed imaging can be achieved[6]. Imaging bandwidth was increased by up to 4 orders of magnitude by using the integrated actuator rather than the scanning piezotube. This allowed scanning speeds of 3mm/s, compared to the 2μm/s frequently used in our experiments. Unwanted coupling between the actuator and the piezoresistor was removed by the use of a lock-in amplifier.

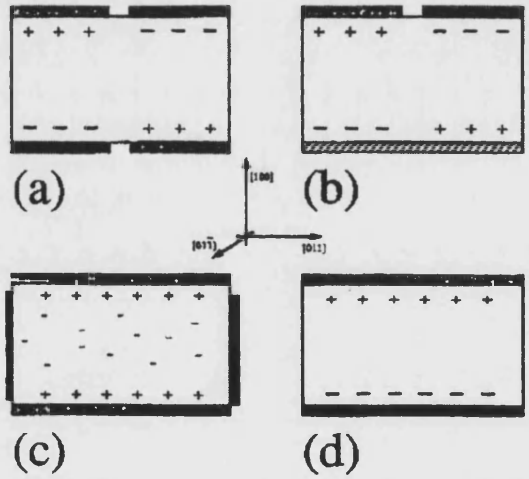

Figure 7.2 Electrode configuration for a $[01\bar{1}]$ beam vibrating in (a)-(b) flexurally in the $[011]$ direction, (c) flexurally in the $[100]$ direction, and (d) longitudinally in the $[01\bar{1}]$ direction[7]

For Si cantilevers a ZnO layer is required as Si does not exhibit a piezoelectric response, GaAs/AlGaAs however does. This raises the possibility of using the GaAs

chip to fabricate both the sensor and the actuator, which would allow much faster imaging to be achieved. Different modes of bending can be induced by applying voltages in different configurations as shown in Figure 7.2. From this a suggested design is shown in Figure 7.3. This design would allow the application of a voltage across the electrodes to bend the cantilever up and down, by inducing flexural bending in the [100] direction.

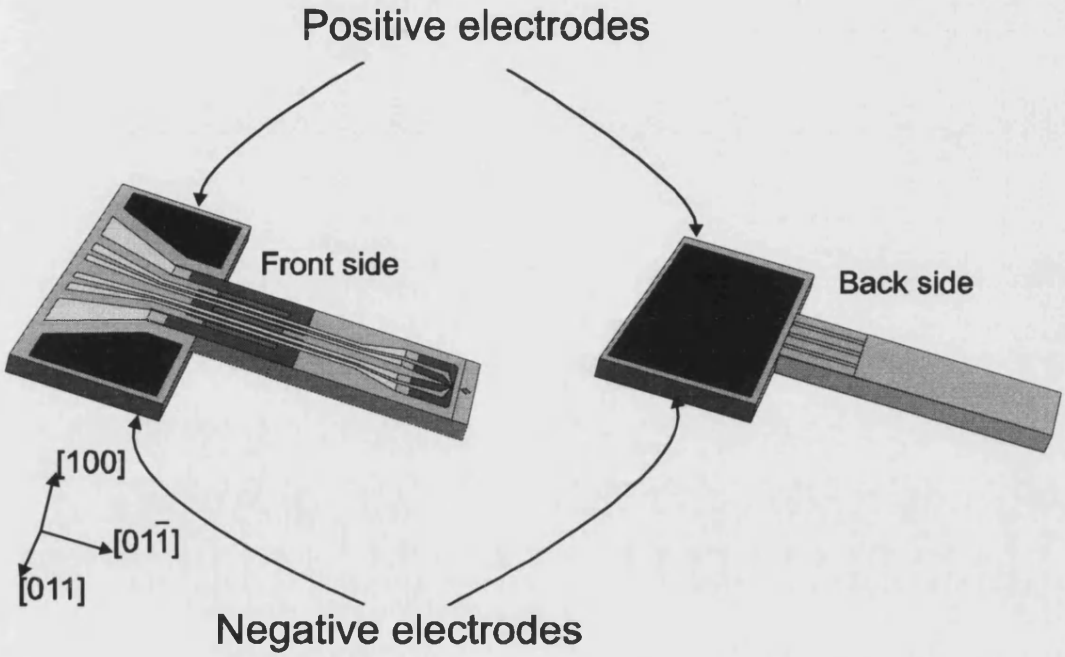

Figure 7.3 Suggested cantilever design with piezoelectric electrodes placed for flexural displacement in the [100] direction

Care must obviously be taken to isolate the piezoelectric voltage and prevent interference with the other sensors.

7.2.5 Other 2DEG devices

The integration of a 2DEG system at the surface of the piezoresistive cantilever also means that other secondary III-V sensors could be fabricated onto the cantilever which could further exploit the properties of direct gap semiconductors, e.g. a vertical cavity surface emitting laser or a single electron transistor, extending the

capabilities of the cantilever. This project, by showing that it is possible to integrate two sensors, should allow the integration of further sensors. The extensions to this work are many and varied, with further work the AFM cantilever could become a "lab on a chip", whereby several sensors on the same cantilever all work simultaneously to analyse a sample surface, giving rise to many different applications of the technique.

7.3 References

[1] M. Tortonese, H Yamada, R. C. Barrett and C. F. Quate, *in Proceedings of transducers '91* (IEEE) 448, (1991)

[2] T. R. Albrecht, P. Grutter, D. Horne, and D. Rugar, *J. App. Phys.*, **69**, 668 (1991)

[3] T. Sulchek *et. al.*, *App. Phys. Lett.*, **76**, 1473 (2000)

[4] A. Oral, S. J. Bending, M. Henini, *App. Phys. Lett.*, 69, 1324 (1996)

[5] A. Dana, F. Ho, Y. Yamamoto, *App. Phys. Lett.*, **72**, 1152 (1998)

[6] Manalis S. R., Minne S. C., and Quate C. F., *App. Phys. Lett*, **68**, 871 (1996)

[7] K. Hjort, J. Soderkvist and J. Schweitz, *J. Micromech. Microeng.* , **4**, 1 (1994)

Appendix A

A Transformation of Coordinates

Vector transformations are useful for converting from one coordinate system to another, or for converting an arbitrary vector to a vector in a given coordinate system. The method of Euler angles is most commonly used for this purpose. By the Euler transformation, three new axes (x', y', z') are defined from the original (x, y, z) axes, by three successive axis rotations. First, the x-y plane is rotated about the z axis by an angle θ to create the x''' and y'' axis Fig. A-1(a).

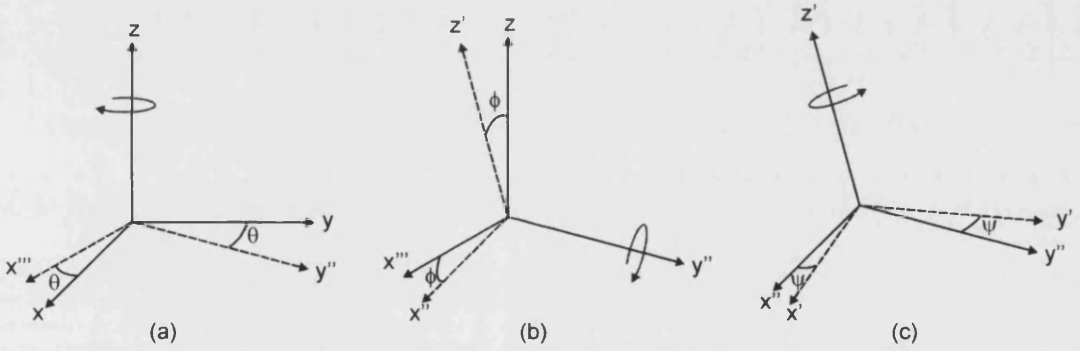

Figure A-1Definition of Euler angles. (a) rotation about z axis. (b) rotation about y'' axis. (c) rotation about z' axis.

This transformation can be expressed as

$$\hat{x}''' = cos\,\theta\hat{x} + sin\,\theta\hat{y}$$
$$\hat{y}'' = -sin\,\theta\hat{x} + cos\,\theta\hat{y} \qquad (A.1)$$

The second transform Fig A-1(b) is a rotation about the y'' axis of angle ϕ, transforming x''' onto x'' and z into z'. Expressed as

$$\begin{aligned}
\hat{x}'' &= \cos\phi\hat{x}''' - \sin\phi\hat{z} \\
\hat{z}' &= \sin\phi\hat{x}''' + \cos\phi\hat{z} \\
&= \sin\phi(\cos\theta\hat{x} + \sin\theta\hat{y}) + \cos\phi\hat{z} \\
&= \cos\theta\sin\phi\hat{x} + \sin\theta\sin\phi\hat{y} + \cos\phi\hat{z}
\end{aligned} \tag{A.2}$$

Finally x'' and y'' are transformed onto x' and y' via a rotation ψ about z'.

$$\begin{aligned}
\hat{x}' &= \cos\psi\hat{x}'' + \sin\psi\hat{y}'' \\
&= \cos\psi(\cos\theta\cos\phi\hat{x} + \sin\theta\cos\phi\hat{y} - \sin\phi\hat{z}) + \sin\psi(-\sin\theta\hat{x} + \cos\theta\hat{y}) \\
&= (\cos\theta\cos\phi\cos\psi - \sin\theta\sin\psi)\hat{x} + (\sin\theta\cos\phi\cos\psi\hat{y} + \cos\theta\sin\psi)\hat{y} \\
&\quad -(\sin\phi\cos\psi)\hat{z} \\
\hat{y}' &= -\sin\psi\hat{x}'' + \cos\psi\hat{y}'' \\
&= -\sin\psi(\cos\theta\cos\phi\hat{x} + \sin\theta\cos\phi\hat{y} - \sin\phi\hat{z}) + \cos\psi(-\sin\theta\hat{x} + \cos\theta\hat{y}) \\
&= (-\cos\theta\cos\phi\sin\psi - \sin\theta\cos\psi)\hat{x} \\
&\quad +(-\sin\theta\cos\phi\sin\psi\hat{y} + \cos\theta\cos\psi)\hat{y} \\
&\quad +(\sin\phi\sin\psi)\hat{z}
\end{aligned} \tag{A.3}$$

We can now define an arbitrary vector r'

$$r' = \begin{bmatrix} x' \\ y' \\ z' \end{bmatrix}$$

$$= \begin{bmatrix} \cos\theta\cos\phi\cos\psi - \sin\theta\sin\psi & \sin\theta\cos\phi\cos\psi\hat{y} + \cos\theta\sin\psi & -\sin\phi\cos\psi \\ -\cos\theta\cos\phi\sin\psi - \sin\theta\cos\psi & -\sin\theta\cos\phi\sin\psi\hat{y} + \cos\theta\cos\psi & \sin\phi\sin\psi \\ \cos\theta\cos\phi & \sin\theta\sin\phi & \cos\phi \end{bmatrix} \begin{bmatrix} \hat{x} \\ \hat{y} \\ \hat{z} \end{bmatrix}$$

$$r' = \begin{bmatrix} l_1 & m_1 & n_1 \\ l_2 & m_2 & n_2 \\ l_3 & m_3 & n_3 \end{bmatrix} \begin{bmatrix} \hat{x} \\ \hat{y} \\ \hat{z} \end{bmatrix} \tag{A.4}$$

where l_i, m_i and n_i are known as the direction cosines.

Appendix B

B Determination of a cantilever spring constant

B.1 Simple Bending Theory

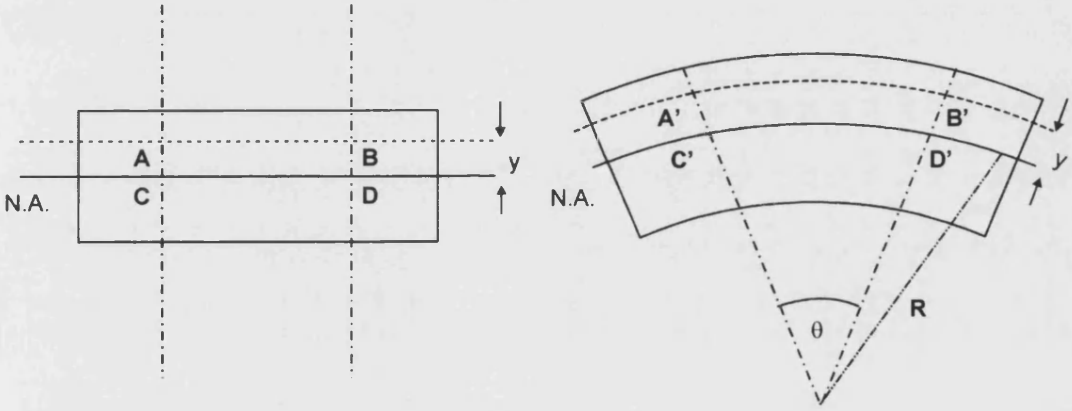

Figure B.1 Unstressed and stressed beam

Consider a simple beam undergoing a bending moment as in Figure B.1. The strained beam is in tension at the top surface and under compression at the lower surface. It is therefore reasonable to assume at point halfway between these two surfaces there are points where the stress is zero. This is known as the neutral axis (N.A.). The strain in fibre A'B' is

$$strain(A'B') = \frac{A'B' - AB}{AB} \qquad \text{(B.1)}$$

unstrained *AB* is the same length as *CD.* As CD is on the neutral axis it is the same length as *C'D'* leading to

$$strain(A'B') = \frac{A'B'-C'D'}{C'D'} = \frac{(R+y)\theta - R\theta}{R\theta} = \frac{y}{R} \tag{B.2}$$

Young's modulus is defined as, E = *stress/strain,* so the stress on a fibre at a distance y from the neutral axis is given by

$$\sigma = \frac{E}{R}y \tag{B.3}$$

Considering the beam cross section

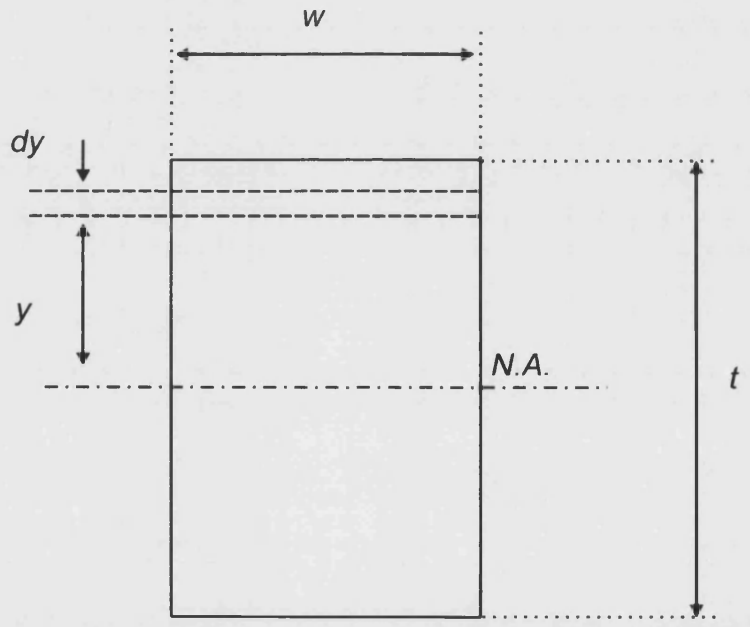

Figure B.2 Cross section of beam

If the strip in Figure B.2 is of area δA the force on the strip is

$$F = \sigma\delta A = \frac{E}{R}y\delta A \tag{B.4}$$

This has a moment about the neutral axis of

$$Fy = \frac{E}{R} y^2 \delta A \tag{B.5}$$

The total moment, M, for the whole cross section is

$$M = \frac{E}{R} \sum y^2 \delta A \tag{B.6}$$

where $\sum y^2 \delta A$ is the second moment of area I, giving,

$$M = \frac{EI}{R} \tag{B.7}$$

B.2 Moment of inertia

Considering the beam cross section in Figure B.2 the moment of inertia can be written as

$$\begin{aligned} I &= \int_{-½}^{½} y^2 w dy = w \int_{-½}^{½} y^2 dy \\ &= \frac{wt^3}{12} \end{aligned} \tag{B.8}$$

B.3 Beam Slope and deflection

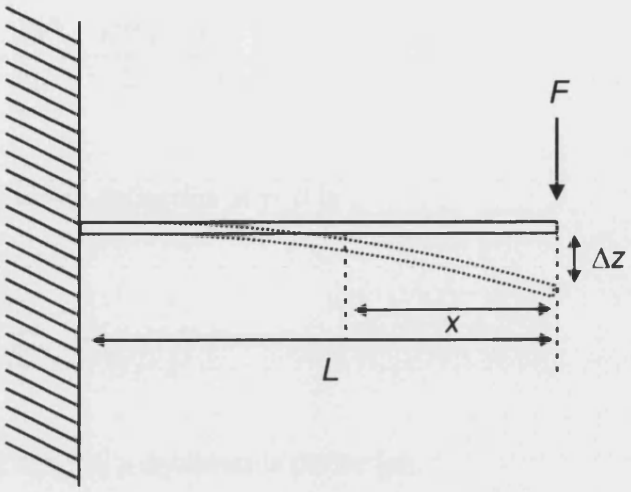

Figure B.3 Cantilever with concentrated load at the end

The basic differential equation for the deflection of beams is given by

$$M = EI\frac{d^2z}{dx^2} \tag{B.9}$$

Using this, it is possible to calculate the slope and deflection at any point x along the beam.

$$\begin{aligned} M &= EI\frac{d^2z}{dx^2} = -Fx \\ \frac{dz}{dx} &= \frac{1}{EI}\left(-\frac{Fx^2}{2} + A\right) \\ z &= \frac{1}{EI}\left(-\frac{Fx^3}{6} + Ax + B\right) \end{aligned} \tag{B.10}$$

Now when

$$\begin{aligned} x = L,\quad \frac{dz}{dx} = 0 \qquad &\therefore\quad A = \frac{FL^2}{2} \\ x = L,\quad z = 0 \qquad &\therefore\quad B = \frac{FL^3}{6} - \frac{FL^2}{2}L = -\frac{FL^3}{3} \end{aligned} \tag{B.11}$$

giving

$$z = \frac{1}{EI}\left(-\frac{Fx^3}{6} + \frac{FL^2x}{2} - \frac{FL^3}{3}\right) \tag{B.12}$$

Therefore the maximum deflection at $x=0$ is

$$z_{max} = -\frac{FL^3}{3EI} \tag{B.13}$$

The negative sign denotes a downwards deflection.

B.4 Spring Constant

For a rectangular beam with a constant cross section as in Figure B.2 the spring constant, k, can be written by combining equations B.8 and B.13 and by using Hooke's law, $F=k\Delta z$ to give

$$k = \frac{Ewt^3}{4L^3} \tag{B.14}$$

Appendix C

C Publications

C.1 Conference presentations

"Integrated AFM cantilever with 2DEG Hall Probe for magnetic imaging"
A J BROOK
Las Vegas 2002 Scanning Probe Microscopy, Sensors and Nanostructures conference

C.2 Journal Publications

"Micromachined III-V cantilevers for AFM-tracking scanning hall probe microscopy"
Brook AJ, Bending SJ, Pinto J, Oral A, Ritchie D, Beere H, Springthorpe A, Henini M, *JOURNAL OF MICROMECHANICS AND MICROENGINEERING*, 13 (1): 124-128 JAN 2003

"Integrated piezoresistive sensors for atomic force-guided scanning Hall probe microscopy"
Brook AJ, Bending SJ, Pinto J, Oral A, Ritchie D, Beere H, Henini M, Springthorpe A, *APPLIED PHYSICS LETTERS*, 82 (20): 3538-3540 MAY 19 2003